

THESIS FOR THE DEGREE OF DOCTOR OF PHILOSOPHY

**Electrical Charges on Polymeric Insulator Surfaces and their  
Impact on Flashover Performance**

SARATH KUMARA



Department of Materials and Manufacturing Technology  
CHALMERS UNIVERSITY OF TECHNOLOGY  
Gothenburg, Sweden 2012

Electrical Charges on Polymeric Insulator Surfaces and their Impact on Flashover Performance

SARATH KUMARA  
ISBN 978-91-7385-764-2

© SARATH KUMARA, 2012.

Doktorsavhandlingar vid Chalmers tekniska högskola  
Ny seire nr. 3445  
ISSN 0346-718X

High Voltage Engineering  
Department of Materials and Manufacturing Technology  
Chalmers University of Technology  
SE-412 96 Gothenburg  
Sweden  
Telephone: +46 (0)31-772 1000

Chalmers Bibliotek, Reproservice  
Göteborg, Sweden 2012

*To Hansi, Hesanya and my parents*



# Electrical Charges on Polymeric Insulator Surfaces and their Impact on Flashover Performance

**Sarath Kumara**

Division of High Voltage Engineering,  
Department of Materials and Manufacturing Technology,  
Chalmers University of Technology.

## Abstract

Utilization of remotely located sustainable energy resources such as solar, wind and hydro calls for further developments of long-distance electric power transmissions operating at ultra-high voltage (UHV) levels which may exceed 1000 kV ac and 800 kV dc utilized today. It is foreseen that insulation of such transmission systems is to be based on polymeric materials that can provide a number of technical benefits over traditionally used glass and porcelain based insulation. As several studies have provided evidences of possible deterioration of withstand properties of polymeric insulators when electric charges are accumulated on their surfaces, especially under dc and impulse stresses, there is a need for acquiring knowledge on the mechanism lying behind such influences for improving design of polymeric insulators as well as related testing methodology.

The research presented in the thesis focuses on three main subjects, i.e. surface charging of polymeric insulation materials by external corona discharges, surface charge decay on thick material layers and impact of surface charges on dc and impulse flashover performance of model insulators.

Charging of polymeric surfaces was analyzed by utilizing a computer model describing development of corona discharges in air. Validity of the model was verified by comparing the calculated and measured corona currents in a needle-plane electrode system with a dielectric barrier. The simulations showed, depending on time regimes of the applied voltage, formation of either positive glow or burst current pulses that led to different conditions of charge deposition on the polymeric surface. The distributions of deposited charges were further investigated by measuring potential distributions along surfaces of flat and cylindrical samples of silicone rubbers, typically used for insulator manufacturing. The obtained results demonstrated existence of significant differences in the surface charge patterns for different charging conditions.

Dynamic behaviour of the deposited surface charges was studied on fresh and aged samples of the silicone rubbers. The developed experimental procedure allowed for distinguishing between the effects of surface charge neutralization through the bulk of polymeric material or by so-called gas neutralization, the latter being conditioned by presence of free ions in the surrounding air. It was found that increased amount of free ions in the air as well as aging of the material accelerated strongly the charge decay

process. For the aged materials the decay became sensitive to air wetness. At the same time, the characteristics measured under bulk neutralization regime were utilized for estimating the conductivities of the studied materials.

The impact of surface charging on flashover performance of polymeric insulator models was analysed experimentally and theoretically. In the experimental study, a cylindrical composite insulator model was used, which consist of a fiberglass-epoxy rod covered with a layer of silicone rubber. The surface of the insulator was charged to various magnitudes and negative dc flashover voltage levels were determined. The obtained results demonstrated that deposition of a negative surface charge enhanced the dc withstand level, whereas deposition of positive charge reduced it. The dc flashover voltages of the charged insulator model were also calculated by means of a model utilizing streamer breakdown criteria. The measured and the calculated dc flashover voltages remained in good agreement for the utilized charging conditions. This further allowed using the model for simulating the influence of surface charging on impulse flashover performance of insulators. A parametric study was performed to investigate the effects of charge magnitude, its polarity and location on the insulator surface. The simulations shown that the dependence of impulse flashover voltage on charge polarity and concentration was similar to that of dc flashover voltage for the cases when the insulator was located far away from the ground (symmetry with regard to voltage polarity). However, when the insulator was standing on a grounded plane, the effect of surface charging was dependent on the polarity of the applied impulse voltage. In the case of positive impulse, presence of positive charge increased the flashover voltage, whereas negative charge yielded their reduction and vice versa.

**Key words:** Surface charge, surface potential, corona charging, charge decay, flashover voltage, streamer criterion, gas neutralization, bulk neutralization, surface conduction, polymeric insulation, bulk conductivity, silicone rubber, humidity.

# Acknowledgements

First, I would like to pay my sincere gratitude to my supervisor Associate Prof. Yuriy Serdyuk for his valuable guidance, support, discussions and revising all my manuscripts. I am grateful to my examiner and co-supervisor Prof. Stanislaw Gubanski for providing guidance, support, new ideas and motivation throughout the project. I would also like to thank the members, present and former, of the reference group, Prof. Uno Gäfvert, Dr. Lars Palmqvist, Dr. Urban Åström, Dr. Henrik Hillborg and Dr. Dan Windmar for valuable discussions and ideas.

My grateful acknowledgment goes to ABB and Swedish Energy Agency for financing my PhD project via ELEKTRA program. Financial support from the “Schneider Electric's fund in memorial of Erik Feuk” for participation in courses and conferences is acknowledged. The National Graduate School in Scientific Computing (NGSSC) is acknowledged for providing financial support to participate in their courses.

Special thanks go to Dr. Henrik Hillborg from ABB Corporate research for providing material samples for potential decay measurements. Also I would like to thank former Master thesis students, Shahid Alam and Imtiaz Hoque, who worked with me and conducted experimental investigations on surface charging and flashover performance of cylindrical model insulators. Former PhD student Dr. Bin Ma is acknowledged for conducting corona treatment of the material samples for potential decay measurements.

I sincerely thank the Department of Materials and Manufacturing Technology, and especially all the former and present colleagues within the High Voltage Engineering and Electric Power Engineering groups for helping me with diverse matters and for creating an enjoyable working atmosphere. I would also like to thank the present and former colleagues from the High Voltage Valley, Samarkand 2015 AB, for creating a friendly working environment for my activities in Ludvika during 2007-2008.

I am grateful to my parents, Siripala and Sumanawathe, for always supporting and guiding me. At last, but not least, my heartfelt thanks go to my wife Anushi for her love, understanding and encouragement and to my daughter Hesanya for making our home a wonderful place.

Sarath Kumara  
Göteborg, Sweden  
December 2012



# Table of contents

<b>Abstract</b>	<b>v</b>
<b>Acknowledgements</b>	<b>vii</b>
<b>Table of contents</b>	<b>ix</b>
<b>1 Introduction</b>	<b>1</b>
1.1 Background and objectives.....	1
1.2 Outline of the thesis.....	3
1.3 List of publications.....	4
<b>2 Literature review</b>	<b>7</b>
2.1 Charging of polymeric surfaces.....	7
2.1.1 Corona charging.....	8
2.1.2 Pre-stressing.....	9
2.1.3 Modeling of corona discharge in air.....	9
2.2 Surface charge decay.....	10
2.2.1 Decay mechanisms.....	10
2.2.2 Surface charge measurements.....	12
2.2.3 Previous experimental work on charge decay.....	15
2.2.4 Surface potential/charge decay modeling.....	16
2.3 Effect of surface charges on insulator flashover performance.....	21
2.3.1 Experimental observations on surface charge effect.....	21
2.3.2 Calculations of flashover voltages in presence of surface charges.....	23
<b>3 Corona charging of polymeric materials</b>	<b>27</b>
3.1 Physical background.....	27
3.1.1 Charge generation mechanisms.....	28
3.1.2 Charge loss mechanisms.....	28
3.1.3 Charge transport mechanisms.....	29
3.2 Mathematical model.....	30
3.2.1 Model equations.....	30
3.2.2 Implementation.....	31
3.3 Validation of the model.....	33
3.3.1 Experimental setup.....	33
3.3.2 Current at low voltage impulses.....	34

3.3.3	Current at high voltage impulses.....	34
3.4	Corona modes in air.....	36
3.4.1	Glow corona.....	36
3.4.2	Burst corona.....	39
3.5	Surface charging by impulse corona.....	42
3.5.1	Charging by glow corona.....	42
3.5.2	Charging by burst corona.....	45
<b>4</b>	<b>Surface charging and charge decay on HTV silicone rubber</b>	<b>49</b>
4.1	Experiments.....	49
4.1.1	Experimental setup .....	49
4.1.2	Experimental procedure .....	50
4.1.3	Material types.....	51
4.1.4	Test conditions.....	52
4.2	Decay due to bulk neutralization.....	52
4.2.1	Potential distribution on the surface .....	53
4.2.2	Potential decay at the sample centre.....	55
4.2.3	Decay rates and field dependent apparent bulk conductivities.....	55
4.2.4	Trap density distributions.....	58
4.2.5	Effect of charging conditions on decay.....	59
4.3	Contribution of gas neutralization to charge decay.....	61
4.3.1	Decay due to bulk and natural gas neutralization.....	61
4.3.2	Decay due to bulk and enhanced gas neutralization .....	63
4.3.3	Comparison of three gas neutralization modes.....	64
4.4	Contribution of surface conduction to charge decay.....	67
4.4.1	Corona treatment.....	67
4.4.2	Potential distributions .....	68
4.4.3	Surface potential decay .....	71
4.4.4	Influence of relative humidity.....	72
4.4.5	Trap density distributions.....	72
4.5	Comparison of different decay mechanisms.....	74
<b>5</b>	<b>Surface charging of cylindrical polymeric insulator</b>	<b>75</b>
5.1	Experiments.....	75
5.1.1	Setup for surface charging.....	75
5.1.2	Setup for surface potential measurements.....	76
5.1.3	Experimental procedure.....	77

5.2	Calculation of charge densities.....	78
5.2.1	The $\Phi$ -matrix method.....	78
5.2.2	Obtaining the $\Phi$ -matrix .....	79
5.3	Charging with corona belt.....	81
5.3.1	Effect of charging voltage.....	81
5.3.2	Effect of charging time .....	85
5.3.3	Effect of position of the belt.....	85
5.4	Charging by dc pre-stressing.....	87
<b>6</b>	<b>Impact of surface charging on dc flashover performance of insulators</b>	<b>89</b>
6.1	Measurement of flashover voltages.....	89
6.1.1	Test procedure .....	89
6.1.2	Results of the measurements.....	90
6.2	Computational model.....	91
6.2.1	Calculation of electric fields.....	92
6.2.2	Determination of the effective ionization coefficient.....	92
6.3	Calculation of flashover voltage.....	93
6.3.1	Application of the model.....	93
6.3.2	Results and discussion.....	95
<b>7</b>	<b>Prediction of impulse flashover performance of insulators in presence of surface charges</b>	<b>99</b>
7.1	Model validation.....	99
7.1.1	Application of the model .....	99
7.1.2	Comparison of the results.....	101
7.2	Model detail.....	103
7.2.1	Field calculations .....	103
7.2.2	Study cases.....	105
7.2.3	Surface charges and parametric study.....	106
7.3	Results.....	106
7.3.1	Effect of charge magnitude.....	106
7.3.2	Effect of charge location.....	111
7.3.3	Effect of the material.....	114

<b>8</b>	<b>Conclusions</b>	<b>119</b>
8.1	Charging of polymeric surfaces.....	119
8.2	Surface charge decay.....	120
8.3	Effect of surface charge on flashover performance of insulation.....	121
<b>9</b>	<b>Future work</b>	<b>123</b>
	<b>References</b>	<b>125</b>

# 1 Introduction

Utilization of remotely located sustainable energy resources such as solar, wind and hydro calls for further developments of long-distance electric power transmissions operating at ultra high voltage (UHV) levels, e.g., 1000 kV ac and 800 kV dc or even higher [1]. It is also foreseen that insulation of such transmission systems is to be mainly based on polymeric materials [2] that can provide a number of technical benefits over the traditionally used glass and porcelain based insulation. Although withstand performance of polymeric insulating materials has been studied over the years, there is still lack of complete physical understanding of all important aspects related to practical situations. Experimental and theoretical studies provided evidences of a possible deterioration of flashover performance of polymeric insulators when electric charges are accumulated on their surfaces [3-7]. Another consequence of surface charging is a poor repeatability of results for a series of impulse applications during type tests of polymeric insulation systems [8]. Therefore for avoiding unexpected flashover events in such applications, there is a need to understand the surface charge accumulation, its dynamic behavior as well as the influence on insulation performance under various stresses.

## 1.1 Background and objectives

With the above motivation in mind, the objectives of the project have been (1) to analyze processes in gas medium under strong electric fields leading to surface charging of flat polymeric insulation samples and cylindrical model insulators, (2) to study mechanisms responsible for surface charge decay on thick polymeric insulating samples, and (3) to examine the effect of surface charges on impulse and dc flashover performance of insulator models.

Investigations related to surface charging involved both computer modeling and experimental study. The former started with a development of a mathematical model describing corona discharges in air and its computer implementation. Further, the developed model was validated by comparing simulated positive impulse corona currents with measured ones in a needle-plane electrode arrangement. Later on, the

verified model was utilized to identify corona modes, which may be initiated depending on the magnitude and the rate of rise of the applied voltage impulses. Finally, the model was employed to investigate the corona charging process of a polymeric material surface. Dynamics and distributions of space charges and associated electric fields as well as corona currents during material charging by two corona modes (glow and burst) were analyzed and compared. The experimental studies were focused on investigating surface charge profiles on a flat silicone rubber samples and cylindrical polymeric insulator consisted of a glass fiber reinforced epoxy core covered with a layer of silicone rubber. The charging was realized in two different ways reflecting conditions that may appear in service: (i) by utilizing an external corona source, and (ii) by pre-stressing the insulator with a dc voltage. In the case of cylindrical insulator a set of experiments was carried out with the external corona source to investigate effects of its intensity, duration of application and its location with regard to the insulator surface. For all the studied conditions, surface potential distributions were measured after completing the charging process. Further,  $\Phi$ -matrix method was utilized to obtain surface charge density profiles from the measured potential distributions.

Studies related to surface charge decay aimed at identification of contributions of different mechanisms on charge relaxation on polymeric surface in air. In order to obtain decay characteristics, surface potentials resulted from impulse corona charging were measured on thick flat samples of high temperature vulcanized (HTV) silicone rubber. First, charge decay due to bulk neutralization was studied by preventing other mechanisms. Further, the influence of surrounding gas on decay rates was studied by performing experiments utilizing different levels of concentrations of free ions in air. Finally, a contribution of surface conduction to charge decay was evaluated utilizing decay characteristics measured on materials samples aged by means of corona treatment. In this case, effect of moisture content in the surrounding gas environment was also analyzed. The obtained decay characteristics were compared and were further utilized to deduce decay rates as well as materials properties, such as field dependent apparent bulk conductivities and trap density distributions.

Effect of surface charge on flashover performance of polymeric insulators was studied by means of experiments and numerical simulations. Experimental study aimed at obtaining dc flashover voltages of a cylindrical composite model insulator in presence of surface charges whereas the simulations focused on theoretical predictions of the flashover voltages. The calculation model was developed based on utilizing criteria for inception, propagation and sustenance of streamer discharges in air. The model was validated by comparing the calculated flashover voltages with the experimental ones measured within this project as well as with those provided in available literature. Hereafter, the model was adapted to the geometry of the studied insulator and effects of polarity, magnitude and location of surface charges as well as the influence of the material on impulse flashover characteristics were investigated. The obtained regularities of the flashover characteristics were analyzed in terms of electric field distributions in the vicinity of insulator surface.

## 1.2 Outline of the thesis

The research work packages mentioned above are presented in this thesis as follows:

Chapter 2 – *Literature review*, provides an overview of the current state of research and understanding in all three subject areas: charging, charge decay and effect of charges on flashover performance of polymeric insulators, studied within the project. First section focuses on charging of polymeric surfaces with special emphasis on corona charging. Second section discusses charge decay mechanisms, basic principles of surface charge measurements and related previous studies. The last section focuses on reported experimental observations of the effect of surface charge on withstand performance of polymeric insulation. Also it includes a discussion on streamer flashover criteria and its application in presence of surface charges.

Chapter 3 – *Corona charging of polymeric materials*, focuses on computer modeling and simulations related to charging of polymeric surfaces. The chapter starts with a short discussion on physical background of the mathematical model used to simulate corona discharges. Thereafter, the formulation, implementation and validation of the model are discussed. The last two sections present results of the simulation studies on positive impulse corona modes in air and on surface charging by impulse corona.

Chapter 4 – *Surface charging and charge decay on HTV silicone rubber*, presents experimental studies related to surface charging and charge decay on 2 mm thick flat polymeric samples in air. The first section provides detail of the experiments. The second section presents charge decay characteristics measured under dominating influence of bulk neutralization whereas the two following sections report the results on contributions of gas neutralization and surface conduction to charge decay. The chapter finishes with a comparison of the characteristics obtained under these different conditions.

Chapter 5 – *Surface charging of cylindrical polymeric insulator*, presents experimental studies related to charging of polymeric model insulators. The chapter starts with a description of the experimental setups used, the test procedures and the  $\Phi$ -matrix method. Further, surface charge profiles resulted from charging by an external dc corona source and pre-stressing with a dc voltage are presented and discussed.

Chapter 6 – *Effect of surface charge on dc flashover performance*, starts with a presentation of the experimental results of dc flashover tests carried out on a model of polymeric insulator. The second section discusses the application of streamer criteria for calculating flashover voltages. Last section compares the calculated flashover voltages with the experimentally obtained ones for the model insulator.

Chapter 7 – *Prediction of impulse flashover performance of insulators in presence of surface charges*, presents a simulation study on impulse flashover voltages of a post insulator by means of the same model as the one presented in Chapter 6. First two sections are focused on model validation for impulse flashover voltages and modification of the model when adapting to the post insulator. Last section presents model predictions together with explanations of the observed regularities based on analyses of electric field distributions.

Chapter 8 – *Conclusions*, is a collection of conclusions drawn from the results presented in Chapters 3-7.

Chapter 9 – *Future work*, suggests several paths to continue the project.

## 1.3 List of publications

This thesis is mainly built on the research that is presented in the following publications:

- **Sarath Kumara**, Bin Ma, Yuriy V. Serdyuk and Stanislaw M. Gubanski, “Surface charge decay on low-conductive polymer: effect of material treatment by corona discharges”, *IEEE Transactions on Dielectrics and Electrical Insulation*, Vol. 19, No. 6, pp. 2189-2195, December 2012.
- **Sarath Kumara**, Shahid Alam, Imtiaz R. Hoque, Yuriy V. Serdyuk and Stanislaw M. Gubanski, “DC flashover characteristics of a cylindrical insulator model in presence of surface charges”, *IEEE Transactions on Dielectrics and Electrical Insulation*, Vol. 19, No. 3, pp. 1084-1090, June 2012.
- **Sarath Kumara**, Imtiaz R. Hoque, Shahid Alam, Yuriy V. Serdyuk and Stanislaw M. Gubanski, “Surface charges on cylindrical polymeric insulators”, *IEEE Transactions on Dielectrics and Electrical Insulation*, Vol. 19, No. 3, pp. 1076-1083, June 2012.
- **Sarath Kumara**, Yuriy V. Serdyuk and Stanislaw M. Gubanski, “Surface charge decay on polymeric materials under different neutralization modes in air”, *IEEE Transactions on Dielectrics and Electrical Insulation*, Vol. 18, No. 5, pp. 1779-1788, October 2011.
- **Sarath Kumara**, Yuriy V. Serdyuk and Stanislaw M. Gubanski, “Surface charge decay of corona charged HTV silicone rubber samples due to bulk conduction”, *Proceeding of the 22<sup>nd</sup> Nordic Insulation Symposium (Nord-IS 11)*, pp. 75-78, Tampere, Finland, June 2011.

### 1.3. List of publications

- **Sarath Kumara**, Yuriy V. Serdyuk and Stanislaw M. Gubanski, “Simulation of surface charge effect on impulse flashover characteristics of outdoor polymeric insulators”, *IEEE Transactions on Dielectrics and Electrical Insulation*, Vol. 17, No.6, pp. 1754-1763, December 2010.
- **Sarath Kumara**, “Electrical charges on insulator surface and their impact on withstand performance”, Licentiate thesis, Department of Materials and Manufacturing Technology, Chalmers University of Technology, Gothenburg, Sweden, 2009.
- **Sarath Kumara**, Yuriy V. Serdyuk and Stanislaw M. Gubanski, “Charging of polymeric surfaces by positive impulse corona”, *IEEE Transactions on Dielectrics and Electrical Insulation*, Vol. 16, No. 3, pp. 726-733, June 2009.

Other publications within the project, not included in this thesis.

- **Sarath Kumara**, Yuriy V. Serdyuk and Stanislaw M. Gubanski, “Calculation of corona voltage-current characteristics in air”, Proceeding of the 4<sup>th</sup> International Conference on Industrial and Information Systems (ICIIS 09), pp 489-492, Pedadeniya, Sri Lanka, December 2009.
- **Sarath Kumara**, Yuriy V. Serdyuk and Stanislaw M. Gubanski, “Surface charge relaxation in silicone rubber and EPDM”, 2009 Annual Report IEEE Conference on Electrical Insulation and Dielectric Phenomena (CEIDP), paper 2B-16, Virginia Beach, USA, October 2009.
- **Sarath Kumara**, Yuriy V. Serdyuk and Stanislaw M. Gubanski, “Measurement and simulation of positive impulse corona current”, Proceeding of the 21<sup>st</sup> Nordic Insulation Symposium (Nord-IS 09), pp. 117-120, Gothenburg, Sweden, June 2009.



## **2 Literature review**

Surface charging of polymeric materials has been utilized extensively over decades in relation to various applications such as electrets, electrooptics, and surface modification, etc. [9, 10]. In the field of electrical insulations, which is the primary interest of this study, dynamics of charges appearing on surfaces of insulating materials (or resulting surface potentials) due to different processes has been studied to obtain material properties related to charge storage and transport. As an example, measurements of charge decay in [11-15] have been utilized to extract transport related quantities such as mobilities of charge carriers and/or bulk conductivities/resistivities whereas in [14, 16] similar approach was used to obtain surface trap energy distributions. Recently, several investigations were reported, e.g. [4, 6], where surface charging has been utilized to study its influence on flashover performance of materials. This chapter summarizes literature analyses related to the thesis subject, which focuses on three different topics: charging of polymeric surfaces, charge decay on polymeric surfaces and effect of surface charges on flashover performance of polymeric insulation systems.

### **2.1 Charging of polymeric surfaces**

Surface charging can be achieved by different techniques such as corona charging, contact charging, electron beam and polarization, etc. [10]. Among them, corona charging has been widely used due to possibility of better control over on the charge deposition process [9]. On the other hand, nowadays, phenomena associated with corona charging in air receive special attention in connection with the development of outdoor polymeric insulation systems operating at extremely high dc voltages [17] and exposed to impulse overvoltages caused by switching operations and lightning events. The experimental work presented in this thesis utilized either external corona or pre-stressing to charge materials surfaces. Thus other charging methods have been excluded from further discussions. Details on those techniques can be found elsewhere [9, 10].

### 2.1.1 Corona charging

Corona charging can be achieved by either external or internal sources. The latter can be a sharp conducting particle attached to one of the electrodes or a protrusion on the electrode of an insulation system [18]. External sources are usually sharp electrodes such as wires or needles connected to a high voltage source and mounted in the vicinity of the surface to be charged. An example of a more advanced system is a corona triode, where a grid electrode is located in the gap between the sharp corona electrode and material surface that allows controlling charge deposition process [9].

In all the systems mentioned above, charge carriers are generated by corona, which is a self-sustained electrical discharge taking place in electrode configurations providing strongly non-uniform electric field distributions [9]. Under such field conditions, discharge activity is localized in the vicinity of a sharp (i.e. most stressed) electrode, where gas becomes ionized due to extremely high field strength forming so-called ionization region. One of the crucial factors that determine the inception of corona is the availability of a free electron within the ionization region, which can trigger an avalanche. As a result of the ionization, charged species of both polarities are generated in gas. The carriers, having the same polarity as the high field electrode (positive ions and electrons in case of positive and negative corona, respectively), move towards the counter electrode under the influence of electric field set up by the electrodes and enter into a low field region (so-called drift region), where further ionization ceases. Thus, a complete breakdown of the insulation gap is prevented unless the applied voltage is sufficiently increased. In case of negative corona, electrons reaching the boundary of the ionization region are attached to electronegative components of air producing negative ions which move further towards the opposite electrode. In case of presence of a solid insulating surface, charge carriers can be deposited on it and form a surface charge layer. Depending on the magnitude and polarity of the applied voltage, corona discharge can be in one of the forms: burst pulses, streamer corona, continuous glow or Trichel pulses [9, 19]. The types of ions that may reach a dielectric surface depend on corona polarity and on conditions in the gas [9]. Thus in case of positive corona in air at atmospheric pressure, dominant charged species are hydrated ions in the form of  $(\text{H}_2\text{O})_n \text{H}^+$ , where  $n$  is an integer increasing with humidity. However at low humidity,  $(\text{H}_2\text{O})_n \text{NO}^+$  and  $(\text{H}_2\text{O})_n (\text{NO}_2)^+$  ions become dominant. At very low moisture content, considerable amount of those ions are unhydrated [9, 20]. In case of negative coronas in air, ionic species such as  $\text{O}^-$ ,  $\text{O}_3^-$ ,  $\text{CO}_3^-$  and  $\text{NO}_2^-$  appear and their relative fractions are highly dependent on air pressure. At atmospheric pressure,  $\text{CO}_3^-$  becomes dominant and relatively small portion of that can appear in the hydrated form,  $(\text{H}_2\text{O})_n \text{CO}_3^-$ , in presence of higher water contents [21].

Once a polymeric surface is subjected to charging from a corona source, charges will be deposited in the form of gaseous molecular ions, which are determined by the polarity of the corona and the surrounding conditions as discussed above. According to [22, 23], the ions reaching polymeric surface can charge it in two ways, either staying

as stable entities within a surface layer or transferring electrons into/from surface states (traps) in order to neutralize the incoming ions, thus charging surface states of a polymer to the same charge as incident ions. One should note that in both cases, the charges are initially located in energy states within the surface layer and need to acquire certain amount of energy (activation energy) in order to be released from the surface states for entering into mobile bulk states [23]. Issues related to presence of shallow or deep surface states, providing trapping sites for charge carriers, in polymeric material were discussed in [24-26].

### 2.1.2 Pre-stressing

When pre-stressing an insulator by applying a voltage below its flashover level, charging can be due to polarization, internal corona activities, charge injection at interfaces or combination of these mechanisms. When stressing an insulator with a dc voltage, a voltage source is usually switched on and then its output is increased gradually up to a desired level below a flashover threshold. During the transient, the electric field distribution around/in the insulator is of capacitive type and it is determined mostly by a displacement current. The field changes to a resistive type after certain time interval when the applied voltage comes to a steady-state. The process is associated with a charge build-up on interfaces between different materials (solid insulation and air) due to their different permittivities and conductivities [27]. In addition to this, the field strength at high pre-stressing voltages may become sufficient to initiate corona discharges at triple junctions or from edges of adjusted metallic objects (e.g., insulator flanges) and the mechanism of corona charging described above may contribute to the increase of the total amount of charges present on insulator surface. If the field strength is sufficiently high, charge injection from metallic electrode to the solid dielectric may take place. Typically, charge injection at metal-organic semiconductor interfaces is characterized through field assisted thermo-ionic emission (or Schottky emission) [24], resulting in an exponential relation between the injection current density and square root of the field strength. Similar injection law can be also applicable for polymeric materials. In addition to this classical theory, several alternative mechanisms have been proposed to account for charge injection into polymers [24].

### 2.1.3 Modeling of corona discharge in air

Even though the processes of charge deposition by corona charging are extensively documented, see e.g. [9, 28, 29], physical mechanisms associated with the dynamics of those processes are still not well understood. In this respect, utilizing computational models of corona discharge verified against experiments provides powerful tools for analyzing dynamics of charged species in air and at gas-solid interfaces, as well as for identifications of corona modes taking place in a particular electrode system under given conditions. Basic simulation studies on formation and development of corona in atmospheric air are usually performed in “classical” electrode arrangements such as

point-plane, rod-plane, coaxial cylinders and the most popular computational approach is based on continuity equations for fluxes of charge carriers coupled with Poisson's equation for the electric potential [30, 31]. Such model is utilized in the present study and is described in details in Chapter 3.

## 2.2 Surface charge decay

As previously mentioned, surface charge decay on polymers has been studied experimentally and theoretically over decades. In most of the cases, it has been analyzed by measuring the resulting surface potential. One of the effects, which enhanced the interest in this subject, was the “crossover effect” in potential decay characteristics observed on corona charged films by Ieda [32] and later by others researchers [21, 33]. It relates to a crossing of the surface potential decay curves measured after different initial magnitudes of charging conditions, after which the decay can appear faster for higher initial values. As the crossover effect has become a scope of many investigations, understanding of the phenomenon was improved, especially in line with the models of charge injection and electric transport mechanisms [15, 33-37]. Most of the reported charge decay experiments were performed on flat material samples, where the charged surface was open to surrounding gaseous medium and the opposite surface was in contact with a grounded metal plate (so called open circuit configuration). The majority of those studies were related to thin films, of thickness in  $\mu\text{m}$  range [15, 16, 33, 38], whereas only a few studies were carried out on thicker samples in mm range [39-42]. The primary objective of the present study has been to investigate charge relaxation in thick samples that are of interest for high voltage applications. Therefore, the following literature review focuses mainly on relevant experiments and simulations.

### 2.2.1 Decay mechanisms

Once deposited on a polymeric surface, electric charges will remain on it over a certain time determined by the efficiency of decay processes. In air under open circuit configuration, the decay can occur due to three main mechanisms, namely, bulk neutralization, surface conduction and neutralization by ions present in the gas phase (so-called gas neutralization) [32, 39, 40, 42-45]. In most of the reported studies, presence of one or two of the mechanisms have been neglected, either at the experiment design stage or when comparing the relative contributions from these processes. For example in [32], surface conduction on polyethylene was shown to be negligible because the decay rate was found to be almost independent of the sample surface leakage length. At the same time, gas neutralization was also considered insignificant because of negligible decay rate on thick samples. In contrary, it was concluded in [43] that bulk neutralization was the dominant decay mechanism for corona charged low density polyethylene films. In [39], all the three mechanisms were taken into account for interpreting the charge decay characteristics on silicone rubber,

epoxy resin and polytetrafluorethylen. It was suggested that either gas neutralization or bulk neutralization could become dominant depending on the material type and specific experimental conditions. Each of the above listed mechanisms is briefly discussed below.

### **Bulk neutralization**

Bulk neutralization represents the charge decay through the bulk of the solid material and can be due to intrinsic conduction, charge injection and polarization processes [10, 40]. The efficiency of the intrinsic conduction depends on rates of charge carrier generation and recombination as well as their mobility within material. The decay due to charge injection refers to bulk transport of injected charges and the dynamics of this process is governed by several physical factors, such as drift in the electric field, trapping, de-trapping, and recombination between charge carries of opposite polarity [23, 24, 46, 47]. Most of the theoretical models and interpretations of surface charge decay have assumed transport of injected charges as the dominating mechanism [34, 35, 48]. Contribution of dipolar polarization to the charge decay is mainly dependent on intensity of slow polarization processes in the considered material [10]. Once charges have been deposited on material surface, the resulting electric field triggers polarization of the bulk material which tends to screen out the surface charge and leads to apparent decrease of the measured potential.

### **Surface conduction**

Surface conduction refers to the charge leakage along the sample surface due to the tangential electric field, which appears when surface charge is distributed unevenly. Charge transport along a surface of a polymeric material can be due to carrier hopping through the localized surface states and/or through a surface film of adsorbed moisture [49]. This process results in a lateral expansion of the surface charges and can be quantified by means of surface conductivity, which strongly depends on external conditions, such as presence of pollution and level of air humidity [13, 49, 50]. It is also worth noting that this process alone may only yield a local charge rearrangement, while the total amount of charge on the surface remains preserved [44].

### **Gas neutralization**

The term “gas neutralization” is usually used to indicate a compensation or neutralization of surface charges by free ions attracted to the charged surface from the surrounding gaseous environment [42, 44, 45]. Free ions are always present in atmospheric air due to several background ionization processes. Being exposed to the electric field produced by the surface charges, some of the ions can be attracted to the gas-solid interface and occupy free surface traps. These ions interact with those deposited during charging by screening them out or by recombining with them [45]. In any case, the macroscopic effect is seen as a reduction of the surface charge (or potential). The critical factors that determine the efficiency of the charge decay due to

gas neutralization are concentrations of ions present in the gas phase, electric field strength in the vicinity of the charged region defining the capture volume and the energy depth of the surface states. As some of the factors are dependent on the electric field distributions in the experimental setup and in its vicinity, a general quantification of this mechanism is rather complicated.

### 2.2.2 Surface charge measurements

Surface charges while deposited on an insulating sample produce electric fields in both the material and in the surrounding gas environment. The strength of this field depends on material properties, dimensions of the sample, geometry of the experimental setup and eventual presence of nearby grounded objects. The resulting electric field yields a certain electric potential on the sample surface (so-called surface potential). Monitoring of the surface charge and its decay can be achieved through measurement of charge itself or by measuring the resulting electric field or the potential. Several techniques have been developed for such measurements. Thus, dust figure technique, which is simply a spreading of dielectric powder on the surface so that it attaches to the charged regions, can be used for direct detection of surface charges. As this method provides only a rough estimation of charge distribution and its polarity [51], it is not sufficient for quantitative estimations. Indirect detection of surface charges, i.e. by means of field or potential measurements, can be achieved using three kinds of instruments: induction probes, field mills and electrostatic probes [52]. Among them, electrostatic probes, which measure the surface potential, are widely used nowadays due to the non-contact nature of the method and its simplicity.

There are two basic kinds of electrostatic probes, capacitive probe and Kelvin probe [10, 51, 52]. In most of the cases, capacitive probe is made of a conductive sensor plate surrounded by a grounded guard electrode. When placed against the analyzed surface, it will acquire certain charge and, hence, a floating potential which is induced depending on the capacitances in the measuring system (basically probe to ground, surface to ground and probe to surface). Knowing the probe response characteristics, the actual surface charge density can be determined by measuring the induced potential. The main drawback of this method is that the latter strongly depends on the probe-to-surface distance. The other type of electrostatic probes, Kelvin probe, consists of a vibrating sensor connected to a feedback loop, which can be provided e.g. by an electrostatic voltmeter [10], an electrostatic field meter or ac feedback voltmeter [53]. Surface potential measurements presented in this thesis were performed by utilizing a vibrating sensor connected to a dc feedback electrostatic voltmeter, as discussed below in details.

#### Surface potential measurement with Kelvin probe

Figure 2.1 shows the schematics of the probe and induced voltages and equivalent capacitances when it is placed above a charged surface. Vibrations of the sensor result

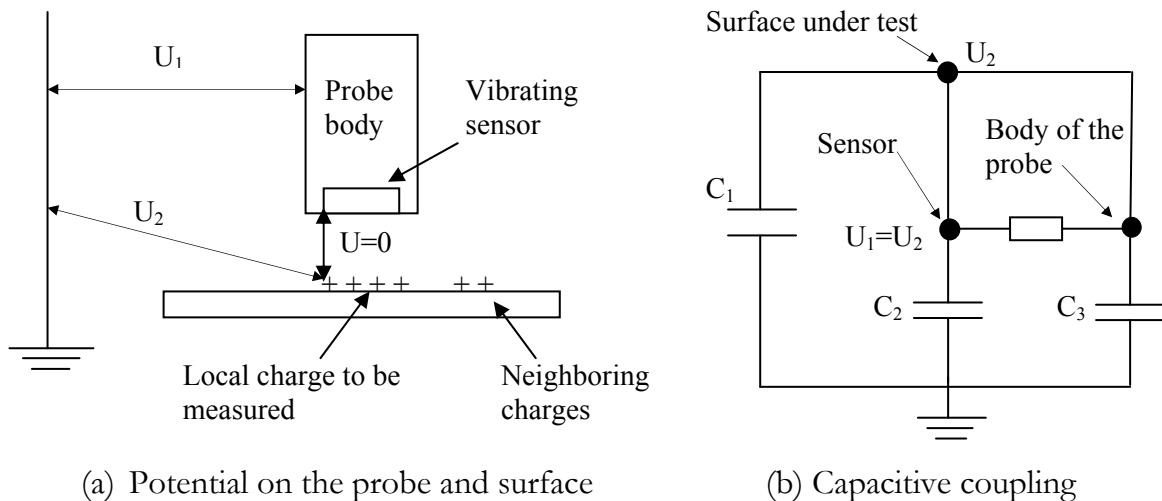


**Figure 2.1.** Kelvin probe placed above a charged surface. Capacitances;  $C_1$ -surface to the ground,  $C_2$ -sensor to the ground,  $C_3$ - probe body to the ground.

in certain current in or out from the probe. The Kelvin method is based on adjusting the voltage on the sensor to the voltage on the surface in such a way that the current becomes zero [54]. As the field between the probe and the surface also becomes zero, this method is usually referred as a field nullifying technique [53]. It provides three major advantages: (a) measurements are independent on the probe to surface distance at least within a certain range, (b) the risk of discharges between the probe and surface is avoided, and (c) measurement errors are reduced due to absence of capacitive coupling between the probe (both the sensor and the body) and the surface (see Figure 2.1b) [55]. One of the drawbacks of Kelvin probe is its high sensitivity to noise. Any electromagnetic or mechanical noise, which introduces offsets into the detected current, causes significant errors. This effect can be reduced by employing proper filtering and shielding [54]. Another limitation of the method is related to the necessity of utilizing small probe area and small distance between the probe and the surface for avoiding influences of neighboring charges on the results of the measurements and, thus, for achieving a good resolution. However, use of the probe with the recommended surface to probe spacing maintains a good resolution which is usually within a few mm.

### Calculation of the charge densities from measured potential

As mentioned above, deriving surface charge distributions from surface potential profiles measured by any kind of probe requires knowledge on relationship between the potential and the charge densities under exact conditions at which the measurements were performed. In general, this relationship can be obtained with the help of electrostatic field calculations, which may be either a simple analytical or a complex numerical problem, depending on the test object under consideration.

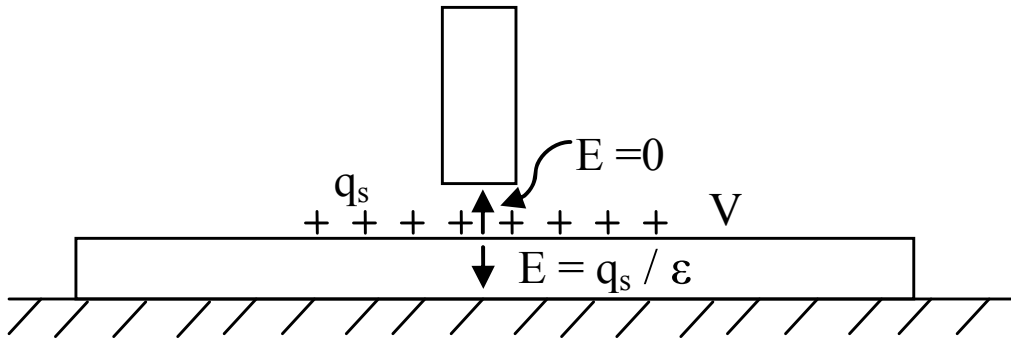


**Figure 2.2.** Electric field due to surface charge while measuring the potential using Kelvin probe.

Figure 2.2 illustrates a typical situation appearing during measurements on flat samples in open circuit configuration. As the probe potential is identical to the surface potential, the field strength between the tip of the probe and the surface becomes zero and the surface charge is only coupled to the grounded back electrode [14, 52]. When neglecting space charges in the material bulk and assuming that the surface is charged uniformly, a relation between the potential  $V$  and the charge density  $q_s$  may be denoted as:

$$V = \frac{d}{\epsilon} q_s \quad (2.1)$$

Here,  $d$  and  $\epsilon$  are the thickness and permittivity of the material, respectively. It is worth to mention that even for flat samples this simple relation is not accurate when tangential field component becomes significant due to non uniform charge distributions on the surface. This expression is not valid for more complex geometries such as cylindrical samples, which provide complex field structures with both normal and tangential field components. Those cases need to be analyzed with some other techniques such, for example, as  $\Phi$ -matrix method presented in [56]. A detail discussion on this method is included in Chapter 4, where a  $\Phi$ -matrix is utilized for calculations of charge distributions for a cylindrical insulator model.

### 2.2.3 Previous experimental work on charge decay

Since the primary concern of the present study is to analyze performance of the materials for high voltage insulation applications, the discussion here focuses on investigations performed with thick (mm range) materials samples. In this context, it is worth to mention that the related literature information is quite limited. Thus in [41], results of surface potential decay measurements on 2 mm thick ethylene-propylene-diene-monomer (EPDM) and silicone rubber (SIR) specimens were presented. The material surfaces were charged by lightning impulse or dc positive corona from a needle electrode placed at 1 mm above the sample surface in air. Potential distributions

along air-solid interface were measured using Kelvin probe within 15 minutes time intervals starting at 60 s after the charging. Both spatial and temporal variations of the surface potential were reported [14, 41, 57]. It was found that the potential profiles along the sample surface might appear as either bell-shaped or saddle-like, depending on the magnitude of the charging voltage, number of applied impulses and type of material specimen. The latter profile was attributed to back discharges from charged interface to the corona needle. Presented surface potential decay characteristics for the SIR (filled with alumina trihydrate, ATH) specimens showed faster surface charge relaxation as compared to EPDM and they were not sensitive to the polarity of the deposited charges.

In [39], surface potential decays on 10 mm thick cylindrical insulator samples placed in air and in sulfurhexafluoride ( $\text{SF}_6$ ) were measured for three types of materials: polytetrafluorethylen (PTFE), SIR and epoxy resin (EP). All the samples were charged by  $\pm 12.5$  kV dc voltage applied to a needle electrode placed at 10 mm from the sample and the measurements were performed using an electrostatic probe. Here also bell-shaped or saddle-like potential distributions were recorded depending on the type of the material: the former was obtained for SIR whereas the latter appeared with PTFE and EP. For all three materials, the decay characteristics acquired with smaller volume of air surrounding the samples resulted in lower decay rate as compared to that obtained in open space. This result indicated an important role of atmospheric ions in the surface charge neutralization process. Further, no significant differences between decay rates for positive and negative charges were observed.

A decay of surface potential on four types of 7 mm thick samples of bisphenolic epoxy resin was analyzed in [40]. The experiments were carried out using different charge deposition methods: corona charging, polarization and contact charging with several electrode geometries. Effects of charging method, electrode geometry and filler content on potential decay were studied. It was concluded that charging method, surface scratching, atmospheric conditions and initial value of the potential did not influence potential decay characteristics significantly.

Surface charge decay of 3 mm thick PTFE, EP and polyethylene (PE) samples, which were charged by ac and impulse corona, were studied in [42] by applying an induction type probe to measure surface field distributions. Experimental results on charging with impulse voltages showed that even though voltage polarity did not affect the residual field profiles along the sample surface, it modified surface charge distribution observed with dust figures. The bell-shaped field profiles recorded at relatively low voltages evolved into saddle-like distributions with increased magnitude of the applied charging impulse. This observation is in agreement with the results reported in [39, 41]. The measured time variations of the electric fields after charging by impulse voltage indicated that surface charge decay in air is much faster than that in  $\text{SF}_6$ . It was also concluded that the observed quicker charge relaxation at the centre of the sample was

due to neutralization of surface charges by ions from the surrounding gas volume (i.e. gas neutralization).

## 2.2.4 Surface potential/charge decay modeling

The surface potential measured during the charge decay is not only due actual surface charging of the sample. Other sources that contribute to the surface potential are dipolar polarization and space charges built up in the material bulk. Depending on the experimental conditions, one or more sources can be active and need to be taken into account. One of the ways to analyze the processes is to develop computer models allowing for considering relevant potential decay sources. Such models are seen today as powerful tools to understand physical mechanisms responsible for the surface potential and charge decay. This section focuses on summarizing published works presenting computational models of charge transport in polymeric insulation materials.

### Theories related to potential decay

In most of the cases the modeling of potential decay assumes that the material sample is charged instantly at time  $t = 0$  and afterward is kept in an open circuit configuration. For such a case, current continuity equation can be written at any point inside insulation as [10]:

$$\frac{\partial D}{\partial t} + \sigma E + \sum_i \mu_i \rho_i E = 0 \quad (2.2)$$

Here, the first term is related to the dielectric displacement  $D$  and it represents the so-called displacement current density, which is dependent on polarization inside the material since  $D = \epsilon_0 E + P$ , where  $E$  is the electric field strength and  $P$  is polarization,  $\epsilon_0$  is the permittivity of vacuum. The second term represents the current density due to intrinsic conductivity  $\sigma$  of the material. The third term describes the current density due to drift of injected charge carriers into material bulk. Here,  $\mu$  and  $\rho$  are the mobility and the density of a particular charge carrier, respectively. One can observe that the sum of these current densities is zero due to the open circuit configuration and the three terms contribute to the potential decay. However this formulation is only valid as long as the charge decay due to gas neutralization is prevented. This condition is usually satisfied when the zero field is reached between the probe and surface charge when using Kelvin probe. For a more complete analysis, surface conduction and charge injection need to be incorporated in the equation as a boundary condition on the gas-solid interface.

### Model based on intrinsic conduction

Once polarization is stabilized and space charge effect can be neglected, Equation 2.2 can be reduced to Equation 2.3, and the potential decay is solely governed by intrinsic conductivity  $\sigma$ . For a flat material sample with large dimensions as compared to its thickness, the problem can be treated as a one-dimensional and Equation 2.3 can be further simplified to Equation 2.4.

$$\varepsilon \frac{\partial E}{\partial t} + \sigma E = 0 \quad (2.3)$$

$$\frac{\partial V}{V \partial t} = -\frac{\sigma}{\varepsilon} \quad (2.4)$$

According to the Equation 2.4, a constant intrinsic conductivity should yield an exponential potential decay with a time constant equal to the ration between intrinsic conductivity and permittivity ( $\sigma/\varepsilon$ ) [10]. However, several hypotheses on charge generation, recombination and mobility are required to be introduced due to the fact that the conductivity depends on space charge density and mobility of charge carriers according to  $\sigma = \sum q\mu n$ , where  $q$  is the elementary charge. In consequence, this may lead to a field dependent conductivity and to more complex potential decay shapes than the exponential one.

An interpretation of the potential decay based on the assumption of continuous charge removal from the surface due to bulk conductivity is presented in [58]. Here, field dependency of the conductivity was taken into account by applying a modified Poole-Frankel model. The model has been utilized to reproduce the potential decay presented in [33] and it was concluded that the intrinsic conductivity model is sufficient to describe charge decay and, hence, to reproduce experimentally observed potential decay dynamics.

A recent work [14] also utilized the bulk conduction model to study the measured surface potential decay on EPDM and SIR by assuming a field dependent conductivity defined by Poole-Frankel model, where conductivity was assumed to be an exponential function of square root of the surface potential, as in Equation 2.5:

$$\sigma(V) = \sigma_o \exp\left(\beta_{PF} \sqrt{V}\right) \quad (2.5)$$

Here,  $\sigma(V)$  is the field (or voltage) dependent conductivity which can be calculated according to Equation 2.4 utilizing potential decay measurements. By observing the variation of  $\sigma(V)$  with  $\sqrt{V}$ , the parameter  $\sigma_o$  and Poole-Frankel coefficient  $\beta_{PF}$  can be determined. On the other hand, a theoretical value for  $\beta_{PF}$  can be calculated from Equation 2.6.

$$\beta_{PF} = \frac{q}{kT} \sqrt{\frac{q}{\pi\epsilon d}} \quad (2.6)$$

where  $k$  is Boltzmann's constant,  $T$  is temperature in  $K$ ,  $\epsilon$  is permittivity and  $d$  is the thickness of the sample. In [14], calculated and measured  $\beta_{PF}$  were compared for few type of material samples and a fair agreement was found in case of the material containing only small amount of additives.

In [44], surface potential decay on 10 mm thick polymeric samples was analyzed using an approach similar to the intrinsic conductivity model. However, it is worth to mention, that formulation of the model was not purely based on intrinsic conduction and it considered three charge decay mechanism, namely: (a) injection from gas-solid interface to the bulk, (b) surface conduction, and (c) surface charge neutralization due to background ionization in gas. Each of these processes was represented by an equivalent conductivity or current source. The model was utilized in [39] to simulate the measured surface potentials and total charge decay. A comparison of simulated results with experiments revealed that the dominant charge decay mechanism (gas neutralization or bulk conduction) determines the characteristic shape of surface charge and potential distributions during the relaxation.

### Model based on dipolar polarization

Presence of electric charges on a dielectric surface results in modifications of electric field inside the material and may activate dipolar polarization processes, which create additional surface charge layers inside the solid. Interaction of these charges with the pre-deposited charge is still not completely understood. However, under the assumptions of zero conductivity ( $\sigma = 0$ ) and no space charge ( $\rho = 0$ ) in the material bulk (i.e. no charge injection), Equation 2.2 yields  $\partial D / \partial t = 0$ . This means that free charge density on the surface is constant and the potential decay can be described solely by a time dependent dipolar polarization. A characteristic feature of almost all insulating polymers is that dielectric relaxation is a very slow process that is a consequence of internal molecular reorganization and complex interfacial phenomena taking place due to the existing electric field distribution [10]. The response of these materials can be modeled in a linear regime by a dielectric response function in order to calculate surface potential and free charge density on the sample surface. More detailed mathematical formulation and utilization of this approach to surface potential decay phenomena in polymers can be found in [10, 40, 59]. One can note that dipolar polarization itself does not act as a charge decay mechanism. However it can contribute to potential decay and, hence, affect the electric field, which may, in turn, influence the efficiency of the decay processes.

### Model based on charge injection and transport

Most of the published models on surface potential decay are based on hypotheses that the deposited charges are injected through gas-solid interface into the bulk and are transported inside solid material. The main reason of using this approach for most of the studies is a possibility to describe the observed cross-over phenomena. The mathematical representation of these models is achieved by utilizing continuity equations for charge carriers present in the solid, coupled with Poisson's equation for the field. In [34], a model based on volume conduction due to drift of charges was developed taking into account both time and spatial variations of the space charge. A comparison of the model performance with experimental data for polyethylene yielded predicted apparent charge carrier mobility of  $\sim 10^{-11}$  cm<sup>2</sup>/Vs that is close to typically cited values [46, 60]. In [35], similar model was extended to account for charge diffusion. This new formulation was used to obtain specific solutions for surface potential and space charge under certain conditions. Another version of injection and transport models was developed by considering instantaneous partial injection and field independent mobility of injected charges and it was used to study transient behavior of charge carriers generated by pulse illumination of a flat insulator sample [36]. Here, exact solution of the model was utilized to describe the dynamics of surface potential, space charge and electric field. Later, the same model was further modified to include trapping mechanisms in the bulk and it was used in a similar study based on some simplifying approximations [37]. In [48], a more sophisticated model was presented, which accounted for field dependent mobility and either instantaneous or time dependent injection. The former case was further studied considering field dependent injection efficiency. However, this model neglected charge trapping and transport due to diffusion. Surface potential decay characteristics of corona charged samples were obtained theoretically and compared with experimental data presented for polyethylene in [32]. The comparison showed that the model results reflected experimentally observed general features, such as initial steep decay for high initial surface potentials, almost flat decay curves for lower initial potentials and cross-over phenomena. Further theoretical studies suggested that with high initial potentials all surface charges are injected into the bulk within very short time whereas for low initial potentials little or no charge injection takes place. For intermediate potentials, injection process was considered to be time and field dependent. Further progress in developing computer models of surface charge relaxation has been achieved by introducing trapping and de-trapping processes to the transport model [33], where partial instantaneous injection and shallow trap modulated mobility were assumed. Here, an analytical solution obtained under certain approximations were utilized to calculate the transport and trapping parameters by fitting experimental surface potential decay characteristics for high density polyethylene samples. Recent study [15] also utilized an approach similar to [33], but using a simple power law relationship to describe the field dependency of the mobility. It is worth to mention that most of the models based on injection and transport have been developed for thin polymeric films in  $\mu\text{m}$  range and

assumed unipolar charge injection. Thus, the validity of those models for thick insulating polymers remains questionable.

### Model based on demarcation energy

If carrier's transit time is low compared to their mean characteristic de-trapping time, the potential decay becomes solely controlled by the de-trapping processes. In this model potential decay dynamics are governed by the progressive increase of the trap energy depth. Demarcation energy level,  $E_m$  represents the border between emptied states and filled states so that states located above  $E_m$  are emptied during the time spent since charge deposition, whereas states below remain frozen in-situ at that time. With the time passing,  $E_m$  changes and more states becomes emptied. Energy gap between  $E_m$  and the position of the extended state (mobility edge),  $E_o$ , can be described as [10, 16, 61-63]:

$$E_o - E_m = kT \cdot \ln(v_o t) \quad (2.7)$$

where  $v_o$  is the attempt to escape frequency in  $s^{-1}$ . The decay rate  $dV/dt$  is proportional to the de-trapping emission current  $I_d$ , which is caused by a movement of the carries excited from states near the demarcation energy level  $E_m$  into the conduction states. On the other hand  $I_d$  is proportional to trap density,  $N(E_m)$  and rate of change of  $E_m$  as illustrate by Equation 2.8. Thus, as can be seen in Equation 2.9, term  $tdv/dt$  provides an image of trap density distribution.

$$I_d \propto N(E_m) \frac{dE_m}{dt} = N(E_m) \frac{kT}{v_o t} \quad (2.8)$$

$$t \frac{dV}{dt} \propto N(E_m) \quad (2.9)$$

In [62, 63], the demarcation energy model was used to obtain an image of a trap density distribution corresponding to bulk states in thin polymeric films. The charging was realized by an electron beam, i. e., charges were injected into the material bulk and thereafter trapped. The same approach was utilized in [10] to treat results of surface potential decay measurements on corona charged thin films, where charges were initially trapped in surface states. Application of the model has been extended in [14] for obtaining surface trap density distributions on thick polymeric samples charged by corona. Similar approach is used in the present study to evaluate surface traps parameters of the analyzed materials. It should be noted however that the method may lead to unphysical results in cases when surface charge behavior is controlled by other mechanisms than those dominated by de-trapping from surface traps, e.g., polarization. However, as it was already mentioned, the latter is believed to not contribute to the potential decay under conditions of the present experiments.

## **2.3 Effect of surface charges on insulator flashover performance**

### **2.3.1 Experimental observations on surface charge effect**

It has been revealed by investigations performed on real polymeric insulators [3, 7], prototype insulators [6, 64-66] and material samples [4, 5, 67] that flashover voltages may be affected by the presence of surface charges. This section summarizes the results available in the literature. Even though the present study focuses on flashover performance of polymeric insulations in air, some of publications related to applications in SF<sub>6</sub> are also considered in the discussion.

#### **Experiments in air**

In [3], lightning impulse flashover voltages of a 15 kV high density polyethylene (HDPE) insulator were studied under three different conditions: dry, semi-wet and heavily wet. These three cases were used to trace the changes in flashover voltage introduced by surface charges accumulated during preceding flashover events. The authors observed a reduction of negative flashover voltages due to wetting. As saline water used for the wetting reduced the amount of charges on the surface, it was concluded that presence of negative charges on the insulator surface increases the negative impulse flashover voltage. Similar effect was observed in [4] for 2 mm thick flat silicone rubber samples, where existence of positive surface charges led to a reduction of the impulse flashover voltages while negative charge yielded their increase. Study [4] has been extended in [67] to investigate the effect of surface charge on lightning impulse flashover voltage for six different polymeric material samples: SIR and EPDM with and without ATH fillers. In [67], charging of the sample surfaces were achieved by application of few impulses with reduced magnitude and the results demonstrated that impulse flashover voltages were dependent on the polarity of deposited charges, the polarity of the applied impulse, the material type itself and the presence of fillers.

In [65] effect of pre-deposited surface charge on dc flashover voltage in air along cylindrical PTFE insulating spacer surface was studied. The investigations were carried out for both uniform and non-uniform field configurations by using various electrode systems. The presented results indicated a reduction of the negative flashover voltage both in uniform and non uniform field configurations due to presence surface charges of either polarity, a large scatter of the flashover voltage results in case of uniform field configuration as well as lack of significant effect on positive flasher voltage in non-uniform field configuration and presence of charges of either polarity.

In addition to direct studies on surface charge effects on flashover voltages, the influence of insulators surface charging on the results of impulse tests was reported in [8]. It has been observed that pre-breakdown or partial breakdown during withstand impulses resulted in charge deposition on the tested insulator surfaces. The accumulation of charges led to a gradual increase of the impulse breakdown strength during subsequent tests. As a consequence of the changing conditions on insulator surface after each breakdown or withstand, series of impulse tests on such insulators could not provide reliable information for determining the 50% flashover voltage levels or the statistical withstand voltage levels in accordance to the obeying standards. An obvious way to solve such problems is through neutralizing the deposited surface charges after each impulse application. This, however, makes the impulse testing more time consuming and expensive.

### Experiments in SF<sub>6</sub>

Due to extensive use of gas-insulated equipment, a significant number of publications report the results obtained for insulators operating in SF<sub>6</sub> environment. Thus in [5], variations of ac and dc breakdown strength of an SF<sub>6</sub> insulated electrode configuration affected by presence of surface charges on a nearby flat PTFE insulation sample (thickness of 5 mm and 10 mm) was presented. The sample was first charged in a point-plane electrode system and thereafter moved into the electrode arrangement for performing breakdown tests, which consisted of two hemispherical rods placed at a certain distance away from the sample surface. The experiments showed that presence of bipolar charge layer (with the net charge density of about  $-30 \mu\text{C}/\text{m}^2$ ) led to a reduction of positive dc and ac breakdown voltages by  $\sim 20\%$  and  $25\%$ , respectively. It was also mentioned that negative charge increased negative dc breakdown voltages by  $\sim 15\%$ .

Similar studies on prototype insulator samples in SF<sub>6</sub>-filled gas insulated systems (GIS) were also extensively reported in the literature (see, e.g., [6, 64, 66]). In [64], the investigation was performed on a prototype PTFE plain cylindrical insulator (20 mm in diameter and 10 mm long) placed in a plane-parallel electrode configuration kept at 0.1 MPa. Insulator surface was charged by applying a dc voltage to a needle mounted closer to the solid surface. The effect of surface charge accumulation on field intensification and positive impulse flashover voltage was reported. The key observations included a reduction of positive impulse flashover voltage level at presence of linearly or uniformly distributed positive surface charges greater than  $25 \mu\text{C}/\text{m}^2$  (45% reduction at  $70 \mu\text{C}/\text{m}^2$ ), lack of a significant effect on flashover due to presence of negative charges up to  $60 \mu\text{C}/\text{m}^2$  and a reduction of flashover voltage due to localized positive charge accumulation closer to the cathode (35% reduction at  $40 \mu\text{C}/\text{m}^2$ ). Based on these observations, it was concluded that only the charge distributions, which can cause a significant enhancement of the cathode field strength, effected the flashover voltage for small spacers in SF<sub>6</sub>.

### 2.3. Effect of surface charges on insulator flashover performance

In [66], the effect of surface charge on a particle contaminated insulator was studied using very similar (or the same) experimental setup as described in [64]. In order to represent the particle contaminated insulator, a well defined needle was placed on the insulator surface parallel with its symmetry axis and it was in contact with the anode electrode. Surface charging was achieved by application of dc voltage to the needle. The effect of surface charge accumulation on field intensification and impulse flashover voltage was reported for positive voltage stresses. According to the observations, positive charge resulted in an increase of flashover voltages (25% in presence of negative charge of peak density about  $59 \mu\text{C}/\text{m}^2$ ) whereas negative charge resulted in a decrease (21% in presence of positive charge of peak density about  $49 \mu\text{C}/\text{m}^2$ ). In [6] a similar electrode configuration was used at  $\text{SF}_6$  pressure of 0.1 MPa. However in this case, the needle was connected to the grounded electrode and surface charging was achieved by incomplete flashovers that occurred during application of lightning impulses to the ungrounded electrode. The maximum charge density reached  $200 \mu\text{C}/\text{m}^2$ . The measured voltage-time characteristics ( $v-t$  curve) for positive lightning impulses showed that positive charge caused  $\sim 40$  kV enhancement of insulation strength compared with the  $v-t$  curve for the non-charged insulator whereas the negative charging caused  $\sim 30$  kV reduction. It is worth to mention that one should be careful when generalizing such conclusions for electrode configuration other than one used for the experiments. For example the observations can be different if metal needle is connected to a cathode instead of anode, if the applied voltage is negative or if electrode configuration is symmetrical, i.e. without a needle, nearby grounded floors, etc.

In [7] an insulator of a three-phase 110 kV GIS was studied. A metal needle was connected to one of the phase conductors to trigger the flashover and to deposit surface charges. The charging was done by application of a dc voltage. The obtained 50% impulse flashover voltages and voltage-time characteristics for positive polarity showed that presence of positive charge increased the flashover voltage whereas negative charge decreased it that led to a conclusion that charges with opposite polarity with respect to the applied stress reduce the flashover voltages.

#### 2.3.2 Calculations of Flashover voltages in presence of surface charges

##### Flashover criteria

It is commonly accepted that in air gaps at atmospheric pressure at inter-electrode distances larger than a few centimeters, the breakdown is primarily caused by streamer mechanism [68]. Therefore a general procedure for estimations of flashover voltages by means of a mathematical model can be based on assumption of the so-called streamer inception criterion and the conditions for streamer propagation and sustenance, as presented in [69, 70]. The condition for streamer inception states that the number of free electrons in the active region (e.g. at the head of an electron

avalanche) must reach a critical value for providing space charge density that creates a local field comparable with the external applied field. This locally enhanced field leads to strong ionization and, hence, to further increase of the number of charge carriers forming self-sustained streamer channel. Mathematically, this condition can be evaluated by integrating the effective ionization coefficient  $\alpha'$  in the active region along the critical line, as shown in Equation 2.10.

$$K = \int_0^{x_c} \alpha'(E) dx \quad (2.10)$$

Here,  $x_c$  is the distance along the critical line from the electrode surface to the boundary of the ionization region, where the effective ionization coefficient may eventually become zero depending on the field structure. Once the integral  $K$  reaches the value corresponding to a critical number of electrons, streamer initiation takes place. Further propagation of the streamer into the inter-electrode gap for relatively long distances requires some energy input from the external field [71]. The condition for streamer propagation in air is that the average electric field along the critical line should be greater than  $\sim 0.5$  MV/m for positive (cathode directed) streamers and at least 0.8 MV/m for negative ones [72-74]. The condition for streamer sustenance defines the external field, which has to be strong enough to overcome random thermal motion of gas molecules, so that photoelectrons producing secondary avalanches are able to drift into the high field region around streamer head. To satisfy this requirement, the minimum electric field along the critical line must be stronger than 60 kV/m [69].

### **Application of streamer criteria in presence of surface charges**

An attempt to utilize the above discussed criteria for prediction of flashover characteristics accounting for surface charging has been undertaken in [75]. The model used was based on the assumption that a flashover is to be initiated by a streamer formed in a high field region and propagating along a field line where conditions for its propagation and sustenance are satisfied [69]. To check the validity of the approach, the experimental conditions described in [4] were implemented in the model. A charged spot with Gaussian profile was introduced at a fixed location on the material surface between electrodes. The results of the calculations for different combinations of polarities of the deposited charges and the applied voltages were found to be in a reasonable agreement with the experimental data [4]. Both measured and calculated results demonstrated that the flashover voltages were higher for the case of opposite polarities of the surface charges and the applied voltage than that in case of the same polarity. This effect was analyzed in [75] by considering electric field distributions between electrodes and it was attributed to local field distortions associated with the deposited charges.

### *2.3. Effect of surface charges on insulator flashover performance*

One of the crucial steps in applying this flashover criterion for insulators with surface charge is related to determination of the discharge path (i.e. critical line), which might be affected by the accumulated charges. If discharge propagates along the surface (completely or only in certain regions), the applicability of the flashover criteria, which is originally developed for gas media, is not well understood. Therefore, it is worth to discuss the experimental observations on flashover discharges in presence of nearby solid surfaces with or without surface charges.

Streamer propagation under uniform field and along cylindrical insulating surfaces was studied in [76]. One of the electrodes was connected to a negative dc voltage supply whereas another one was grounded. The streamer was initiated from a sharp point located in an aperture on a grounded electrode in such a way that it was at the same level and in contact with the insulator surface. The sharp needle was supplied with fast rising high voltage square pulses. Based on the experiments performed for different insulating materials, it has been observed that the field required for stable streamer propagation along the insulating surface was higher than that for the propagation in air alone. By referring to [77], it was suggested that additional attachment process due to presence of insulating surface was responsible for the necessary higher propagation field. Further, it was observed that both the propagation field and streamer velocity were dependent on the type of insulating material. Another study [78] performed by the same authors on insulators having different profiles showed that those characteristics were also dependent on the the insulator profile.

Similar study was conducted for non-uniform field configurations (rod-plane electrodes) in [79]. A cylindrical insulator sample, 12 cm in length, was placed vertically on the grounded electrode in such a way that it touched the tip of the rod. Flashover tests were performed by applying standard switching impulses of positive polarity to the rod electrode. According to the observations, presence of the insulating surfaces resulted in higher 50% breakdown voltages as compared to the case with air alone. It was also reported that flashover path was dependent on the applied voltage stress. During the flashover at voltages close to the 50% flashover voltage, the discharge took place in air whereas for higher voltages it propagated along the surface. Similar experiments for positive lightning impulses were presented in [80]. In contrast to the switching impulse case, the 50% flashover voltages decreased due to presence of insulation samples. It was suggested that local field enhancement at the rod electrode due to the presence of solid insulator was the main reason for the reduction. However, similarly to switching impulses, flashovers took place in air rather than along the surface. It was mentioned that surface charge accumulation could be the reason for such behavior. Studies with negative lightning and switching impulses were presented in [81], where the 50% flashover voltages in presence of insulting surfaces were reduced as compared to air alone for negative impulses, irrespective of the shape of the impulse. However, in contrast to the positive case, discharges at 50% flashover voltages propagated along the surface. This behavior could be due to the fact that negative corona more likely propagated along the surface than in air.

In [82], an effect of negative ions on the propagation of discharges across insulating surface mounted between concentric electrodes was investigated experimentally. Measurements were performed for positive discharges caused by lightning impulse voltages. From the presented results, it could be observed that excess of negative ions yielded an increased amount of charges and wider expansion of the charge spot in case of corona discharges. It was claimed that this observation is due to the detachment of ions from the surface in the field of the streamer tip, followed by collisional detachment of electrons. However those negative ions did not result in any significant effect in the mean flashover voltage.

Characteristics of positive streamer discharges developing along negatively charged different types of polymeric insulation surfaces were presented in [83]. It was reported that both the magnitude of the discharge current and the propagation speed increased due to the presence of an insulating surface. The authors claimed that this behavior was due to increased ionization intensity resulting from higher ionization potentials of the surfaces and/or field enhancement caused by the solid insulation itself and by the deposited negative charges. On the other hand, regardless of the increased ionization, a minimum voltage required for stable propagation was increased due to the presence of the insulation surface.

In [84], impulse breakdown characteristics of rod-plane gaps with and without glass rod (installed between the electrodes) have been studied experimentally. As the solid insulation used was not a polymeric material, results related to breakdown are not discussed here. However one of the interesting observations from this study was that positive discharges took place through air whereas negative ones followed the insulator surface.

According to the above discussed reports, it is clear that utilizing the streamer flashover criteria for solid insulation in presence of surface charges needs some extra considerations related to field enhancement caused by the solid insulation itself, field enhancement or reduction due to possibly deposited charges, necessity of selecting proper discharge path for evaluation of the flashover criteria, accounting for additional charge generation (in the form of emission, detachment or photoionization) or loss (attachment) processes associated with solid surfaces and/or deposited charges if discharge propagates along the surface. The first two issues related to field conditions can easily be accounted for by proper field calculations including solid insulation with surface charges. Even though the independent studies [79-81] and [84] discussed above showed that positive discharges take place in air and negative ones follow the surface, generalization of these observations need more experimental evidences with different materials under different voltage stresses. The fourth issue (additional charge generation/loss processes) can be integrated into flashover criteria by modifying the effective ionization coefficient correspondingly. However, this can be rather difficult due to the lack of required material characteristics.

## **3 Corona charging of polymeric materials**

This chapter focuses on simulation study of charging of polymeric material surfaces by corona discharges in air under positive impulse voltage conditions. External (circuit current) and internal (space charge densities and electric fields) characteristics associated with the corona charging are analyzed by means of computer simulations. The developed model is validated by comparing simulated and measured corona currents in a needle-plane electrode arrangement. Further, the verified model is used to identify the corona modes depending on the magnitude and the rate of rise of the applied voltage impulses. Further the model is employed to investigate the charging process of a polymeric material surface. Dynamics and distributions of space charges and associated electric fields during charging by two different corona modes (glow and burst coronas) are analyzed and compared.

### **3.1 Physical background**

Corona discharge appears when electric field strength at the surface of an electrode exceeds the ionization threshold of a gas and leads to generation of high amount of free charge carriers in an initially electrically neutral gas volume. In the present study, corona in air is analyzed and it is assumed that three generic types of charged particles (electrons, positive ions and negative ions) take part in this process. Once an external electrical field is applied to a gas medium, various processes leading to charge generation and loss can be activated depending on the morphology of the electrode system, nature and conditions of the gas (pressure, temperature), strength of the applied electric field and its variation with time, etc. These processes include various types of ionization (due to electron impact, photo-ionization), attachment of electrons to neutral molecules, detachment of electrons from negative ions, recombination between opposite charges, emission from electrode surfaces and secondary emission from the cathode [85]. As our study is focused on positive corona discharge in air, only the relevant processes such as electron impact ionization, background ionization,

attachment, detachment and recombination are further considered. In addition to that, transport of the charges due to drift and diffusion in the field is also discussed.

### 3.1.1 Charge generation mechanisms

Even at zero field conditions certain amount of charged particles are present in air, which are produced by cosmic radiation and presence radioactive substances in the earth and in atmosphere [86]. This involves generation of both free positive ions and electrons, which remain normally in equilibrium, and is usually referred to as background ionization. The rate of the background ionization,  $S_0$ , is  $\sim 1-10$  ion pairs/( $\text{cm}^3 \cdot \text{s}$ ) that leads to a permanent presence of  $\sim 10^3$  ion pairs/ $\text{cm}^3$  [87].

When electrons are accelerated in an applied electric field, non-elastic collisions take place between these electrons and neutral atoms/molecules at certain field strength. If the electron energy, which an electron gains from the field during the movement between two collisions (so-called free path), is higher than the ionization potential of the gas, new electrons and positive ions are generated. This mechanism, namely electron impact ionization, is the most important charge generation process in the bulk of a gas discharge [85]. Its intensity is characterized by Townsend's ionization coefficient,  $\alpha$ , i.e. the number of ionization events produced by a single electron on a unit length path. The ionization coefficient  $\alpha$  is a field dependent quantity. Its value for different gases can be found in the literature in forms of empirical expressions and measured data [88-90].

Another mechanism providing free electrons in air is their detachment from negative ions. As the name implies, electron detachment is the opposite process to the electron attachment (considered below). Detachment can be characterized using corresponding rate coefficient or detachment frequency, which are determined as a function of ion temperature or reduced electric field [91].

### 3.1.2 Charge loss mechanisms

Certain atoms and molecules in gaseous medium having non-zero electron affinity (e.g.,  $\text{O}_2$ ,  $\text{CO}_2$ ,  $\text{H}_2\text{O}$ ) can readily acquire a free electron to form a stable negative ion. This process, called electron attachment, results in removing free electrons from the gas and generation of negative ions. The attachment is an important and sometimes the main mechanism of electron losses in electronegative gases and in gas mixtures containing electronegative additives. The rate of the attachment can be characterized using an attachment coefficient,  $\eta$ , which is similar to  $\alpha$  for ionization process and strongly field dependent [88-90].

As concentrations of both positive ions and electrons are significant in the bulk of a gas discharge, there is a probability for electrons to recombine with positive ions upon

collisions. This process may take place at certain energy of electrons and, depending on the way in which the excess energy is released, different types of electron-ion recombination reactions, such as radiative, dissociative and three-body, can be identified [85]. Electron-ion recombination results in loss of both electrons and positive ions. The process is characterized by a recombination coefficient,  $\beta_{ei}$ , which is  $\sim 5 \cdot 10^{-8} \text{ cm}^3\text{s}^{-1}$  for air under normal conditions [91]. Recombination between negative and positive ions normally takes place in electronegative gases, where negative ions are present. At low pressure, ion-ion recombination happens through two-body collisions, whereas at moderate and high pressures it occurs through three-body collisions. The ion-ion recombination coefficient,  $\beta_{ii}$ , for air at atmospheric pressure is usually defined as a function of ion temperature [91].

### 3.1.3 Charge transport mechanisms

Application of an external electric field to a gas containing charged particles results in their movement in the direction (or opposite, depending of the sign of the charge) of the applied field in addition to their random motion. This directed movement is called drift and its average velocity, called drift velocity  $w$ , depends on the applied field, the charge and the mass of the particles involved, pressure, etc. The ratio of the drift velocity to the electric field is known as mobility,  $\mu$ , and it is widely used to characterize the charge transport due to drift. Typically, the mobility is field dependent for most of the gases. In the case of electron transport in some common gases and gas mixtures, including air, several empirical relations can be found describing  $\mu$  or  $w$  as functions of the reduced electric field [89, 91]. In [88-90], measured dependencies of  $w(E/N)$  can be found as graphs or tables. For ionic drift, constant mobility values are usually assumed over a wide range of the reduced electric field strength [91, 92].

If concentration of particles moving in a gas volume is spatially non-uniform, charge transport takes place from regions with high particle concentration to regions with low concentration in order to minimize the concentration gradient [85]. Charge transport due to this mechanism is called diffusion and it is characterized by the diffusion coefficient,  $D$ . In the case of electron transport in gas discharge plasma,  $D$  can be estimated based on the measured drift velocity  $w$  and ratio of the  $D/\mu$ , which can be found in literature for common gases [89, 91]. Typically  $D$  for the ionic transport is calculated using the well known Einstein relation,  $D/\mu = kT/q$ , which is valid up to moderate field strength values, under which swarm of ions are in thermal equilibrium with the gas molecules [19]. Here  $k$ ,  $T$  and  $q$  stand for Boltzmann's constant, ions temperature and elementary charge, respectively.

## 3.2 Mathematical model

### 3.2.1 Model equations

Under certain assumptions [93], the physical phenomena discussed in previous section can be mathematically described using so-called zero-moment of Boltzmann's equation. Such description implies continuity equations (mass conservation) for each generic kind of charge carriers and Poisson's equation for the electric potential, which are coupled through field dependencies of kinetic/rate coefficients and net space charge density [87]:

$$\partial n_e / \partial t + \nabla(-n_e \mu_e \mathbf{E} - D_e \nabla n_e) = S_e \quad (3.1)$$

$$\partial n_p / \partial t + \nabla(n_p \mu_p \mathbf{E} - D_p \nabla n_p) = S_p \quad (3.2)$$

$$\partial n_n / \partial t + \nabla(-n_n \mu_n \mathbf{E} - D_n \nabla n_n) = S_n \quad (3.3)$$

$$\nabla(\epsilon_o \nabla \phi) = -q (n_p - n_e - n_n), \mathbf{E} = -\nabla \phi \quad (3.4)$$

Here,  $n$  stands for the charge carrier density,  $m^{-3}$ ;  $D$  is the diffusion coefficient,  $m^2 s^{-1}$ ;  $\mu$  is the mobility,  $m^2 V^{-1} s^{-1}$ ;  $\mathbf{E}$  is the vector of electric field,  $V m^{-1}$ ;  $\phi$  is the electric potential, V;  $t$  stands for time, s; and  $S$  specifies source terms (rates of the processes in discharge plasma),  $m^{-3} s^{-1}$ ;  $q = 1.6 \cdot 10^{-19}$  C is the elementary charge, and  $\epsilon_o = 8.854 \cdot 10^{-12}$  Fm $^{-1}$  is the permittivity of vacuum. Subscripts  $e$ ,  $p$  and  $n$  indicate the quantities related to electrons, positive ions and negative ions, respectively.

The first terms in brackets under the gradient operator in Equations 3.1-3.3 describe drift of charges in the field with corresponding velocity  $\mathbf{w} = \mu \mathbf{E}$ , while the second terms represents diffusion of charges. The negative sign in the drift terms of Equations 3.1 and 3.3 indicates that the velocity is in the opposite direction to the field for negatively charged particles. The selected values/expressions for mobility and diffusion coefficient for each type of charge carriers are given in Table 3.1. The dependencies of the parameters on electric field strength are taken into account.

The source term for each kind of charge particles in Equations 3.1-3.3 represents the net effect of several generation and loss mechanisms described earlier in Section 3.1. The rates of charge generation/loss are calculated using corresponding coefficients listed in Table 3.1:

$$\begin{aligned}
S_e &= \alpha n_e |\mathbf{w}_e| - \eta n_e |\mathbf{w}_e| - R_{ei} n_e n_p + \nu_{\text{det}} n_n + S_0 \\
S_p &= \alpha n_e |\mathbf{w}_e| - R_{ei} n_e n_p - R_{ii} n_p n_n + S_0 \\
S_n &= \eta n_e |\mathbf{w}_e| - R_{ii} n_p n_n - \nu_{\text{det}} n_n
\end{aligned} \tag{3.5}$$

Note that the source terms shown are dependent on the local electric field strength, which is obtained by solving Equation 3.4 accounting for the local density of the space charge (right hand side of the equation).

**Table 3.1.** Rate coefficients used in the model.

Parameter	Charge carrier	Value	Reference
Mobility, $\text{m}^2\text{V}^{-1}\text{s}^{-1}$	Electrons	$w_e(E/N)$ *	[88]
	Positive ions	$1.8 \cdot 10^{-4}/\delta$ **	[92]
	Negative ions	$2.7 \cdot 10^{-4}/\delta$	[92]
Diffusion coefficient, $\text{m}^2 \text{s}^{-1}$	Electrons	$D_e / \mu_e(E/N)$	[88]
	Positive ions	$D_{p,n} / \mu_{p,n}(E/N)$	[91]
	Negative ions		
Ionization coefficient, $\alpha$ , $\text{m}^{-1}$		$\alpha/N(E/N)$	[88]
Attachment coefficient, $\eta$ , $\text{m}^{-1}$		$\eta/N(E/N)$	[88]
Detachment coefficient, $k_{\text{det}}$ , $\text{m}^3 \text{s}^{-1}$		$k_{\text{det}}(E/N)$	[91]
Recombination coefficients, $\text{m}^3 \text{s}^{-1}$	electron-ion, $R_{ei}$	$5 \cdot 10^{-14}$	[91]
	ion-ion, $R_{ii}$	$R_{ii}(E/N)$	[91]
Background ionization rate ( $S_0$ ), $\text{m}^{-3}\text{s}^{-1}$		$10^6$	[94]

\*  $N$  is the gas density,  $\text{m}^{-3}$ . \*\*  $\delta$  is the relative air density.

### 3.2.2 Implementation

The geometry of the needle-plane electrode system, which is the selected electrode configuration for this study, is simplified and reduced to a two dimensional representation, utilizing its rotational symmetry. The resulting computational domain is shown in Figure 3.1. The model is implemented in COMSOL Multiphysics package, which is based on finite element method. The package's "Convection and diffusion, transient analyzes" and "Electrostatics" application modes are used to implement the system of Equations 3.1-3.4 together with boundary conditions shown in Figure 3.1.

The applied impulse voltage is specified by means of a double exponential function of time with appropriate time constants. The equations are solved using time dependent solver. The discharge current,  $I$  is calculated using Sato's equation 3.6 accounting for both conduction (first term) and displacement (second term) current components [95]. The conductive component of the current is associated with the drift and diffusion of charge carriers, whereas the component due to time varying electric field and geometric capacitance of the system is considered as the displacement current.

$$I = \frac{q}{V_a} \iiint_v (n_p w_p - n_e w_e - n_n w_n - D_p \nabla n_p + D_e \nabla n_e + D_n \nabla n_n) \cdot \mathbf{E}_L dV + \frac{\epsilon_0}{V_a} \iiint_v \frac{\partial \mathbf{E}_L}{\partial t} \cdot \mathbf{E}_L dV \quad (3.6)$$

Here  $V_a$  and  $\mathbf{E}_L$  stand for the applied voltage and vector of the Laplacian electric field. Though both the integrations are to be performed over the volume, they are reduced to surface integration in 2D computational domain considering the axial symmetry of the electrode system.

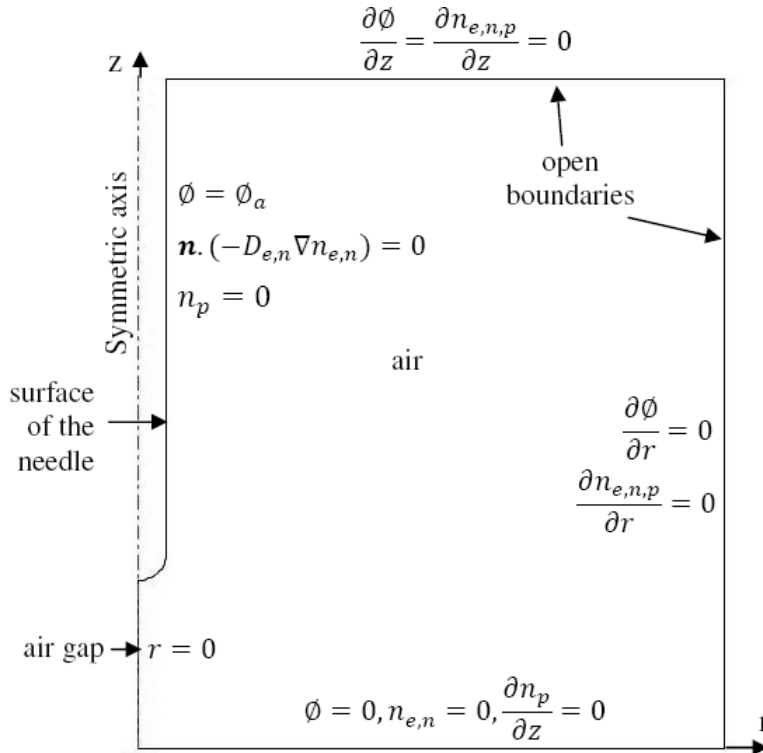


Figure 3.1. Computational domain,  $\mathbf{n}$  is the unit vector normal to the boundary.

### 3.3 Validation of the model

Before using the model for corona charging studies, it was verified by comparing the computed external circuit current waveforms with experimental results obtained for positive impulse corona in a 5 mm air gap. Model implementation and current calculation are similar to that described in the previous section. The experimental setup used for the measurements and comparison of the current waveforms are presented in the next section.

#### 3.3.1 Experimental setup

The schematic diagram of the experimental setup is shown in Figure 3.2. A needle electrode, having a hemispherical tip of diameter 0.95 mm was placed at 5 mm above the plane electrode and it was connected to a high voltage impulse generator (Haefely PU-12), which can supply lightning and switching impulses with magnitude up to 12 kV. The plane electrode was grounded in series with 7.48 k $\Omega$  shunt resistor and the current signal was monitored with an oscilloscope (Tektronix TDS 220). The applied impulse voltage was monitored from the built-in CRO output in the impulse generator. All the measurements presented in this section were carried out by applying a positive switching impulse of 350/1500  $\mu$ s (time to peak/time to half value).

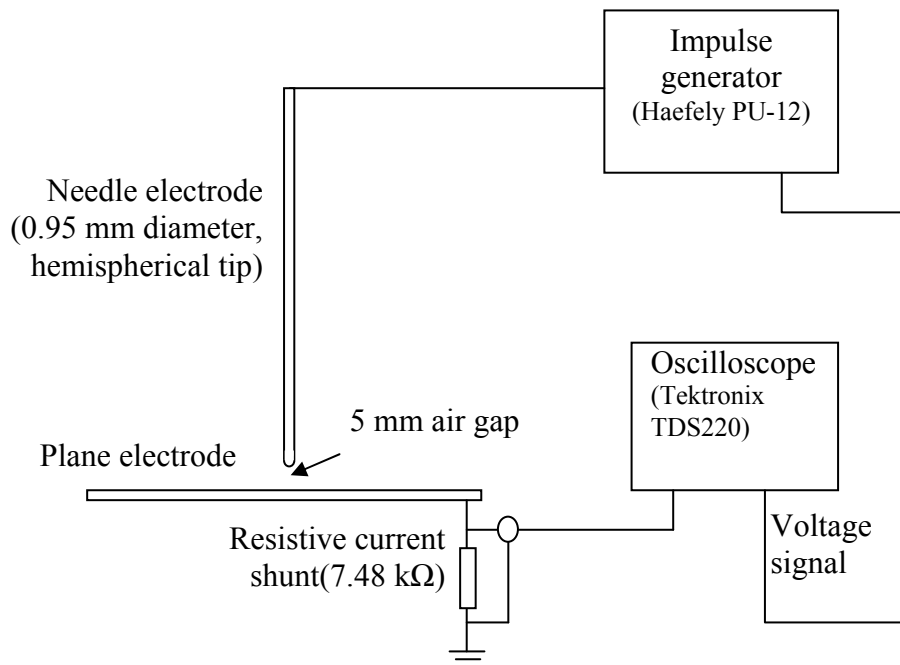


Figure 3.2. Experimental setup.

The test circuit was designed and arranged in a way to allow the minimizing parasitic discharge activities from locations other than the considered air gap. To ensure that the measured current corresponded to the corona from the point, an additional set of current measurements was carried out for each voltage level with the needle electrode removed, so that contributions from other part of the circuit could be eliminated in the recorded current traces.

### 3.3.2 Current at low voltage impulses

The applied voltage, measured and calculated current waveforms obtained with 3 kV switching impulse are shown in Figure 3.3. One can observe that the highest magnitude of the current was recorded at the time when the voltage impulse was applied ( $t \sim 0$ ) and then it decreased with time until it became zero at the instant corresponding to the peak of the voltage impulse. After that the current became negative, reached a maximum at  $t \sim 500 \mu\text{s}$  and then again decreased in magnitude. In general, the current shape follows variations of the time derivative of the applied voltage indicating dominating contribution of the capacitive term in Sato's equation (the second term in Equation 3.6). Hence, one may conclude that the current is a pure displacement current and there is no discharge activity at this voltage level. The comparison of the measured and computed current profiles shows that they are exactly the same and confirms the validity of the model at low applied voltages.

### 3.3.3 Current at high voltage impulses

Figure 3.4 shows the applied voltage, measured current, calculated total and displacement currents at 6 kV switching impulse. By comparing the measured and computed displacement currents, one can observe that at the beginning of the voltage impulse the current consists of only the displacement component. When the voltage reaches a sufficient level corresponding to corona inception, which is about 3.8 kV according to the calculations, the conduction current starts to flow and contributes to the total current that is reflected by the difference between the total and displacement currents. While considering the measured current shape, the discharge activity starts with a sharp current peak appearing at  $t \sim 180 \mu\text{s}$ , which is most probably a pre-onset streamer. Further, this peak vanishes at  $\sim 220 \mu\text{s}$  (before maximum of the applied voltage is reached) and it is transformed into a smooth current pulse, corresponding to glow corona. The calculated total current agrees well with the measured current except at the beginning of the discharge activity, thus validating the performance of the numerical model for diffusive corona (in this case glow corona) discharge. The agreement between the computed and measured currents, similar to that shown in the Figure 3.4, was obtained for all the studied voltage magnitudes. The discrepancy between the simulation and experimental results during corona inception current pulse is due to the fact that the discharge mechanism describing pre-onset streamers was not included in the numerical model as this study is focusing on diffusive types of coronas. The amount of charge generated during the discharge activity was evaluated by

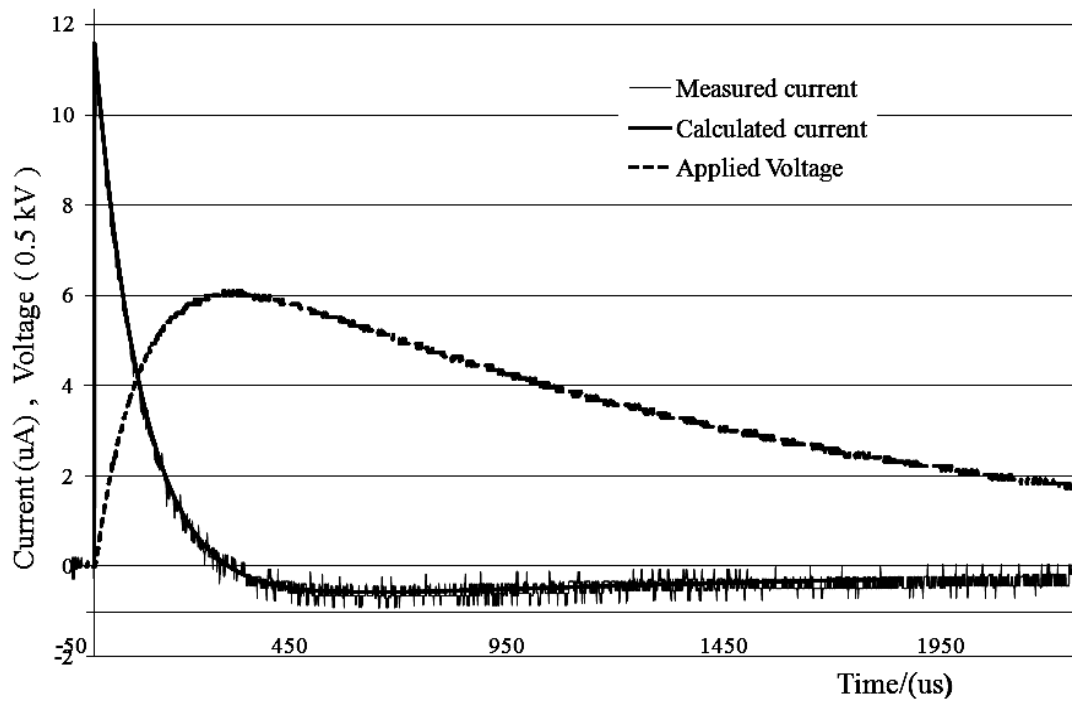


**Figure 3.3.** Measured and calculated current during application of 3 kV switching impulse and actual voltage; note that two current traces are overlapping each other.

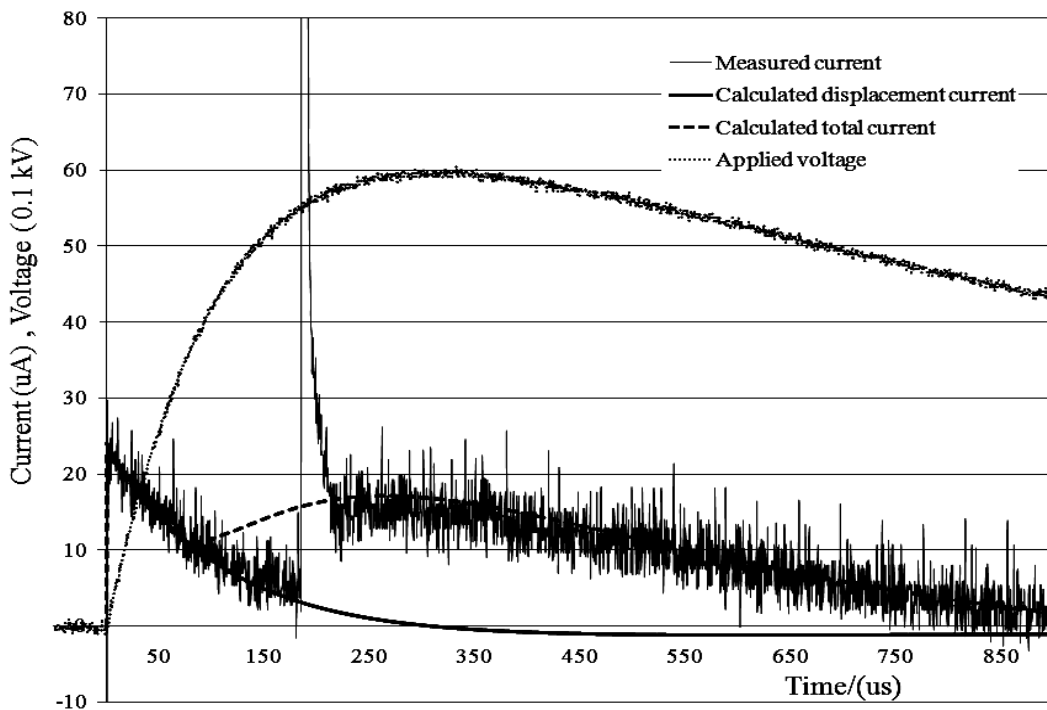


**Figure 3.4.** Measured and calculated current traces during application of 6 kV switching impulse; note that pre-onset streamer appears at 5.5 kV.

**Table 3.2.** Generated charge during discharge activity.

	Charge, nC	
	6 kV impulse	7.6 kV impulse
Measured	10.12	24.45
Calculated	8.64	22.51
Difference	1.48 (14%)	1.94 (8%)

integration of the measured and calculated currents for voltage magnitudes of 6 kV and 7.6 kV. According to the obtained results, shown in Table 3.2, contribution from the streamer current peak to the total generated charge is minor (less than 14%) in comparison with the contribution from the rest of the current trace. Simulations of pre-onset streamers would require introducing additional terms in Equations 3.1-3.3 to account for photo-ionization rate as it is done, e.g. in [72].

## 3.4 Corona modes in air

Characteristics of coronas under different impulse voltages were simulated by applying impulses with different magnitudes and time constants. Two different discharge modes, namely, glow corona and burst pulse corona, were identified by analyzing the space charge dynamics and calculated current. The characteristics of each corona mode are described here with the help of the results obtained for voltage impulses with the amplitude of 5 kV and durations of 350/1500  $\mu$ s and 12/50  $\mu$ s.

### 3.4.1 Glow corona

In the considered electrode system, the properties and characteristics of the corona discharge are mainly determined by the behavior of space charges in the drift region. The dominating charge carriers here have the same sign as the sign of the potential applied to the corona electrode, i.e., positive ions in the case under consideration. The corona region in the vicinity of the needle tip, where electrons and negative ions are dominating and ionization processes are concentrated, is found to be very thin. The main part of the gap contains positive space charge and, as it can be observed in Figure 3.5, the maximum concentration of the positive ions is reached at a distance of  $\sim 0.15$  mm from the anode tip. At the front of the applied 5 kV switching impulse (curves corresponding to times up to 350  $\mu$ s), the densities of positive ions are increasing along the gap while decreasing at the tail of the impulse (dotted lines corresponding to 400  $\mu$ s, 500  $\mu$ s and 600  $\mu$ s). Figure 3.6 shows the variation of the

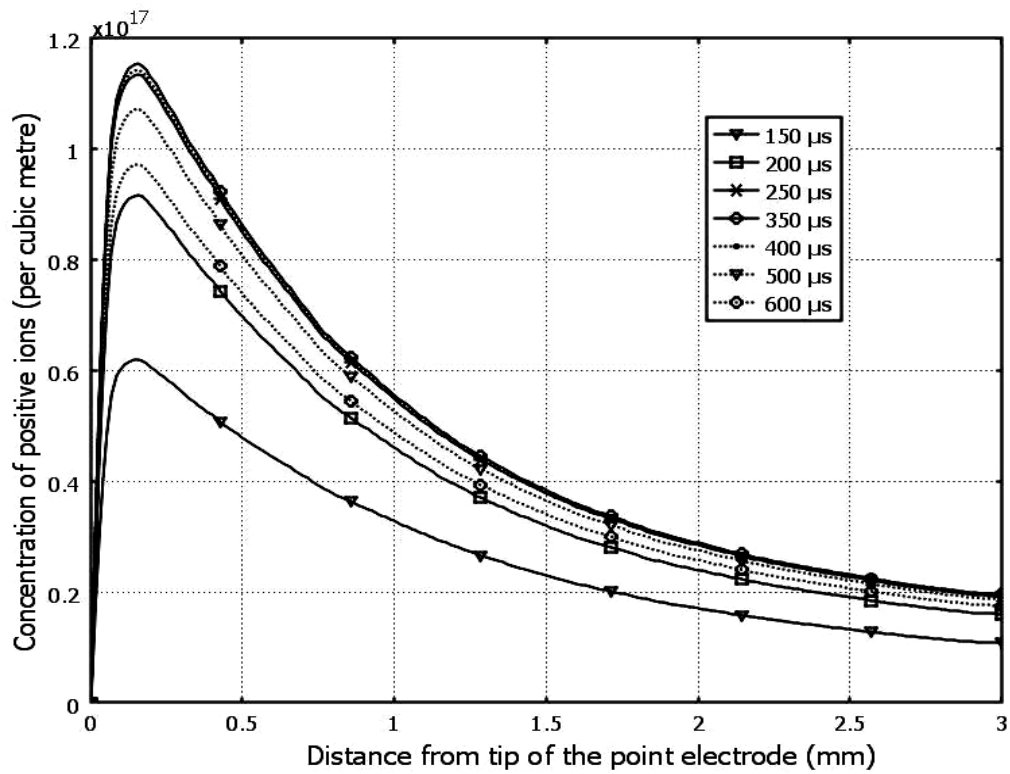


**Figure 3.5.** Calculated profiles of positive ion densities along 3 mm long air gap for 5 kV switching impulse; distance is counted from needle tip and legend shows the time instances corresponding to each of the curves.

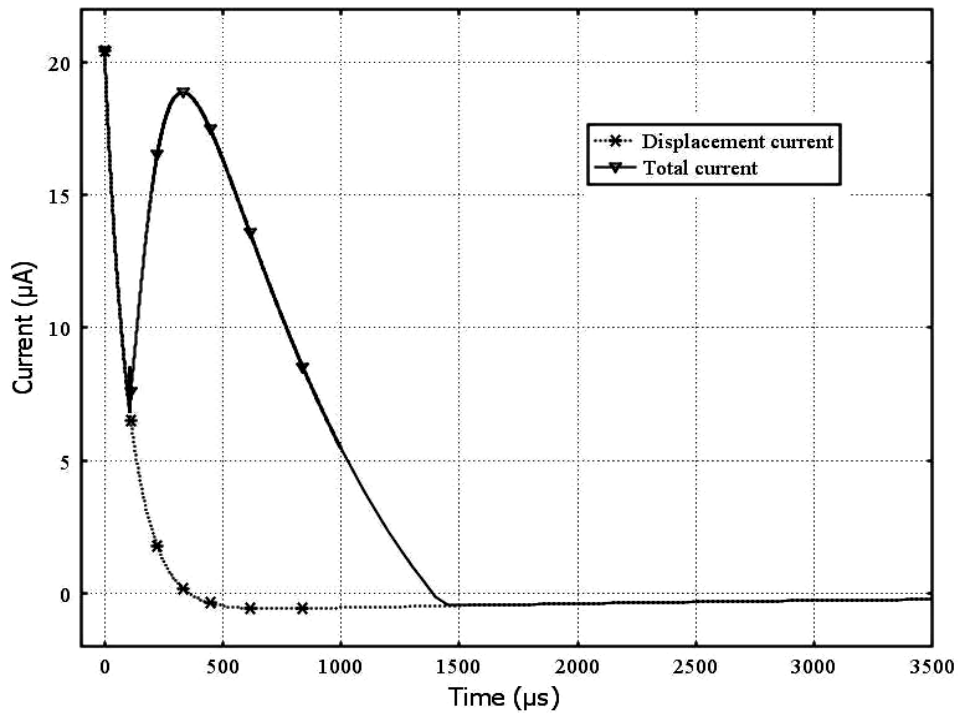


**Figure 3.6.** Calculated currents (total and displacement) for 5 kV switching impulse.

calculated total current and displacement current with time for the same applied voltage impulse. The total current contains a single smooth pulse and at instants  $t=0-100 \mu\text{s}$  and  $t > 1400 \mu\text{s}$  it is only due to the displacement (capacitive) contribution, while in the range of  $t=100-1400 \mu\text{s}$  it is caused by the conduction, which starts to be significant after the applied voltage exceeds the corona inception threshold at  $t \sim 100 \mu\text{s}$ . The current increases with the applied voltage until it reach the maximum at  $\sim 300 \mu\text{s}$ . Further, it decreases on the tail of the voltage impulse and becomes negligible when the voltage drops below the corona threshold at  $t \sim 1400 \mu\text{s}$ . Both the behavior of the density profiles of positive ions (Figure 3.5), which are concentrated in the vicinity of the anode surface, and the continuity of current flow (Figure 3.6) indicate that the type of discharge appearing at 5 kV switching impulse level correspond to a glow corona.

Time variations of the actual electric field (including the effect of space charge) and Laplacian electric field (without the effect of space charge) at the tip of the needle electrode are shown in Figure 3.7. It can be observed that during the discharge activity at  $t=100-1400 \mu\text{s}$ , the actual field strength become less than Laplacian field and remains at a fairly constant level of about 62–65 kV/cm. The reduction of the field is due to the effect of the positive charge cloud located close to the tip of the needle. At instants when no discharge activity takes place, the magnitudes of the fields are similar.

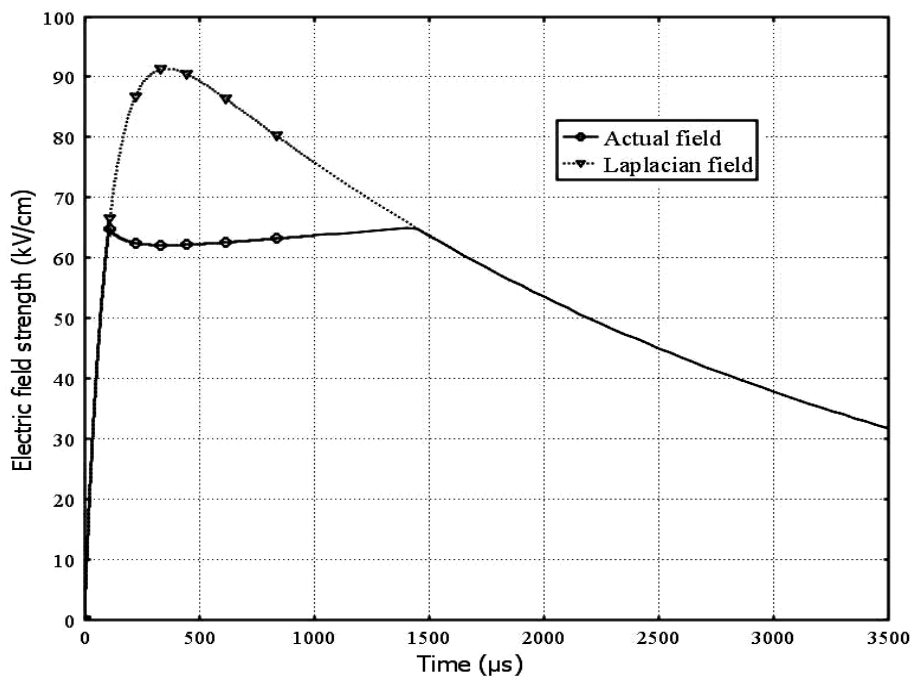


**Figure 3.7.** Calculated time variation of the actual and Laplacian electric field strength at the tip of the needle electrode for 5 kV switching impulse.

### 3.4.2 Burst corona

In contrast to the case considered above, application of a short impulse, 12/50  $\mu\text{s}$  at 5 kV, yields changes in space charge dynamics, which are affected by the increased rate of voltage rise. The distributions of the densities of positive ions along the gap for a few time instants are shown in Figure 3.8. In this case, the location of the maximum concentration of positive ions is changing within short time, indicating that the charge cloud is moving from the needle tip into the bulk of the gap. Note that the maximum concentration is higher than that for the case of switching impulse and the peak density of ions decreases during its movement from the needle tip. Such behavior is typical for so-called burst corona [19] which is conditioned by a series of consecutive positive charge clouds moving along the discharge gap from the anode to the cathode. Figure 3.9 demonstrates formation and propagation of the positive charge cloud during a single burst pulse. The charge is formed very close to the anode and becomes denser during a short time interval (frames for  $t = 12.03 \mu\text{s}$  and  $12.05 \mu\text{s}$ ). Further it starts moving towards the cathode, entering a region with lower field intensity where ion density decreases very quickly (frames for  $t = 12.09\text{--}12.30 \mu\text{s}$ ). After some delay, formation of a new burst starts.

The burst pulses appear due to high density of the generated space charge which produces its own field directed opposite to the Laplacian field. This yields reduction of the electric field strength at the surface of the corona electrode, as shown in Figure 3.10, and a corresponding decrease of the ionization intensity. When the space charge moves away from the anode and its density decreases, the field between the cloud and the anode recovers and provides necessary conditions for formation of the next pulse. This repetitive process results in a series of charge clouds moving along the discharge gap and produces pulsating current in the external circuit, Figure 3.11, instead of the smooth conduction current observed in the case of switching impulse.

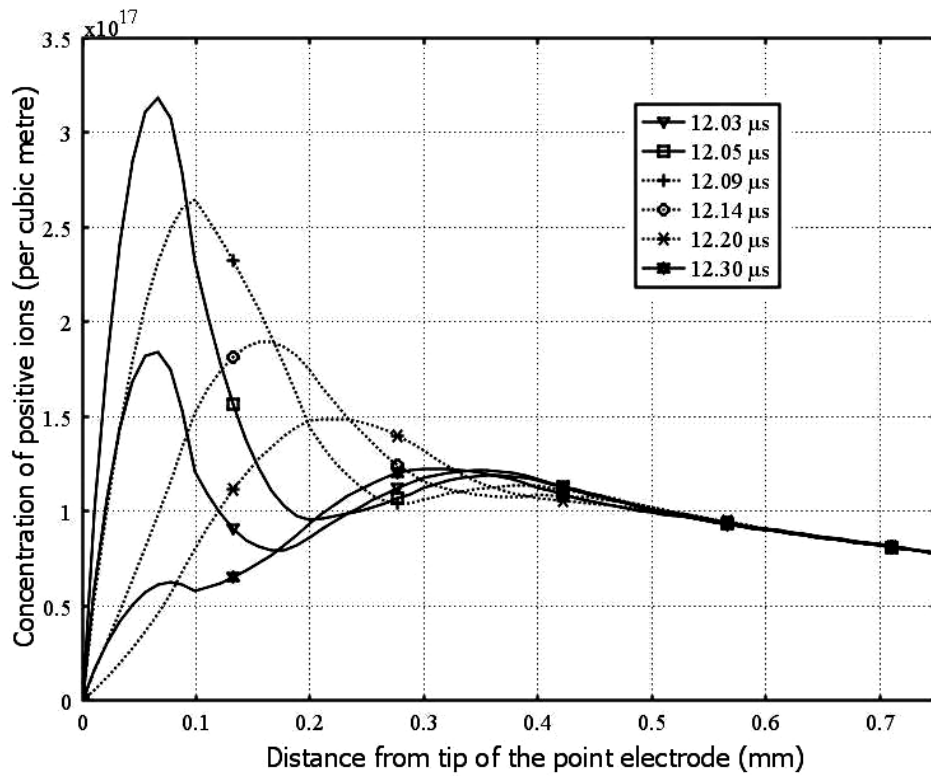


Figure 3.8. Calculated profiles of positive ion densities along the gap for 5 kV short impulse.

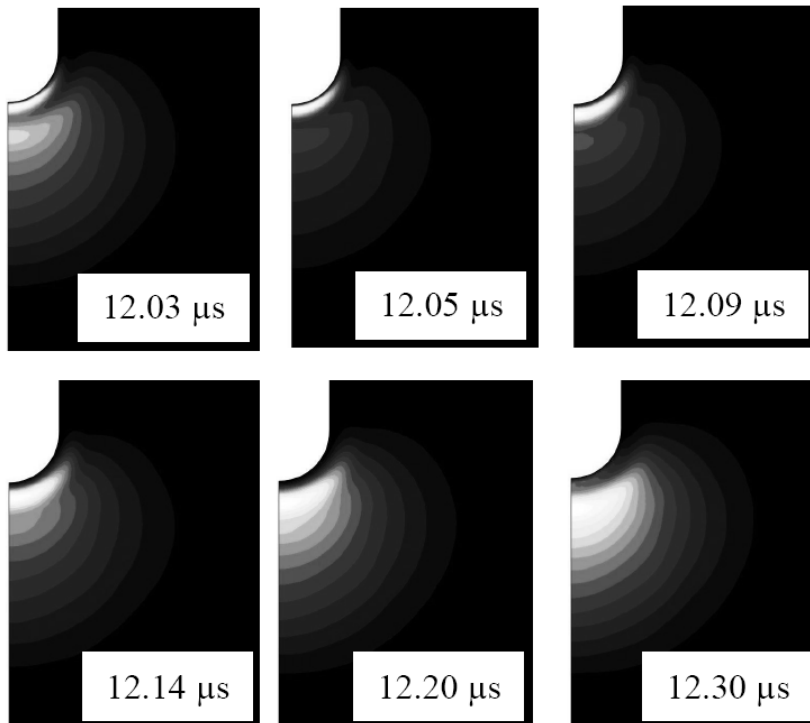
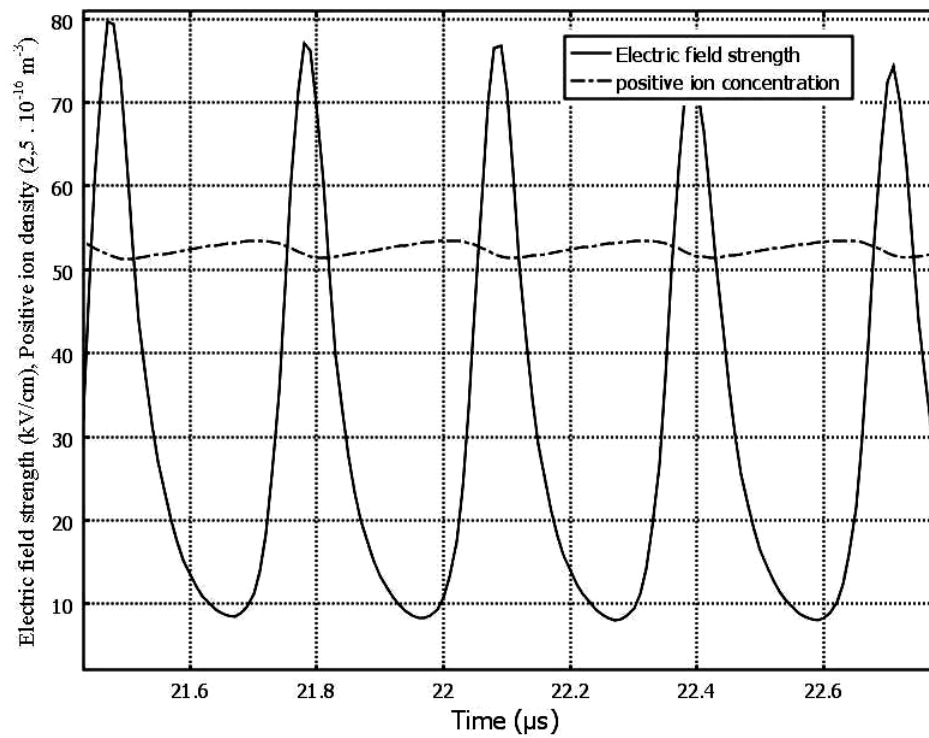
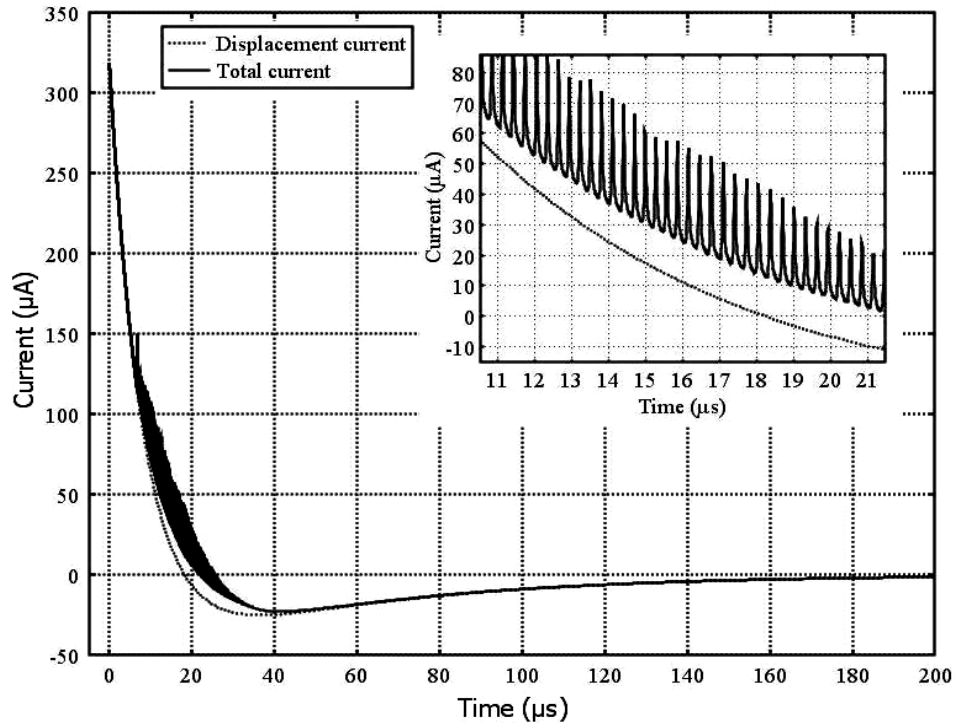


Figure 3.9. Positive ion concentrations during development of a burst pulse; normalized (actual/maximum) densities are shown, where lighter areas correspond to higher and darker areas to lower concentrations.



**Figure 3.10.** Variation of calculated electric field and positive ion density with time at a point very close to the tip of the needle electrode.



**Figure 3.11.** Time variation of the calculated current for 5 kV short impulse; during corona discharge burst current pulses are superimposed on displacement current; the enlargement window shows the pulsating behavior of the current.

## 3.5 Surface charging by impulse corona

For simulating surface charging of a polymeric material by positive impulse corona, a 2 mm thick material sample with the relative permittivity of 2.3 is placed on the grounded plane electrode against the positive needle, similarly to the experiments presented in [14, 94]. To start with, the solid material is assumed to be an ideal insulator with the conductivity equal to zero. Thus, the fluxes of charge carriers are set to zero inside the solid layer and they are not allowed to penetrate (to be injected) into the material or be ejected from its surface. Charging characteristics corresponding to both corona modes, burst pulses and glow, were analyzed by means of the simulations.

### 3.5.1 Charging by glow corona

The voltage level of 6 kV was selected to be able to compare the simulation results with available experimental data [57]. The results obtained from the simulations yield the following physical picture of the corona charging of solid material surface. Immediately after voltage application, the charge carriers present in air start drifting along the direction of the applied field (or opposite, depending of the sign of the charge). As Figure 3.12 shows, the field strength increases in the vicinity of the needle electrode due to rising voltage and it reaches the corona inception threshold at about 60  $\mu\text{s}$  after application of the impulse. It can be observed that the discharge exists until  $\sim 1500 \mu\text{s}$  and it has features of glow corona (compare Figures 3.12 with 3.7).

The changes of the positive ion concentration along the gap are shown in Figure 3.13. As one can notice, at  $t = 60 \mu\text{s}$ , when the corona is weak, the ion concentration is just slightly above the background level of  $\sim 10^8 \text{ m}^{-3}$ . However, already at this instance higher ion densities appear at the tip of the needle and on the gas-solid interface as a result of ionization and ionic drift under applied electric field. At  $t > 62 \mu\text{s}$ , the charge concentration close to the needle tip increases rapidly due to ionization. For the instants of 100  $\mu\text{s}$  and 300  $\mu\text{s}$ , still corresponding to the front of the impulse, ion densities become very high along the whole gap (note that their magnitudes are about seven orders higher than those at 60  $\mu\text{s}$ ). This is the result of the intensive ionization taking place in the corona region that supplies positive charges drifting towards solid material surface and accumulating there. At  $t = 1000 \mu\text{s}$  (the tail of the impulse), a decrease of the concentration can be observed due to reduced ionization intensity, following the reduction of the applied field. Further at  $t = 1500 \mu\text{s}$ , when corona activity stops, charge concentration closer to the needle electrode decreases rapidly. At the same time, the density of charges at the solid material surface is still high as the deposited charges during corona remain there. At  $t = 2500 \mu\text{s}$ , the density of ions closer to the corona electrode is reduced even more, whereas it slightly increases at sample surface. This can be explained by a sweep-out of the charges remaining in the gap under the weak applied external field.

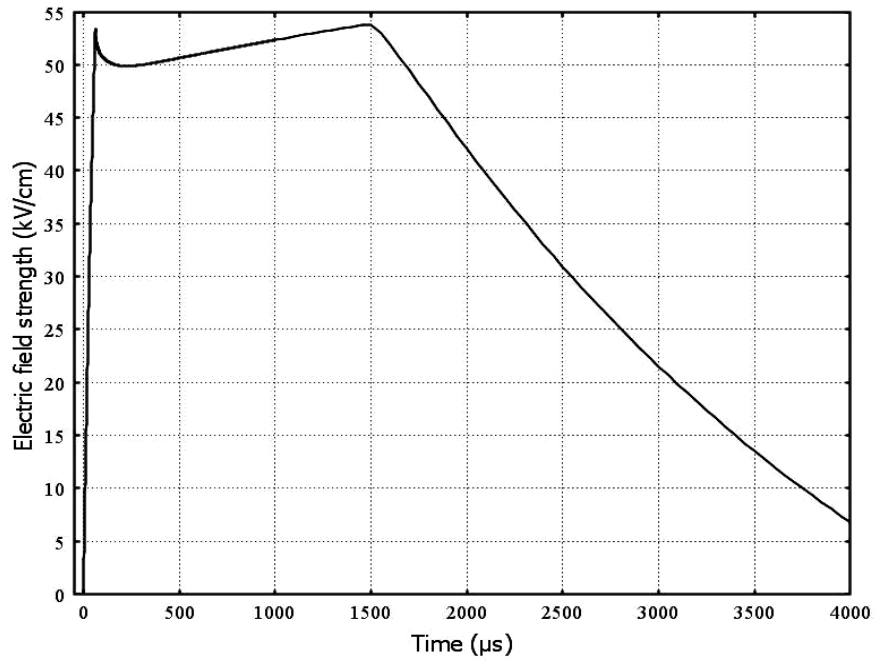


**Figure 3.12.** Calculated electric field strength at the tip of the point electrode for 6 kV switching impulse with solid insulating material placed on grounded electrode.

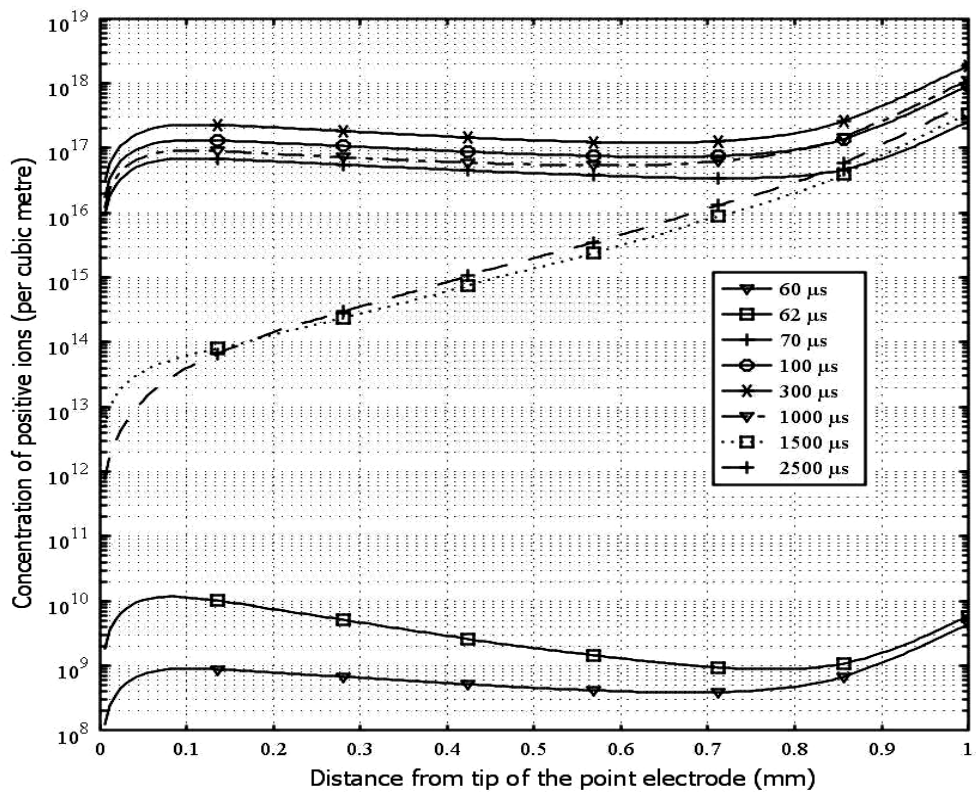


**Figure 3.13.** Calculated profiles of positive ion densities along the gap for 6 kV switching impulse; respective time instants are indicated in the legend window, while the distance of 1 mm corresponds to the position of gas-solid interface.

The development of the charge concentration along the surface of the dielectric material is shown in Figure 3.14. It can be observed that the charge density directly under the needle electrode becomes high right after the corona inception (compare curves for  $t = 70 \mu\text{s}$  and  $60 \mu\text{s}$ ). Following radial expansion of the charged spot along the material surface takes place during the whole corona discharge process. The rate of the radial expansion is highest,  $\sim 70 \text{ m/s}$ , immediately after the inception and it decreases gradually with time down to  $\sim 10 \text{ m/s}$  and less at the longer instants (see e.g. profiles for  $t = 570$  and  $670 \mu\text{s}$ ). At  $t = 1500 \mu\text{s}$ , when the corona activity vanishes, the radius of the charged spot on the surface is fairly constant and reaches  $\sim 2 \text{ cm}$ . Similar dimensions of the charged regions on polymeric surfaces due to point corona charging have been measured in [57, 94]. At longer times, the density of charges on the gas-solid interface changes insignificantly. In reality, several relaxation processes (charge leakage through the bulk, gas neutralization, etc.) take place and alter the surface charge concentrations. These are further considered in Chapter 4 below.

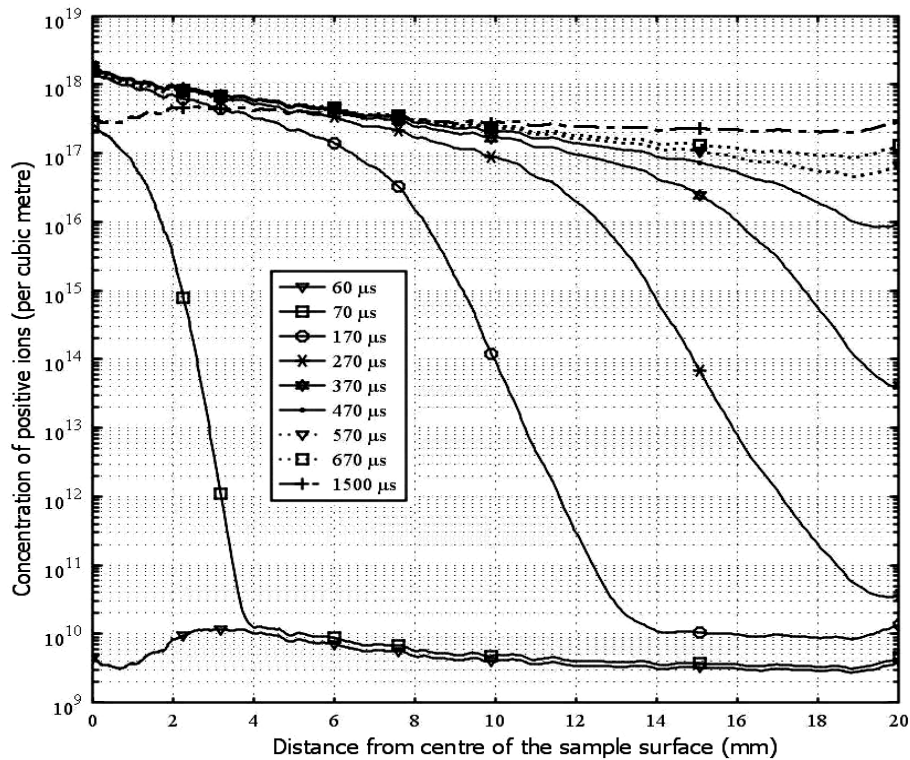


Figure 3.14. Calculated profiles of positive ion densities along the sample surface during charging by glow corona.

### 3.5.2 Charging by burst corona

This section describes the charging process corresponding to application of 6 kV short impulse, 12/50  $\mu\text{s}$ . For this case, the electric field strength in the vicinity of the needle tip reaches the corona inception threshold at  $\sim 4 \mu\text{s}$  after the impulse application, Figure 3.15. Oscillating field behavior observed at the beginning of corona activity indicates that the burst mode is taking place at this stage. At  $\sim 30 \mu\text{s}$  (on the tail of the applied impulse), burst character of corona changes to a glow regime until corona activity completely stops at  $\sim 43 \mu\text{s}$ . As the dynamics of glow corona charging is discussed in the previous section, we focus here on material surface charging by the burst corona pulse (i.e., on time instants from  $\sim 4 \mu\text{s}$  to  $30 \mu\text{s}$ ).

Figure 3.16 shows time variations of positive ion densities during a single burst pulse. The high concentration appearing close to the anode at  $t = 5.45 \mu\text{s}$  indicates that a new burst starts from the needle electrode. It can be also observed that deposited charges from the previous burst remain at the gas-solid interface. Newly created burst moves along the gap away from the anode (frames for  $t = 5.48\text{-}5.54 \mu\text{s}$ ) and at  $t = 5.54 \mu\text{s}$  it reaches the sample surface. Positive charges brought to the gas-solid interface with the burst contribute to the pre-deposited surface charge and increase its density (note the light color layer on the sample at  $t = 5.62 \mu\text{s}$ ). At the same time, conditions for formation of the next burst are created and it appears at  $t = 5.68 \mu\text{s}$ , similarly to the one initiated at  $5.45 \mu\text{s}$  (compare the first and the last frames in Figure 3.16). One should also notice that the new burst sees more pre-deposited charges on the solid surface.

Time variations of the density profiles of the deposited positive charges along the sample surface are illustrated in Figure 3.17. Before the discharge starts, almost constant initial charge concentration can be observed (background density of charge carriers) and it is slightly increased under the needle tip due to the enhanced field and stronger drift (profiles for  $t = 3 \mu\text{s}$  and  $4 \mu\text{s}$ ). Thereafter, when the burst started at  $\sim 4 \mu\text{s}$  the concentration at the location directly under the needle becomes higher (see profile for  $t = 4.5 \mu\text{s}$ ). During the burst corona, the charge densities on the surface increase and the charged spot expands along the sample surface with high velocity of  $\sim 10^3 \text{ m/s}$  (see profiles for  $5 \mu\text{s}$ ,  $6 \mu\text{s}$ ,  $10 \mu\text{s}$  and  $20 \mu\text{s}$ ). Once the concentration under the needle tip exceeds  $\sim 10^{18} \text{ m}^{-3}$ , contributions of new bursts to the total surface charge at the centre of the sample become negligible (compare profiles for  $20 \mu\text{s}$  and  $30 \mu\text{s}$ ). However, the radial expansion still takes place although with the velocity lower than that at the beginning of the burst corona. After transformation of the burst mode into the glow regime at  $\sim 30 \mu\text{s}$ , the charged spot still expands along the solid surface with the velocity of  $\sim 40 \text{ m/s}$  and this is associated with the slight decrease of ion concentrations at the centre. After  $100 \mu\text{s}$  (far away on the tail of the applied voltage impulse), the radius of the charge spot reaches  $\sim 14 \text{ mm}$  and it is smaller than that in the case of charging by glow corona only.

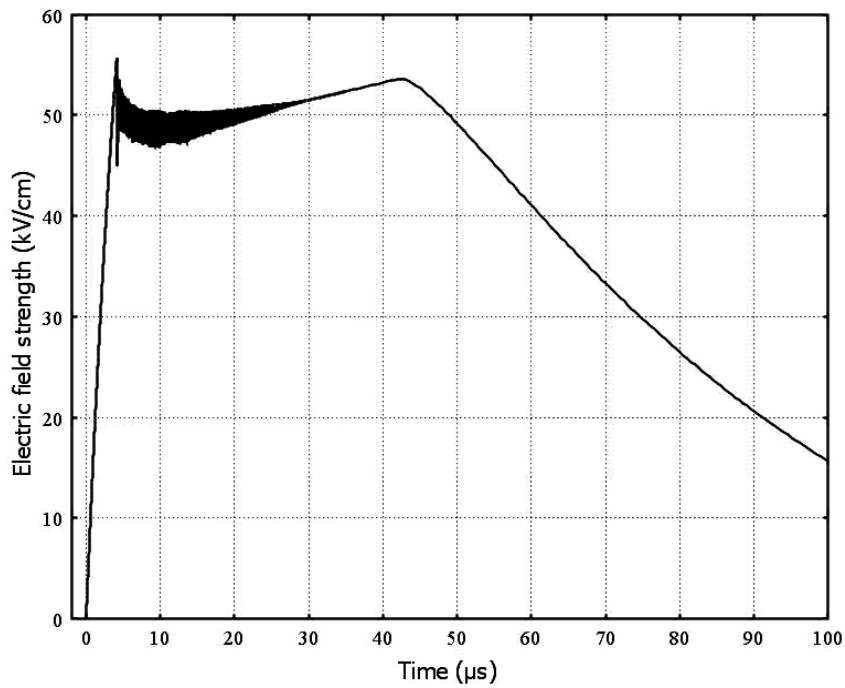


Figure 3.15. Calculated electric field strength at the needle tip for 6 kV short impulse.

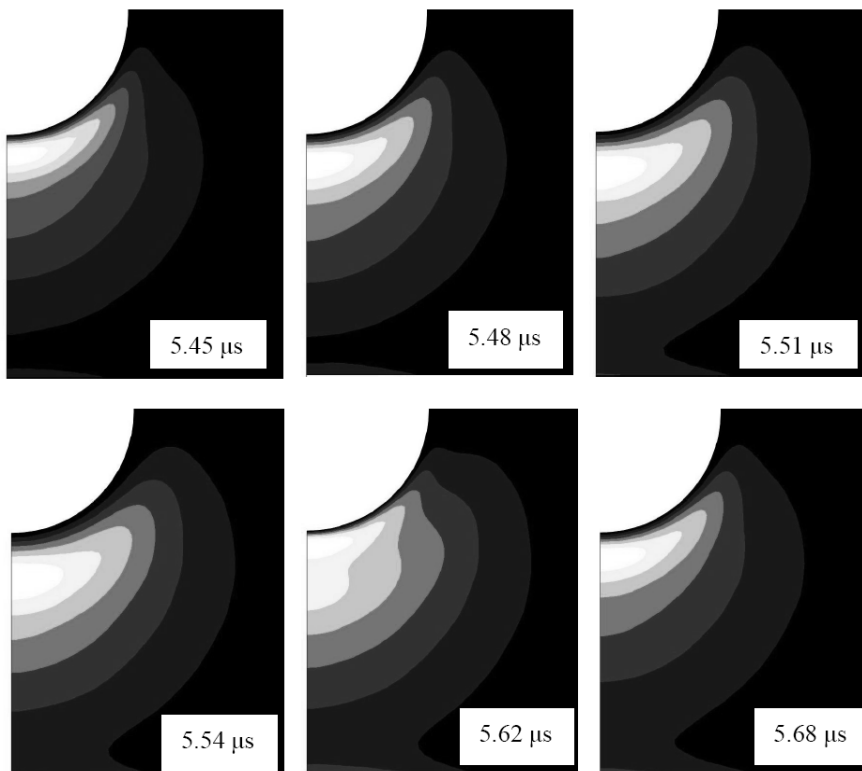


Figure 3.16. Charge deposition during a burst pulse; normalized (actual/maximum) densities are shown, where lighter areas correspond to higher and darker areas to lower concentrations.

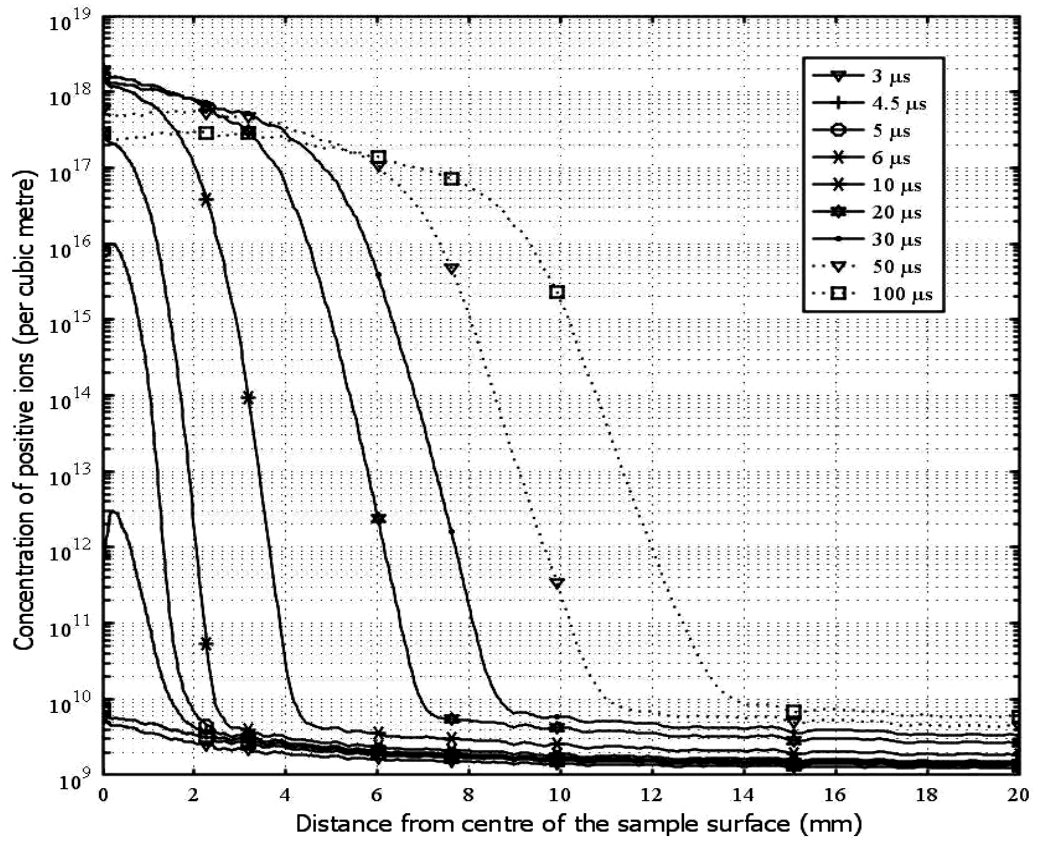


Figure 3.17. Calculated profiles of positive ion densities along gas-solid interface for 6 kV short impulse.



## 4 Surface charging and charge decay on HTV silicone rubber

This chapter focuses on identification of surface charging and charge decay mechanisms on corona charged thick polymeric material samples in air. Surface potential resulting from impulse corona charging was measured on 2 mm thick samples of high temperature vulcanized (HTV) silicone rubber. Firstly, charge decay due to bulk neutralization was studied by preventing other charge decay mechanisms. Then, the effect of gas neutralization on charge decay was investigated by performing experiments under two different conditions, i.e. gas neutralization under natural background ionization and gas neutralization under artificially enhanced concentrations of free ions. Finally, a contribution of surface conduction to charge decay was studied by performing measurements on corona aged samples. The decay characteristics were further utilized to deduce decay rates as well as materials properties, such as field dependent apparent bulk conductivity and trap density distributions.

### 4.1 Experiments

#### 4.1.1 Experimental setup

The performed experiments aimed at obtaining charge distribution and charge decay characteristics by measuring the surface potential at several selected points on sample's surface. As shown in Figure 4.1, the sample (100 mm×100 mm×2 mm) was placed on a grounded copper plate while its upper surface was open to the surrounding air. Corona charging of the sample was achieved by using a needle (0.95 mm diameter) mounted on a movable arm and kept 1 mm above the center of the sample surface. Lightning (standard, 1.2/50  $\mu$ s) or switching (350/1500  $\mu$ s) impulses with peak magnitudes of  $\pm 8$  kV or  $\pm 11$  kV were applied between the needle and the counter-electrode from an impulse generator (Haefely PU 12) and were recorded using in-built low voltage output signal meter. The resulting charging currents were measured using a current monitor (Pearsson coil) mounted on the cable connecting the impulse generator and the needle. For measuring surface potential, Kelvin type electrostatic

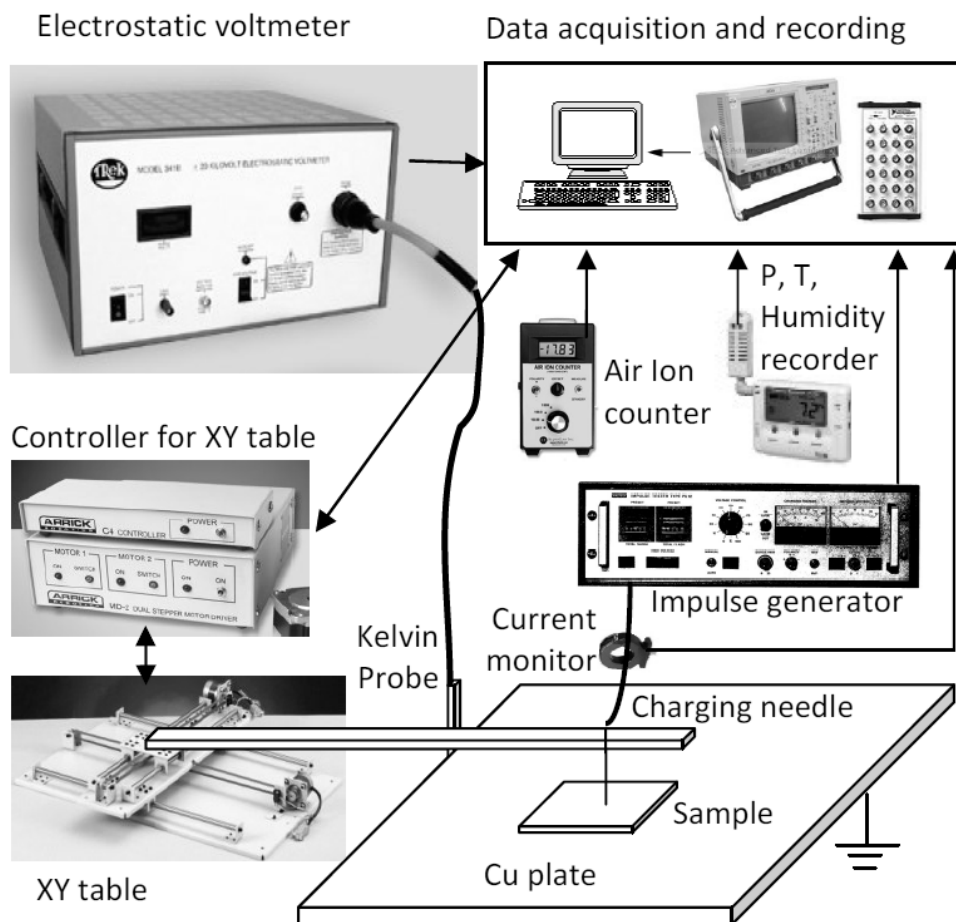


**Figure 4.1.** Schematic diagram of the experimental setup.

probe (Trek 3455 ET) connected to an electrostatic voltmeter (Trek 341B) was used. The potential probe was mounted on the same arm as the charging needle. The probe-to-surface distance was maintained at 3 mm, while positioning of the probe and the needle was achieved by means of a computer controlled XY table (Arrick Robotics XY30). An air ion counter (Alpha Lab Inc.) was used to measure the ion concentrations in air. Temperature, pressure and humidity recorder (TR-73U) was also mounted close to the experimental set-up and recorded ambient conditions throughout the decay measurements. An oscilloscope (Lecroy LC-574AM) and a computer equipped with a data acquisition card were used to collect and to record the experimental data which included charging voltage, charging current, probe position indicator from XY table, surface potential and concentration of air ions.

### 4.1.2 Experimental procedure

Before charging, the material samples were cleaned with isopropanol and thereafter dried. After that, an initial scan of the surface potential was performed to make sure that the sample was properly neutralized. Further, the needle was brought above the centre of the sample and a charging impulse was applied. Immediately after the

charging was completed, the arm was moved away and the potential probe came to the same location. As preliminary measurements showed, the charged spot formed on the surface was symmetrical and, therefore, the scanning along a single radial line was sufficient. The scanning always started at 1 minute after the charging and included 15 measuring points along 3 cm distance, which took about 15 s. However in case of studies with corona treated samples, the first scan was performed at 20 s after the charging and the scanning span was extended up to the edge of the sample surface, i.e., up to 5 cm. Once the scan was completed, the probe was moved to the centre or away from the sample, depending on the required test conditions (see Section 4.1.4 below). Subsequent scans were performed at time intervals selected for each test case. In some cases, extra measurements were taken at the centre of the sample only, without scanning the surface.

### 4.1.3 Material types

The materials used in this study were two types of high temperature vulcanized silicone rubbers. The first type of material, commercially referred as Elastosil R401/60, was based on polydimethylsiloxane (PDMS) and reinforcing silica filler. It was cross-linked with 0.7 wt. % dicumylperoxide (dispersed in 0.7 wt. silicone oil) at 165 °C/100 bar /15 min and then postcured at 170 °C/4 h in an oven. The second material, referred as Powersil 310, was also based on PDMS and silica filler, but in this case PDMS was also filled with aluminatrichydrate (ATH). These samples were compression molded at 165 °C /15 min and then postcured at 150 °C/4 h. The electrical properties of both the materials, obtained by standard resistivity and dielectric response measurements, are summarized in Table 4.1. In addition to these two materials, non-postcured Elastosil samples aged by corona treatment were used for some studies and corresponding parameters are presented in Section 4.4 together with relevant results. As one can observe in Table 4.1, Elastosil is highly resistive as compared to Powersil and it is characterized by lower dielectric constant. One should note here that for the flat samples surface potential is proportional to the charge density and inversely proportional to the material permittivity, as discussed in Chapter 2 (see Equation 2.1). Hence, the conversion of the measured potentials to surface charge densities is rather straightforward.

**Table 4.1.** Electrical properties of the studied materials

Material	Elastosil	Powersil
Relative permittivity @ 100 Hz	2.7	3.7
Bulk conductivity*, ( $\Omega\text{m}$ ) <sup>-1</sup>	6·10 <sup>-16</sup>	3.5·10 <sup>-15</sup>
Surface conductivity*, ( $\Omega\text{.sq}$ ) <sup>-1</sup>	1·10 <sup>-16</sup>	3.3·10 <sup>-14</sup>

\* -measured according to ASTM Standard D 257.

#### 4.1.4 Test conditions

The three types of external conditions for the decay of surface charges were implemented in the experiments as follows:

- (i) **Zero gas neutralization** - this was achieved by continuously keeping the probe close to the surface at the centre of the sample during time intervals between the scans. As the body of the probe has the same potential as a portion of the surface where the potential is measured, the electric field in the air gap between the probe and the surface is zero (see Section 2.2.2). Therefore, air ions are not attracted to the surface under the probe and gas neutralization of the surface charge is prevented. Moreover, due to relatively low radius of the charged spot (about 2 cm) as compared to the probe dimensions (1 cm×1 cm×10 cm), it is reasonable to assume that keeping the probe above the location where the charging corona needle was placed, prevents the gas neutralization on the most of the charged area.
- (ii) **Natural gas neutralization** – takes place due to interaction of surface charges with free ions (positive and negative) present in air produced by background ionization processes. This condition is achieved by keeping the probe far away from the charged sample. However during the scanning, the probe comes close to the sample surface and alters conditions for charge decay. This effect was minimized by limiting the scanning time to 15 s and by selecting sufficiently long intervals between scans. The shortest scanning interval used in this case was 3 minutes.
- (iii) **Enhanced gas neutralization** - in this case the scanning arrangement was as in case (ii). However, the concentration of free ions in air having the polarity opposite to that of the deposited charges was increased by means of a dc corona source located in the vicinity of the measurement setup. The voltage applied to the corona source was +10 kV in case of negatively charged sample surfaces and – 9.6 kV for positively charged surfaces, both providing the concentrations of free ions in the surrounding air at ~15000 ions/cm<sup>3</sup>. This concentration is ten times higher as compared to the one measured under natural conditions.

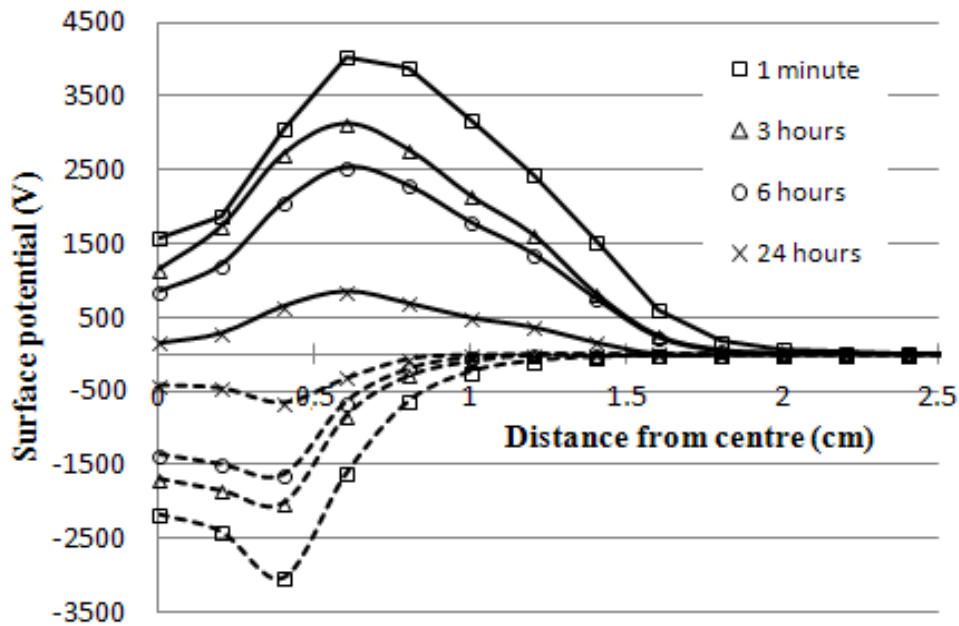
## 4.2 Decay due to bulk neutralization

Charge decay on non-aged material samples due to only bulk neutralization was realized by implementing the condition for zero gas neutralization as described above. Moreover, since no lateral expansions of the charge spot were observed, it was possible to exclude surface conduction from the analysis. Therefore, the surface potential decay under this condition was considered as solely caused by bulk neutralization. Reproducibility of the results was checked by conducting the same measurements up to six times and good repeatability was observed. Therefore, the results from a single

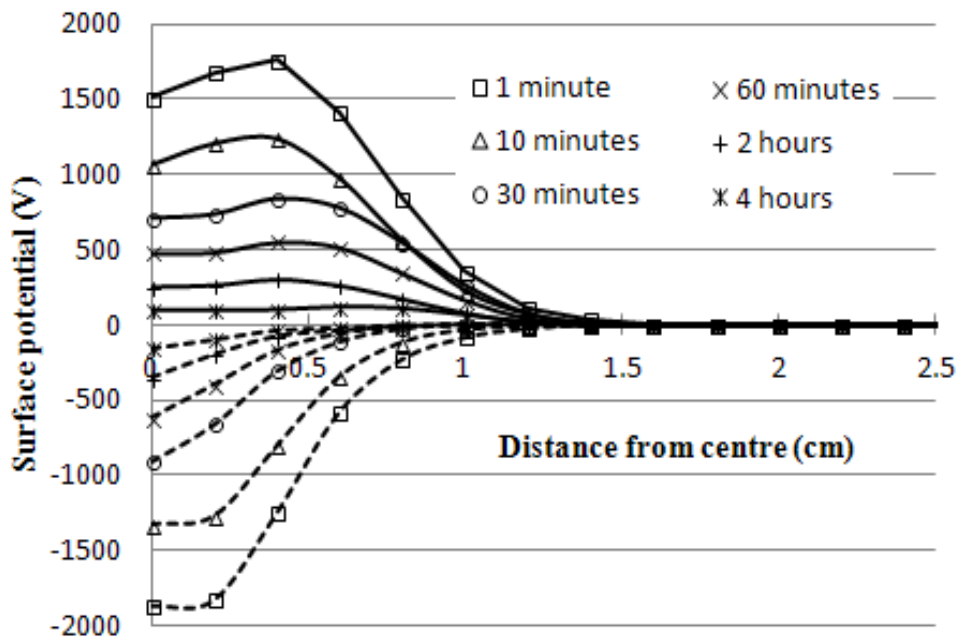
typical trial are presented here. However one should also mention that it was not possible to reproduce exactly the charging process due to the statistical nature of the impulse corona. This resulted in a slight variation in the magnitude and shape of the potential distributions. Therefore, the decay characteristics presented below are normalized in some of the cases. All the measurements were performed under ambient conditions which were recorded throughout the measurement sessions. The temperature, pressure and relative humidity were respectively within the ranges of 20-22 °C, 980-1020 hPa and 50-60%. Even though the atmospheric conditions varied from one measurement to another, no significant effect on decay characteristics were found.

### 4.2.1 Potential distribution on the surface

Typical surface potential distributions measured at different time instants during the decay are shown in Figure 4.2. These results were obtained by charging the samples with standard lightning impulse voltages (1.2/50  $\mu$ s) with peak magnitudes of  $\pm 8$  kV. Important parameters characterizing the surface charges and their distributions at 1 min after charging are summarized in Table 4.2. One can observe that the initial (1 min after the charging) surface potential distributions have either saddle-like or bell-like shapes. Saddle-like shape can be attributed to the appearance of back discharges between the charged surface and the needle electrode when the electric field of the deposited charge is strong enough for initiating corona at the tail of the applied impulse or after it (detail analysis on back discharge is presented in Chapter 5 for cylindrical insulator model). Evaluation of the total charge on the surface was done by, firstly, calculating the charge density distributions from the measured potential distributions using Equation 2.1 and then by integrating it over the surface. Note that when using Equation 2.1 for charge calculations, two assumptions were made: (a) the permittivity of the material remains constant and time independent, and (b) if charge injection takes place, the distance these charges penetrate into the bulk within 1 min is negligible as compared to the sample thickness and, hence, the space charge effects can be neglected. The first assumption is based on the results of the measurements where the permittivity was found to be constant over the frequency range  $10^{-2}$ - $10^3$  Hz. The second assumption is based on low bulk mobility of charges in this type of polymeric materials. As an example, the mobility in polyethylene is in the order of  $10^{-15}$  m<sup>2</sup>/Vs [34]. As one may note from the figures, the application of positive impulses resulted in a higher amount of charge on the surface and its wider spread than the ones obtained for negative charging for both the studied materials. This observation agrees well with the results presented in [14]. It can also be seen that a considerable amount of charges remained on the surface of Elastosil sample even 24 h after charging while for Powersil most of the charges decayed already after 4 h. A comparison of the potential distribution curves for different time instants shows that the potential decay is faster



Elastosil



Powersil 310

**Figure 4.2.** Measured surface potential distributions along a radial line; legend shows the time elapsed after corona charging by positive (solid lines) and negative (broken lines) voltage impulses.

**Table 4.2.** Comparison of the parameters related to charging process.

Parameter	Elastosil		Powersil	
	Positive	Negative	Positive	Negative
Radius of the charged spot, cm	2	1.4	1.4	1.2
Maximum charge density, $\mu\text{C}/\text{m}^2$	48	36	29	30
Total charge 1 min after charging, nC	25.4	5.5	6.4	3.2
Shape of distribution	saddle	saddle	saddle	bell

for the regions where the potential is higher. This indicates that the decay process is field dependent and needs to be analyzed with respect to absolute potential. Further analysis of the decay characteristics is performed based on the potential decay at the centre of the sample.

#### 4.2.2 Potential decay at the sample centre

Figure 4.3 shows the variation of the surface potential with time. The dependencies are normalized in respect to the initial potentials  $V_0$  for each of the presented cases. As it can be observed, only very small differences appear in the characteristics for both polarities of the charging corona. At the same time, the most pronounced feature is that the decay is much faster on Powersil sample as compared to Elastosil. Thus, it takes about 25,000 s for the potential to drop to 50% of the initial value in case of Elastosil whereas this time is only  $\sim 1500$  s for Powersil, i.e. the decay is  $\sim 16$  times faster in the latter case. The times needed for surface potential to decay down to 10% are respectively  $\sim 87,000$  s and  $\sim 10,000$  s for Elastosil and Powersil, indicating less pronounced differences at lower potentials levels.

#### 4.2.3 Decay rates and field dependent apparent bulk conductivities

Figure 4.4 presents the variations of the decay rate with the magnitude of the surface potential. The decay rate,  $dV/dt$ , was calculated by applying the central difference formula to the potential decay data measured at the centre of the sample. As one can see, the decay rates increase with increasing surface potential magnitudes. At potential values higher than  $\sim 500$  V (corresponding averaged field in the sample is 2.5 kV/cm),

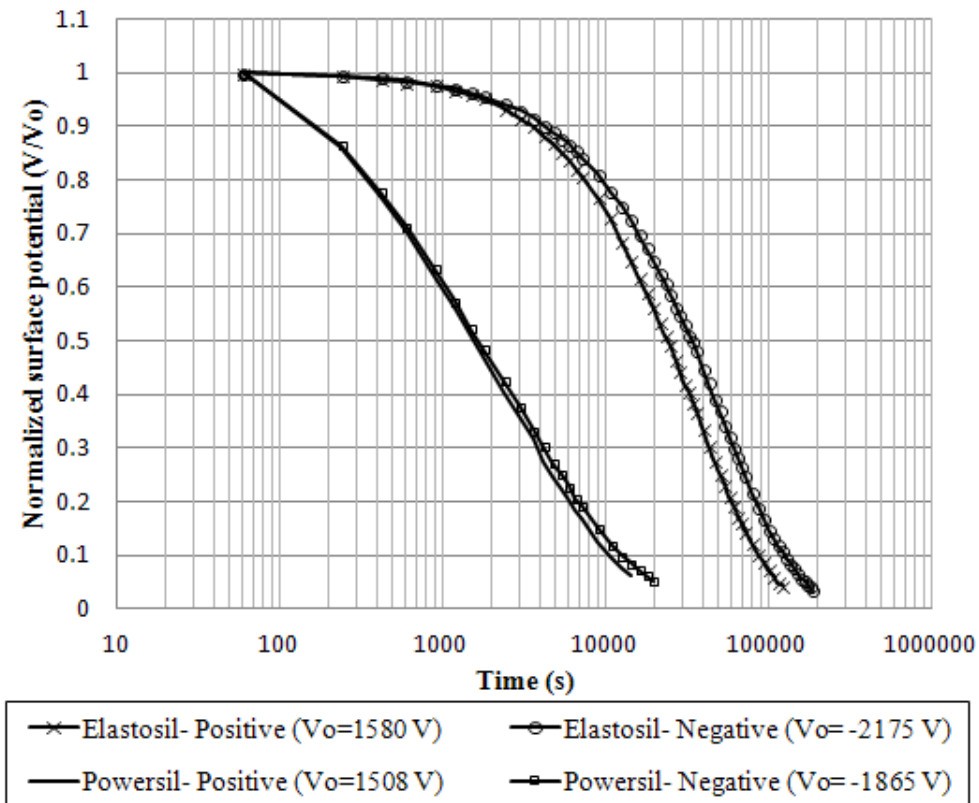


Figure 4.3. Decay of the normalized potential at the centre of the samples for zero gas neutralization; the legend shows absolute value of the initial potentials.

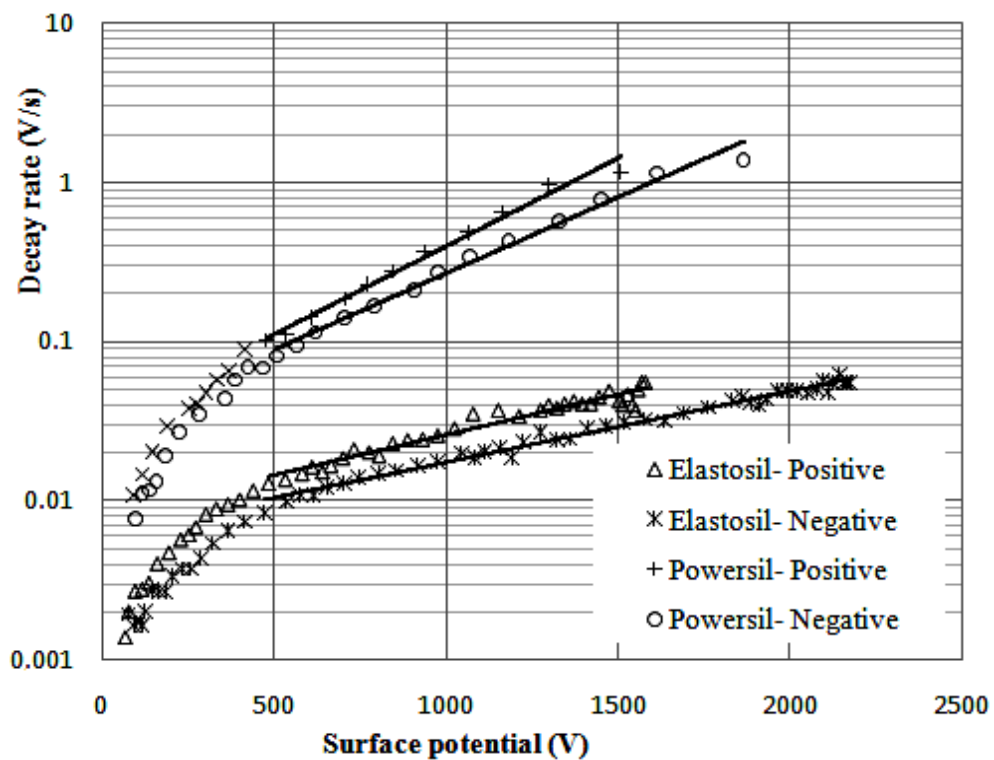
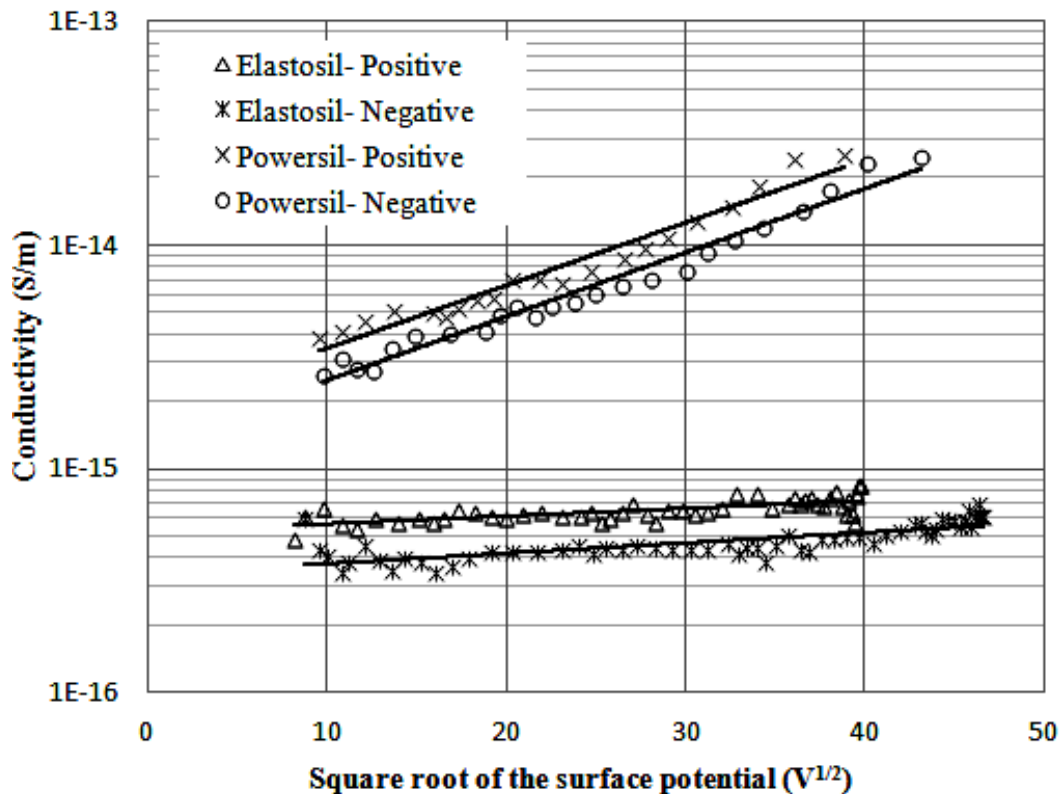


Figure 4.4. Variation of the calculated decay rate with potential magnitude. Solid lines are the results of curve fitting.

the decay rate varies exponentially with its magnitude. Also the differences between the decay rates of the different materials are significant: the decay is faster for Powersil than for Elastosil samples ( $\sim 10$  times at 500 V, and  $\sim 20$  times at 1500 V). Slightly higher decay rate for the positive charging may be related to the differences in the initial distributions.

As mentioned earlier, the charge decay at zero gas neutralization and negligible surface leakage is believed to be purely due to bulk neutralization, which is the net effect of intrinsic conduction, charge injection and dipolar polarization. However, as evaluating the contributions from each of the mechanisms is rather complicated [40], in this study the net effect of all three is treated as an intrinsic conduction process and is quantified as “apparent bulk conductivity”. With this approach, the measured decay characteristics can be used for estimating the apparent bulk conductivity  $\sigma$  of the materials, according to Equation 2.4. This conductivity can be further represented in terms of Poole-Frenkel model described in Section 2.2.4. The values of the calculated conductivity are shown in Figure 4.5 as a dependence on  $\sqrt{V}$ . The parameters extracted from the experimental results are summarized in Table 4.3, where the conductivity values measured using standard tests procedure at 400 V (Table 4.1) are also provided for easy comparisons. For all the cases, the dependencies seems obeying the Poole-Frenkel model. However, one may notice that in case of Elastosil, the conductivity is almost constant and the coefficient  $\beta$  is very small as compared to its theoretical value.



**Figure 4.5.** Calculated voltage dependent apparent bulk conductivities; Solid lines represent exponential fittings for each case.

**Table 4.3.** Conductivities of the studied materials.

Parameter	Elastosil		Powersil	
	Positive	Negative	Positive	Negative
Zero-field conductivity in eq. (2.5) $\sigma_0$ , S/m	$5 \cdot 10^{-16}$	$3 \cdot 10^{-16}$	$2 \cdot 10^{-15}$	$1 \cdot 10^{-15}$
Conductivity at 400 V, S/m	$6 \cdot 10^{-16}$	$4 \cdot 10^{-16}$	$6 \cdot 10^{-15}$	$5 \cdot 10^{-15}$
Conductivity from standard tests, S/m	$6 \cdot 10^{-16}$		$3.5 \cdot 10^{-15}$	
Experimental $\beta$	0.0080	0.0107	0.0647	0.0677
Theoretical $\beta$	0.0408		0.0349	

For Powersil, the values of  $\beta$  are almost twice higher than the theoretical ones and the model underestimate the field dependency of the conductivity. This indicates that the conductivity mechanism in the material does not obey Poole-Frenkel dependence, at least as regards to the coefficient defined according to Equation 2.6. It can be observed that the calculated conductivity for Powersil is more than 10 times higher as compared to Elastosil. This difference is mostly related to the presence of ATH fillers in the composition of Powersil. A comparison of the conductivity values at 400 V with the results from standard tests shows a good agreement for both the materials. This confirms the supposition that the potential decay is predominantly controlled by the bulk neutralization.

#### 4.2.4 Trap density distributions

As discussed in Chapter 2 (see Equation 2.9), a plot of  $tdV/dt$  versus energy gap yields a direct image of trap density distribution for a material. Such plots obtained from the presented surface potential decay measurements, assuming the attempt to escape frequency  $\nu = 10^{11} \text{ s}^{-1}$  [14], are shown in Figure 4.6. Note that the parameter  $tdV/dt$  does not provide absolute magnitudes of the trap densities and the plot reflects only the shape of their energy distribution [10, 14]. One can observe that the trap density distribution for Elastosil sample is characterized by a relatively wide spread in energy with a narrow peak at about 0.91 eV. Similar characteristics were obtained in [14] for materials without ATH fillers. In case of Powersil, the spread of traps energies is lower as compared to that for Elastosil with the peak density at about 0.83 eV. It is notable that the distribution around the peak is not such narrow as for Elastosil material. Due to higher initial potentials for both materials, the negative charging results in higher trap densities as compared to positive charging. This may be due to appearance of stronger fields. Comparison of the trap distributions corresponding to positive

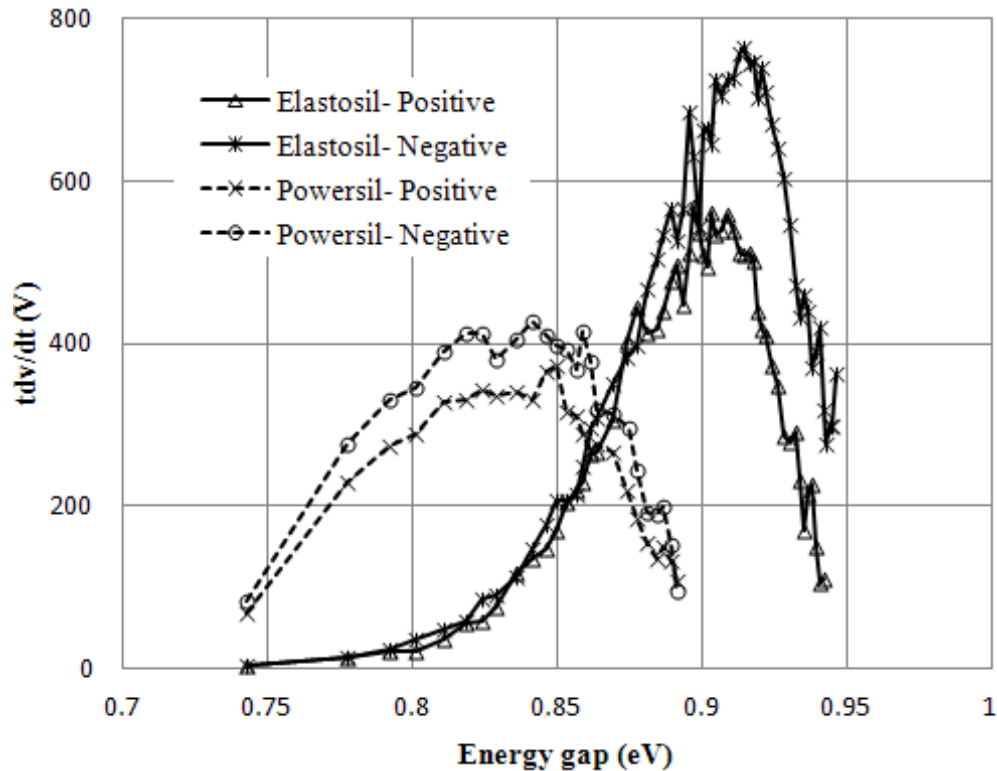


Figure 4.6. Calculated image of the trap energy distribution.

charging shows that Powersil is characterized by lower trap densities as compared to Elastosil even with similar initial potential levels. This could be due to different chemical structures of the two materials.

#### 4.2.5 Effect of charging conditions on decay

In order to investigate the effect of charging conditions on charge decay characteristics, a set of additional decay measurements was carried out on Elastosil samples charged using eight different charging regimes, which were achieved by varying parameters of the applied impulse voltages. The applied impulses were either lightning (LI) or switching (SW) impulses with peak magnitude of  $\pm 8$  kV. The charging was performed with a single pulse and with a series of three consecutive impulses.

Figure 4.7 shows the initial (1 minute after charging) surface potential distributions for the eight different charging conditions. One may observe that the distributions have a pronounced saddle-like shape, similarly to those registered in [14, 39]. In case of lightning impulses, positive charging led to a larger spot with higher amount of charges (higher potentials) than negative charging. This is in contrast to the case of switching impulses, for which no significant effect from the polarity of the applied voltage could be seen (the curves are almost symmetrical in regards to x-axis). Further, the potential distributions due to application of the single LI and the series of three impulses were almost identical. However for the case of switching impulses, the radius of the charged spot on the surface increased from  $\sim 1.5$  cm for the single pulse to  $\sim 2$  cm for three consequent impulses. Also, higher charge densities (potentials) were registered, except

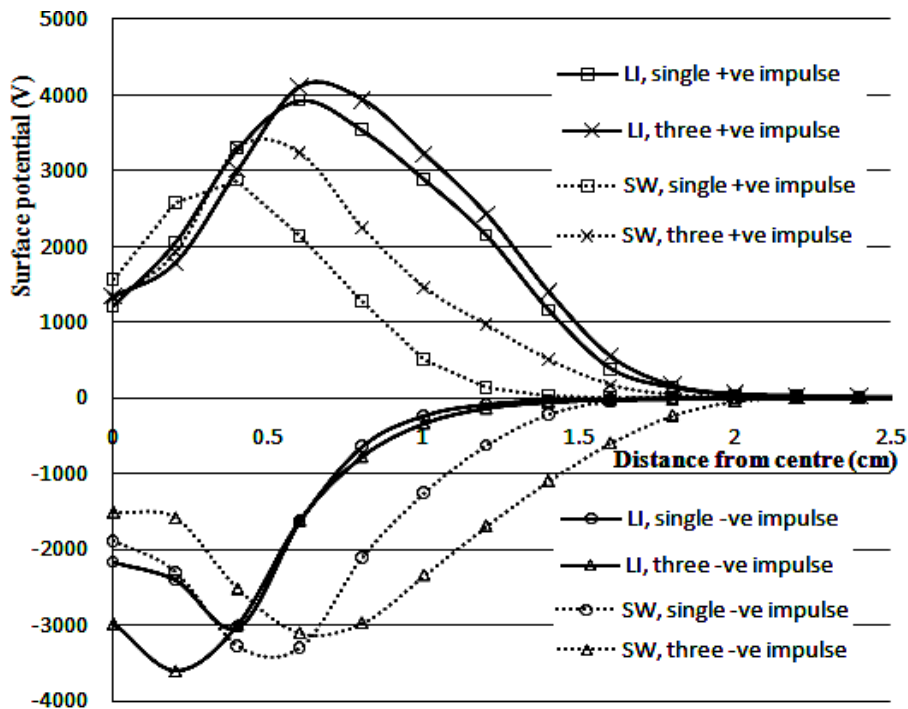


**Figure 4.7.** Measured surface potential distributions along a radial line; legend shows the details about charging.

those in the vicinity of the central point. One should stress here that the initial potentials were slightly varying from one trial to another due to statistical nature of the impulse corona as mentioned in the beginning of this section. Therefore, accurate generalization of the initial potential distributions would require additional extensive measurements and statistical treatment of the results. This, however, was out of the scope of the present study. The important observation here is that the considered charging conditions provided significantly different initial potentials.

Despite of the differences in the surface potentials recorded for different charging conditions, the measured data yield quite similar results in terms of field dependent conductivity and trap distributions. Thus, by utilizing the potential decay measured at the centre of the sample, the field (or voltage) dependent apparent bulk conductivity for each case was calculated and plotted against  $\sqrt{V}$  as shown in Figure 4.8. As it can be seen, the  $\log(\sigma)$  varies linearly with  $\sqrt{V}$  for all charging conditions that is in agreement with the Poole-Frankel model. Further, it can also be seen that all the charging conditions result in almost similar conductivity levels for potentials below  $\sim 1500$  V ( $\sqrt{V} \sim 38$ ), where the maximum deviation from the average value is less than 40%. When the potential exceeds  $\sim 1500$  V, the bulk conductivity increases more rapidly, as seen from the curves for the negative charging extending to higher  $\sqrt{V}$  values due to the higher initial potential at the center (Figure 4.7). This may be due to activation of some field dependent conduction processes. Variations of the trap energy distributions were also analyzed for different charging conditions and it was observed that they resulted in distributions similar to that shown in Figure 4.6 with the peak trap density at  $\sim 0.91$  eV.

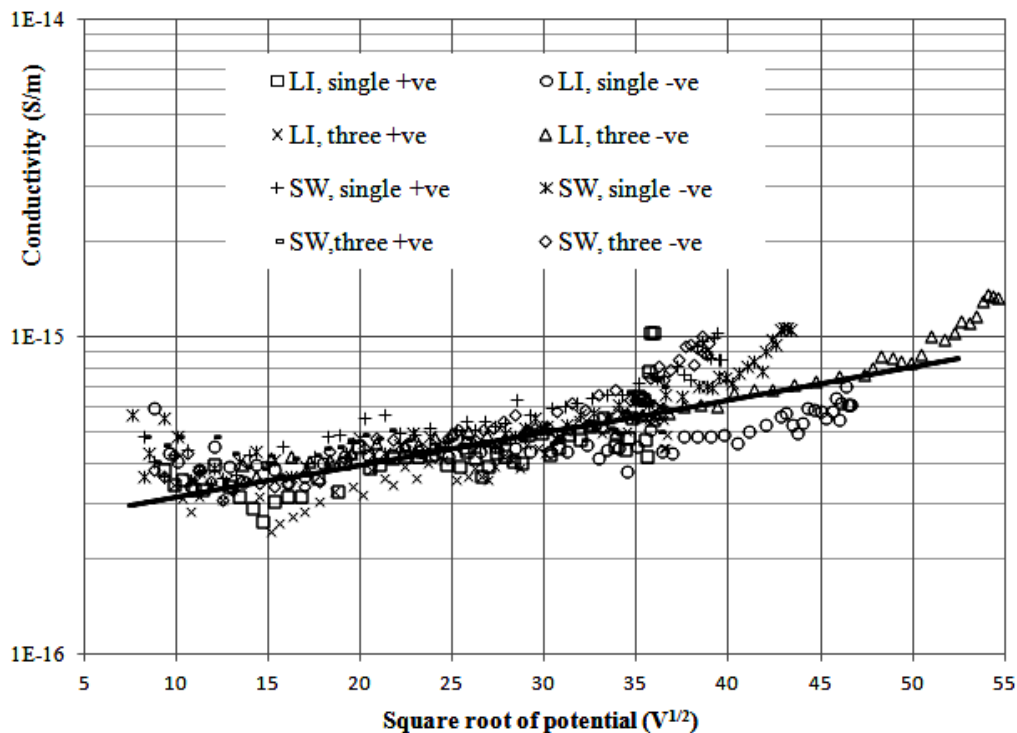


Figure 4.8. Calculated field dependent bulk conductivities; solid thick line represents the average among all the cases.

### 4.3 Contribution of gas neutralization to charge decay

This section presents the results obtained under the test conditions providing natural and enhanced levels of gas neutralization (see Section 4.1.4) for non-aged Elastosil and Powersil material samples. In this case also no charge leakage due to surface conduction was observed. Therefore, the surface potential decay was governed by bulk and gas neutralization mechanisms. Similar to the tests performed with zero gas neutralization, corona from the needle, energized by applying standard lightning impulses (1.2/50  $\mu$ s) with peak magnitudes of  $\pm 8$  kV, was used for charging. As the charging process is independent on the type of the neutralization, the shapes of the initial potential distributions observed in this case are similar to those presented above. Therefore, a detail discussion on the potential distributions is not included here.

#### 4.3.1 Decay due to bulk and natural gas neutralization

Figure 4.9 shows the normalized surface potentials measured at the centre of the sample during the decay under natural gas neutralization. It can be seen again that there is no significant effect of the polarity of the deposited charge on the decay characteristics. Due to the additional action of gas neutralization, the difference between the decay times for the two materials becomes less pronounced as compared

to the case of the zero gas neutralization, where only bulk neutralization was allowed (Figure 4.3). Thus, the time needed for the potential to decay to 50% of its initial value was  $\sim 1500$  s and  $\sim 9000$  s for Powersil and Elastosil respectively, meaning 6 times faster decay on Powersil samples. However, the rate of the decay to 10% was only twice higher. A comparison of these ratios with the corresponding ratios for other gas neutralization conditions is discussed separately below (Section 4.3.3). As shown in Figure 4.10, the decay rate for Powersil shows similar characteristics as in the case of bulk neutralization alone. In case of Elastosil, the decay rate becomes almost constant at higher potentials and converges to the same levels as for Powersil at lower potentials.

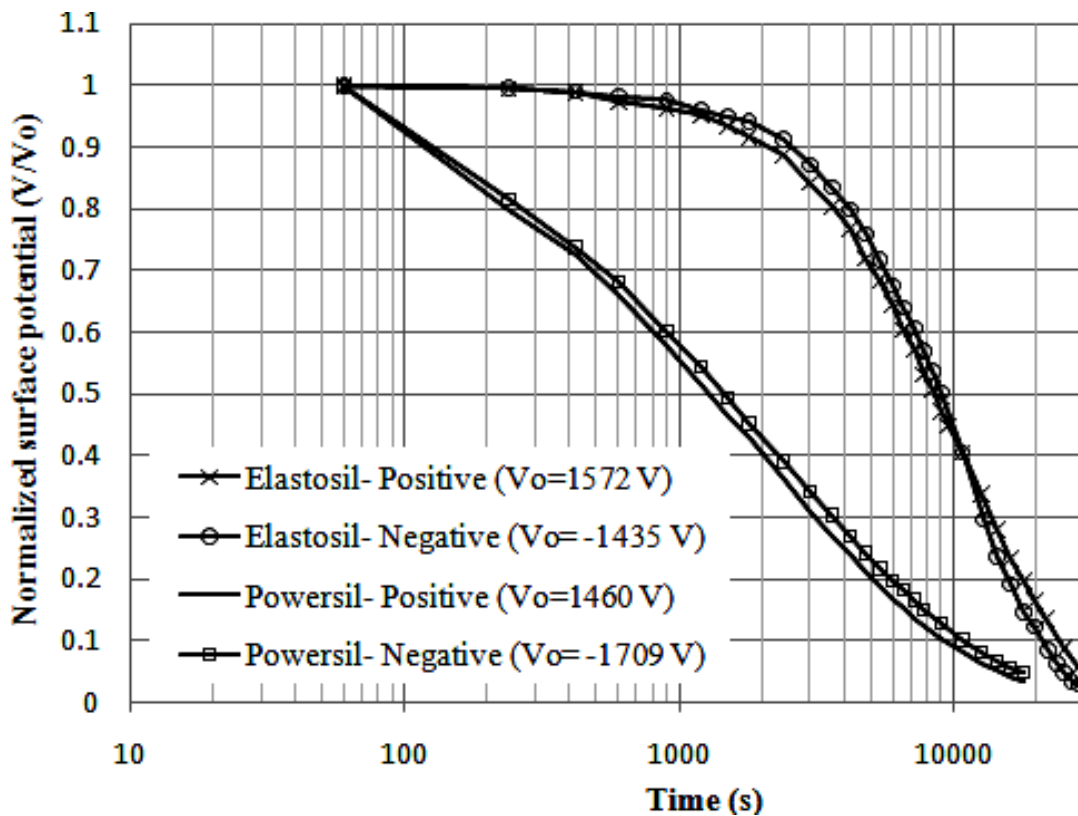


Figure 4.9. Decay of the normalized potential at the centre of the samples for natural gas neutralization; the legend shows the absolute value of the initial potentials.

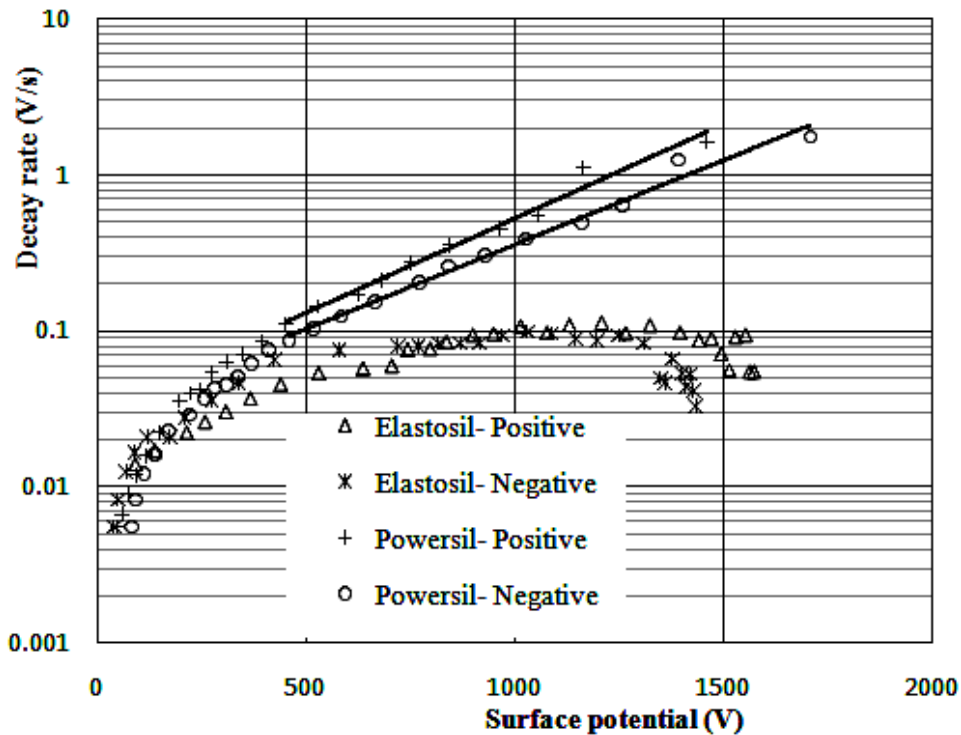
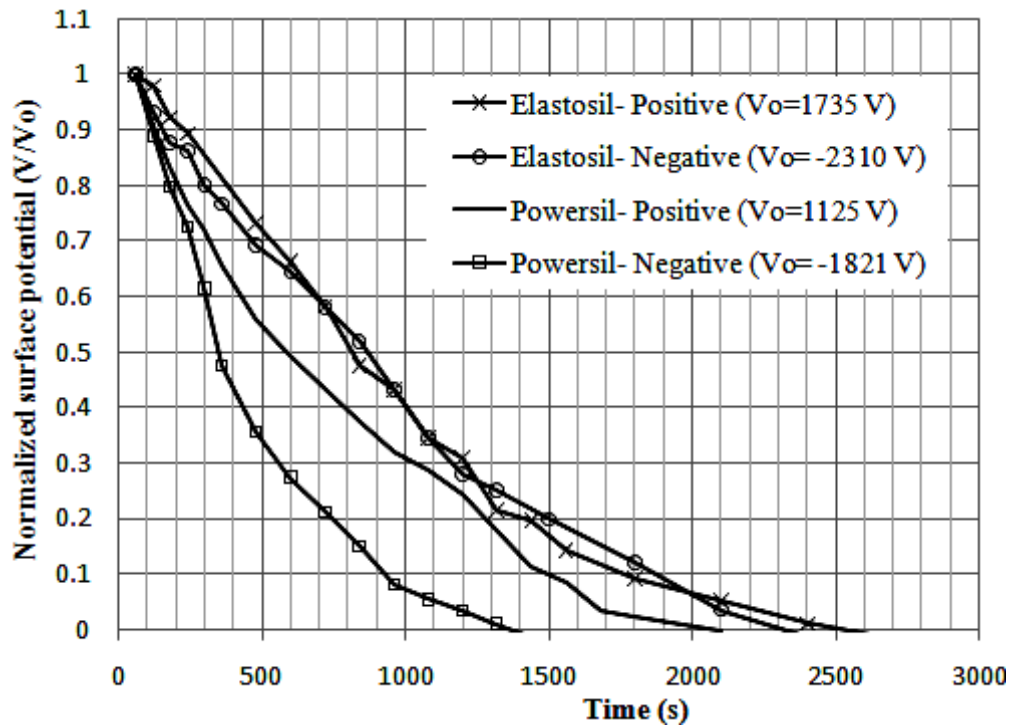


Figure 4.10. Variations of the calculated decay rate with surface potential magnitude.

#### 4.3.2 Decay due to bulk and enhanced gas neutralization

Similarly to the case with natural neutralization, the discussion here is also limited to the potential decay at the sample center. As shown in Figure 4.11, the charge decay becomes very fast for both material types in presence if enhanced gas neutralization. It is worth mentioning that the repeatability of the decay characteristics in this case was not so good. Sometimes the charge decayed very fast while at other times it took longer time, which could be related to sensitivity of the enhanced ions concentrations to external factors, especially disturbances in air flow around the material samples. Thus, the results shown demonstrate the most common features observed within several trials. As it can be seen, the decay is independent on the polarity of the deposited charge on Elastosil sample while a weak dependence can be noticed for Powersil. In general, the differences in the characteristics of the materials are less pronounced as compared to the cases discussed above. The time needed for the decay of the surface potential down to 50 % of the initial value was less than 1000 s whereas the decay down to 10% took less than 2000 s. As the curves are similar to each other, the decay rates are not presented here, though some of them are provided in the next section for comparison with other gas neutralization conditions.



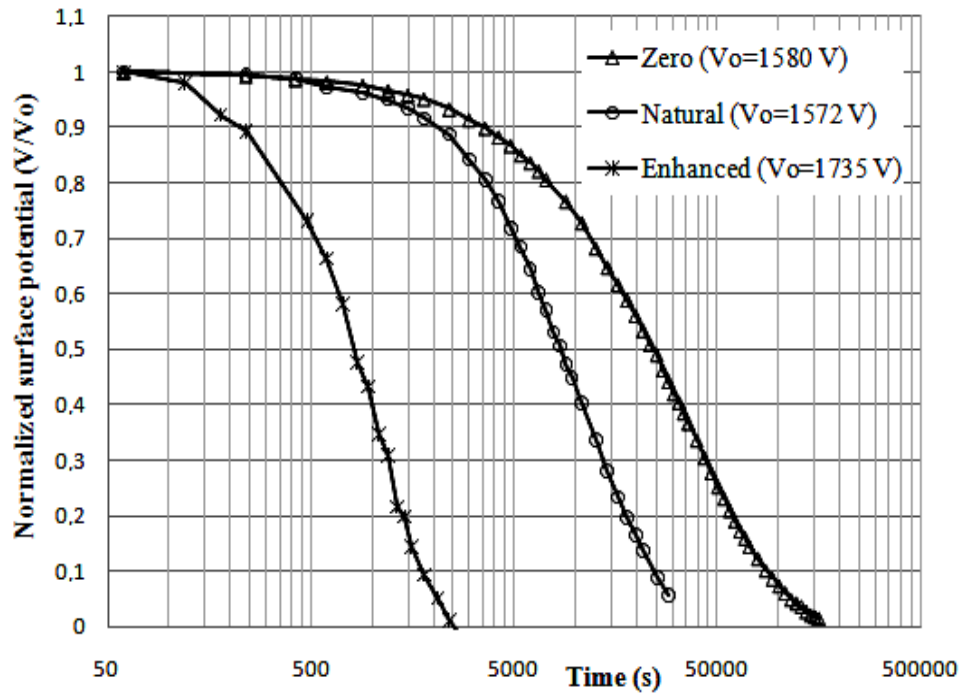
**Figure 4.11.** Decay of the normalized potential at the centre of the samples for enhanced gas neutralization; the legend shows the absolute values of the initial potentials.

### 4.3.3 Comparison of three gas neutralization modes

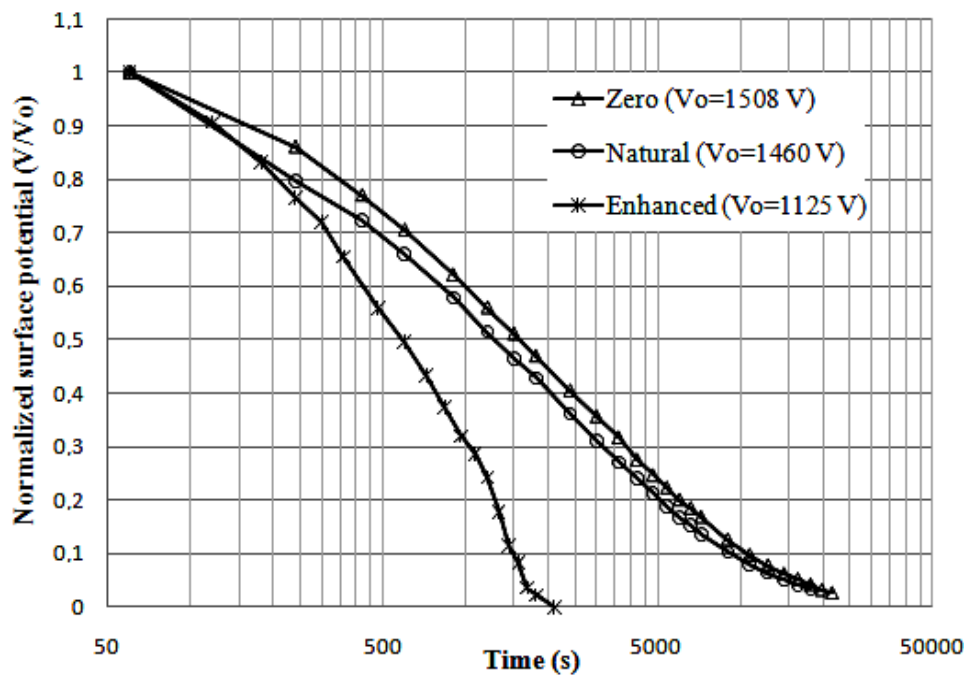
So far the decay characteristics were compared for different polarities of charging and for different types of materials. This section focuses on analyzing the difference arising due to different gas neutralization conditions utilizing the results already presented above. As the polarity of charging has no significant effect on the charge decay characteristics, the discussion concentrates only on positively charged surfaces.

Figure 4.12 shows the potential decay characteristics recorded at the centre of the positively charged samples for each test condition while corresponding decay rates are shown in Figure 4.13. As it is seen, the potential decay becomes considerably faster in case of Elastosil when the natural gas neutralization is allowed. It reduces the time needed for the decay to 50% of the initial value from 25,000 s to 8,000 s, which is almost 3 times faster. The time needed to decay to 10% level is reduced from 87,000 s to 24,000 s, which is also more than 3 times. Correspondingly, the decay rate also increases considerably, as seen in Figure 4.13a. The contribution from the gas neutralization becomes more and more pronounced when the magnitude of the surface potential becomes lower. Under the condition of enhanced gas neutralization, when the free ions densities were about 10 times higher than that under the natural conditions, the potential decay is very fast and the times needed to decay to 50% and 10% are reduced by factor of 10 as compared to the natural conditions. As can be seen from Figure 4.13a, the decay rate is also about 10 times of that at natural conditions.

4.3. Contribution of gas neutralization to charge decay

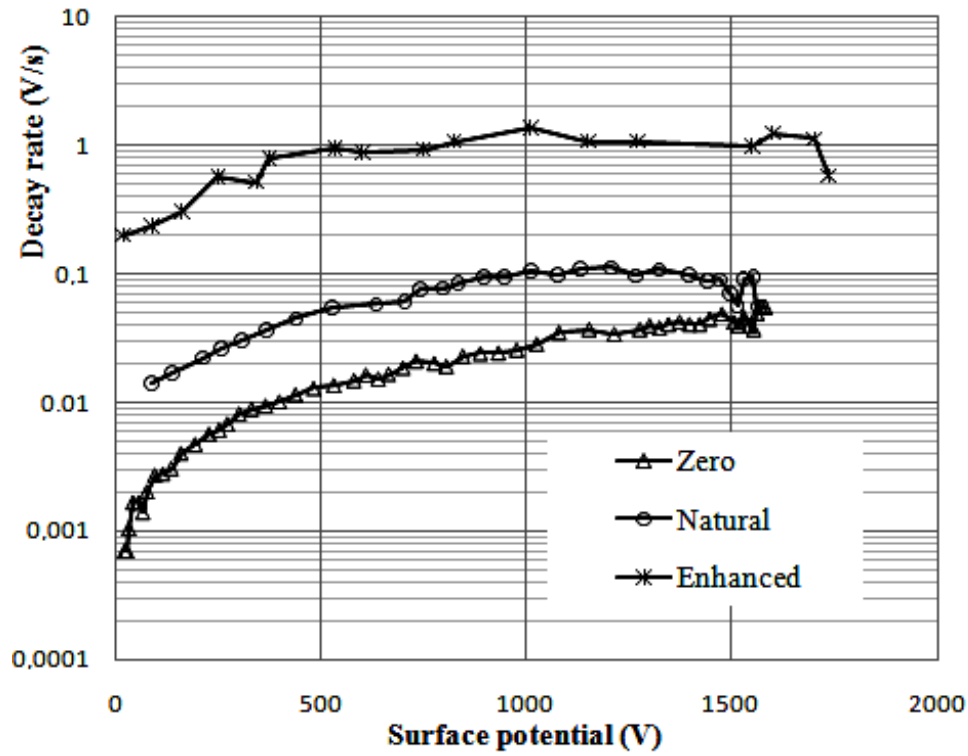


(a) Elastosil

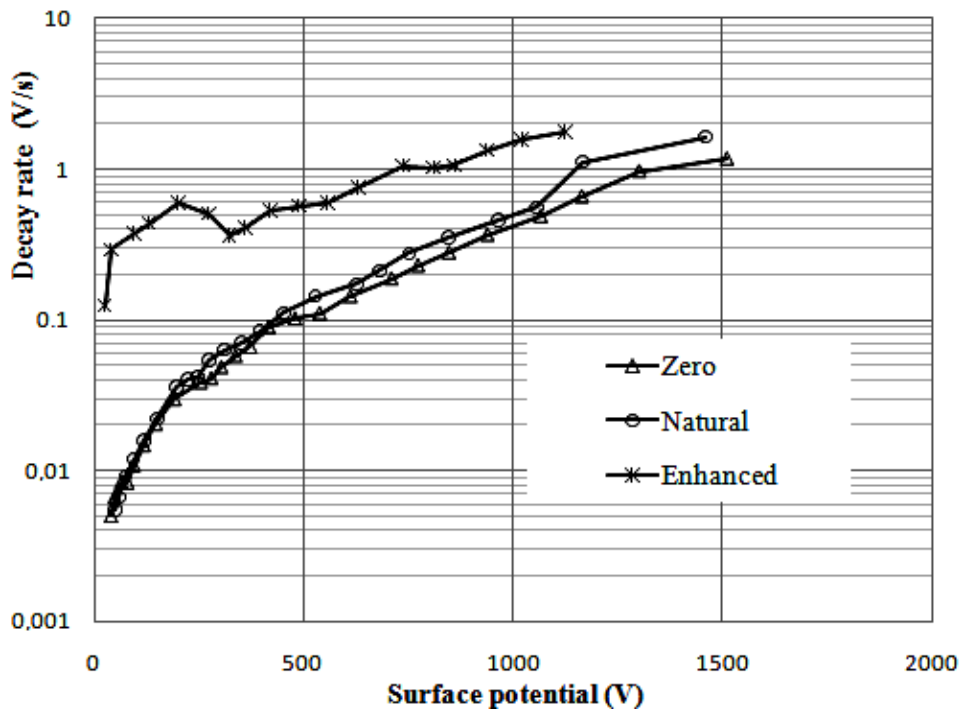


(b) Powersil

Figure 4.12. Decay of the normalized potential at the centre of the samples for different neutralization modes.



(a) Elastosil



(b) Powersil

Figure 4.13. Variations of the calculated decay rate with potential for different neutralization modes.

For Powersil, the level of free ions corresponding to natural conditions does not accelerate the decay process significantly (see Figure 4.12b) and the decay rate does not change considerably (Figure 4.13b). This indicates that in this particular case the decay due to bulk neutralization is much more effective than the decay due to gas neutralization and the contribution of the latter to the total decay is weak. However, the increased concentration of free ions in air amplifies the gas neutralization process and the decay becomes faster, especially at low potential magnitudes. Thus, the time needed to decay to 50% is reduced by half whereas the time for decay to 10% is reduced by a factor of 12. This indicates stronger differences in the decay rate at lower potentials as compared to its higher magnitudes (Figure 4.12b). One may therefore conclude that the effect of the enhanced gas neutralization at low surface potentials is of the same efficiency as the effect of apparent bulk conductivity at higher potentials. During potential decay, the field dependent apparent bulk conductivity decreases and the effect of gas neutralization becomes more and more pronounced.

## 4.4 Contribution of surface conduction to charge decay

This section presents results of charge decay measurements performed on artificially aged non-postcured Elastosil samples, for which a significant increase of surface conductivity was registered. Aging was achieved by exposing sample's surface to corona discharges, usually referred as corona treatment. As all the measurements were performed under zero gas neutralization condition, charge decay is due to bulk neutralization and surface conduction. A standard lightning impulse with the amplitude of +11 kV was used as charging voltage. In addition, the effect of moisture content in the surrounding gas environment was analyzed.

### 4.4.1 Corona treatment

One side of each sample was exposed to ac corona discharges for 100 h using a multi-needle electrode system mounted in a chamber ventilated by dry air (<1% relative humidity). Magnitude of the voltage applied to the needle electrode was 20 kVrms. The rate of air flow was set to 5 L/min [96]. The corona needles were mounted on a metallic disk and were arranged in a way that the electric field at the surface of the treated sample lying on the counter flat electrode was almost homogeneous. The minimum distance between the sample surface and the needles tips was 40 mm. More details about the multi-needle electrode system can be found in [97]. The released power obtained by measuring the applied voltage and the voltage drop across a capacitor connected in series with the multi needle electrode [97], was ~1.6 W. During the corona exposure, the material sample surface was also affected by ozone and UV radiation produced in the discharge. Ozone concentrations were maintained at the levels of ~45 ppm during corona treatments [96]. The measurements of NO<sub>x</sub> content

**Table 4.4.** Measured volume and bulk conductivities. Numbers inside the brackets show the ratio with respect to the corresponding values for untreated samples.

Treatment method	Volume conductivity (S/m)	Surface conductivity ( $\Omega \cdot \text{sq}$ ) <sup>-1</sup>
untreated	$1 \cdot 10^{-15}$	$5 \cdot 10^{-19}$
treated	$2 \cdot 10^{-15}$ (2)	$5 \cdot 10^{-17}$ (100)

revealed that concentrations of these species were below 1 ppm. After completion of the treatment, each of the treated samples was left for a sufficiently long time in a room environment for decaying the residual charges. It was thereafter placed on a grounded copper plate for charging and surface potential decay measurements according to the procedure described above.

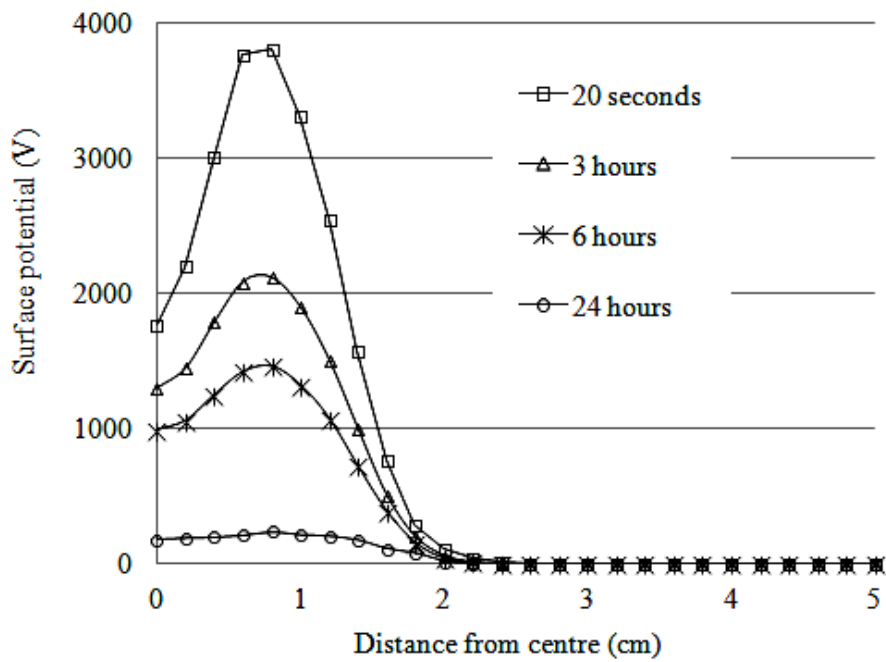
In addition, measurements of volume and surface resistivities were conducted prior and after the corona treatment on another set of identical samples. The experiments were performed according to the ASTM standard D257 using Keithley electrometer 6517A with the test voltage of 400 V (to achieve optimal accuracy). The results of these measurements are shown in Table 4.4. The tabulated conductivity values were obtained using current magnitudes recorded at 12 hours of test voltage application. It can be observed that corona treatment did not influence significantly the volume conductivities although some variations could be noticed from sample to sample. In contrast, surface conductivity was increased by two orders of magnitude as compared to that for untreated samples. This behavior could be attributed to the high corona intensity and, correspondingly, a strong ionic flow conditioned by a continuous charging and discharging of the sample surface that restricted accumulation of surface charges.

#### 4.4.2 Potential distributions

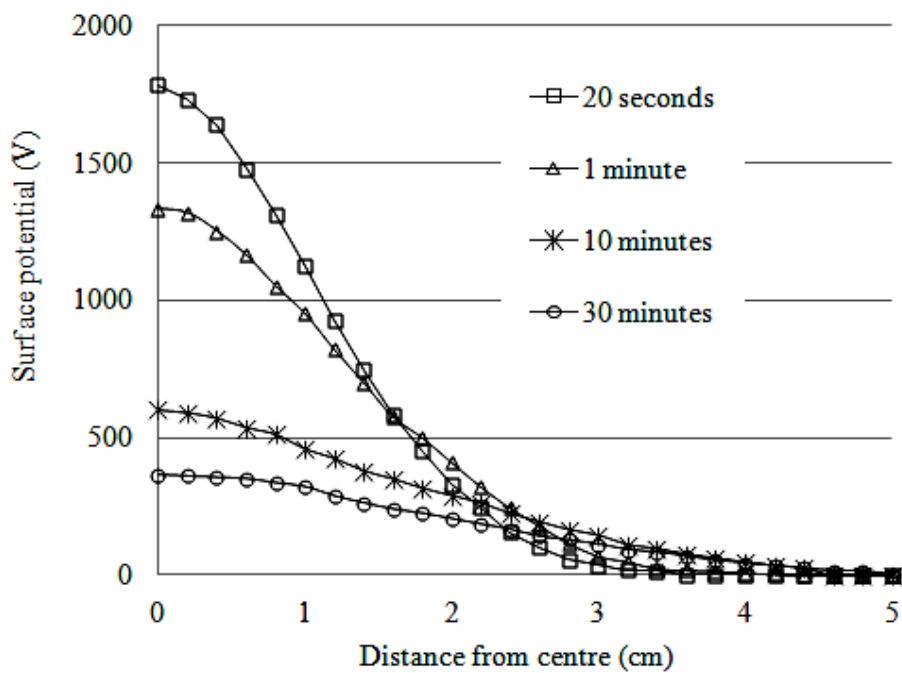
Figure 4.14 shows the surface potential profiles along a line originating from the point, above which the needle electrode was placed during the charging (the curves can be symmetrically be mirrored relative to the vertical axis at zero co-ordinate). One may clearly distinguish differences in shapes of the distributions. Thus, the potential measured on the untreated sample has a local minimum at the center and its peak is located at  $\sim 0.8$  cm away from the central point that yields a saddle-shaped profile. In case of the corona treated material, the peak of the surface potential is at the central point, thus the distribution is bell-shaped. The different appearances of the distributions can be attributed to specific conditions of charge accumulation on the samples during corona charging. Thus, while reaching the surface, the charge carriers are trapped in deep surface traps (as discussed further below) and their density may

#### *4.4. Contribution of surface conduction to charge decay*

become high enough to modify the electric field and to initiate back discharges that partially compensate the deposited charges, resulting in the saddle-shaped potential profiles as discussed in Section 4.2.1. This process is prevented if charge leakage along the surface is essential, as is in the case of corona treated material. Thus, it can be observed in Figure 4.14a that the charged area on the surface of the untreated sample is confined to a spot with the radius of  $\sim 2$  cm and it does not expand with time. In contrast, the expansion is larger in case of the treated sample and the charged spot grows from  $\sim 3$  cm up to  $\sim 5$  cm in radius reaching the edge of the sample at  $\sim 30$  minutes after the charging, as seen in Figure 4.14b. This behavior clearly indicates charge leakage to the grounded electrode along the surface that is most intensive during first moments after the charging, when the decay is fastest (Figure 4.14). The latter is also the reason for the differences in the maximum values of the surface potentials measured 20 s after completing the charging stage (note that this was the shortest possible time to start the potential measurements). In the case of the treated sample, the magnitude of the potential is almost two times lower than its maximum value obtained on the untreated material indicating that a significant portion of the surface charge is already decayed within the initial 20 s.



(a) Untreated sample



(b) corona treated sample

**Figure 4.14.** Measured surface potentials on (a) untreated and (b) corona treated Elastosil samples charged by +11 kV lightning impulse. The legend indicates times after charging.

### 4.4.3 Surface potential decay

Typical time variations of the surface potentials measured at the center of the sample are shown in Figure 4.15. One can clearly observe that the potential decay on the treated material is much faster as compared to untreated ones. It took  $\sim 25,000$  s for the surface potential to drop to 50% of its initial value in case of untreated material, while this time became less than 100 s for the treated sample. In the latter case, the process was found also to be sensitive to relative humidity (RH) of surrounding air (especially at longer times), whereas the humidity did not play any role during the potential decay of the untreated material. Thus, the recorded times needed for surface potential to decrease down to 10% of the initial value were  $\sim 2500$  s and  $\sim 1000$  s at 48% RH and 60% RH, respectively. The faster surface potential decay on ac corona treated material correlates well with the increase of its surface conductivity (see Table 4.4). Therefore, one may state that bulk conduction governs the decay process on the non-treated material while in the case of treated material it is predominantly due to surface conduction.

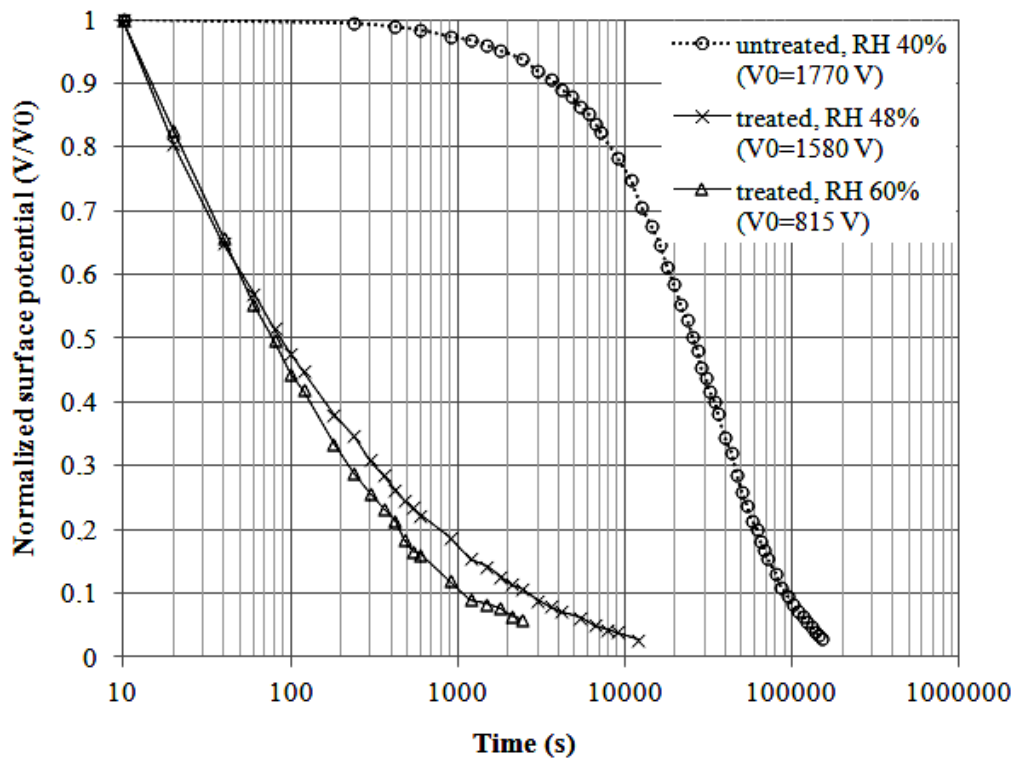


**Figure 4.15.** Decay of normalized potential at the centre of the samples; legend shows the treatment condition, relative humidity and the absolute values of the initial potentials.

#### 4.4.4 Influence of relative humidity

In order to identify the dependency of the charge decay on relative humidity in case of the treated sample, a set of measurements was performed at different moisture contents in ambient air. As the experiments were conducted without regulating the atmospheric conditions, the RH varied slightly over time. However, since the decay process took less than 1 hour, those variations were within  $\pm 3\%$ . The decay rates ( $dV/dt$ ) calculated at different potential levels are shown in Figure 4.16 as functions of corresponding RH. It can be observed that the decay rate exponentially increases with the increase of RH within the tested range at all three potential levels. The increase of the RH from 45% to 62% results in 43 and 28 times higher decay rate for 200 V and 800 V, respectively. This indicates a very high sensitivity of the decay process to the moisture content that is most probably resulting from the chemical changes taking place on the material surface during exposure to the corona discharge. Such modifications are confirmed by the results of the FTIR (Fourier transform infrared spectroscopy) measurements and XPS (X-ray photoelectron spectroscopy) analysis, presented in [96, 97]. The increased amount of water absorbed in humid environment by the surface layer can increase surface conductivity significantly [49] thus leading to stronger leakage of charge on the sample surface.

#### 4.4.5 Trap density distributions

An image of trap density distributions for untreated and ac corona treated samples predicted by calculating  $tdv/dt$  is shown in Figure 4.17. One can observe that the distribution in the case of untreated sample is characterized by a relatively wide spread

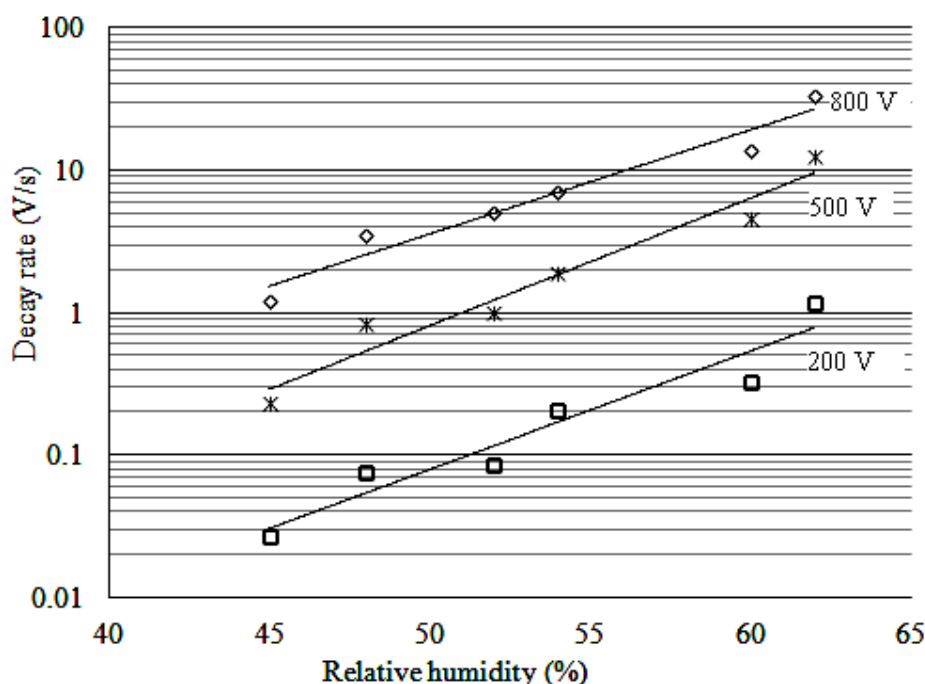


**Figure 4.16.** Variation of the calculated decay rate with relative humidity; the numbers at the curves indicate the potential at which the decay rate was calculated.

in energy with a peak at about 0.91 eV. For the treated material, however, the energy gap is shifted towards lower values and the position of the peak cannot be identified (measurements of the potential decay rate at short instants would be needed to obtain this peak). However according to the trend in the distribution, the peak can be expected at energies lower than 0.73 eV and the corresponding density of the traps is much higher than that for the virgin material. This indicates that the corona treatment reduced the energy barrier for charge de-trapping that facilitates hopping conduction mechanism on the surface and, hence, speeds up the decay process.

The data from Figure 4.17 can be utilized to analyze conductivities of the material. Thus assuming that the conduction process can be described by the energy band model [98], the ration between the conductivities resulting from two different energy gaps  $E_g$  can be written as

$$\frac{\sigma_1}{\sigma_2} = \frac{\exp(E_{g1}/kT)}{\exp(E_{g2}/kT)} \quad (4.1)$$

Representing each trap energy distribution in Figure 4.17 by its peak value (e.g., 0.9 eV for the untreated and 0.7 eV for treated material), the ratio in Equation 4.1 is  $\sim 52$  that correlates well with  $\sim 45$  times faster surface potential decay observed for the treated samples. It is worth noting that such estimation accounts for all the decay mechanisms (e.g., in the case of corona treated material it includes both volume and surface conduction) and, therefore, the obtained agreement is quite unexpected.

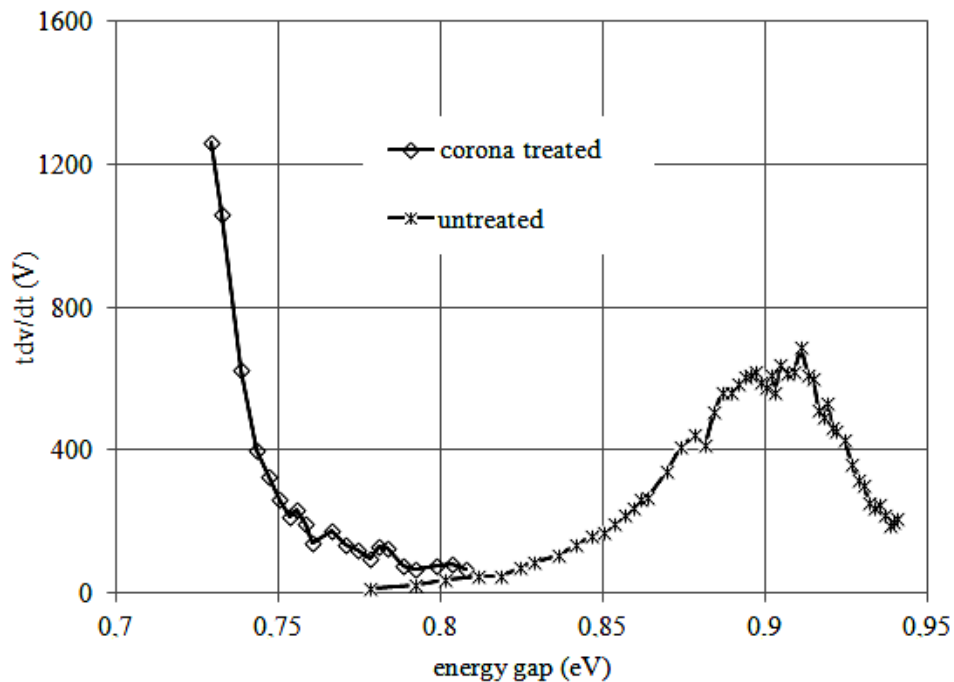


Figure 4.17. Calculated image of trap density distributions for untreated and treated sample.

## 4.5 Comparison of different decay mechanisms

This section summarizes the decay measurements presented above for positively charged Elastosil samples. The discussion is limited only to Elastosil as Powersil was not considered for the studies with corona aged samples, where surface conduction contributes to the decay. Table 4.5 sum-ups the obtained results in terms of the times needed for surface potential to decay down to 50% and 10% of its initial value under action of different decay mechanisms. Corresponding decay curves are already presented in Figures 4.12a and 4.15 above. It can be clearly seen that presence of gas neutralization or surface conduction results in significant speed up the decay process. However, the effect of natural gas neutralization is much less pronounced as compared to the enhanced gas neutralization and surface conduction. When considering the complete decay, i.e. down to 10%, the enhanced gas neutralization (10 times higher ion concentrations as compared to natural air) and surface conduction (100 times higher compared to case of “bulk neutralization” in the Table 4.5) has similar effects on charge decay. However when considering initial stage of the decay, i.e. down to 50%, surface conduction results in 10 times faster potential drop as compared to the enhanced gas neutralization. This indicates that surface conduction is more effective when surface potential and, hence, electric field is high enough to transport charges along material surface.

**Table 4.5.** Comparison of decay times under different decay conditions.

Active decay mechanisms		Time needed for potential decay (s)	
		to 50%	to 10%
Bulk neutralization		25,000	87,000
Bulk and gas neutralization	Natural	8,000	24,000
	Enhanced	1,000	2,000
Bulk neutralization and surface conduction*		< 100	1,000 - 2,500

\*in case of relative humidity in the range of 48% - 60%.

# 5 Surface charging of cylindrical polymeric insulator

This chapter focuses on experimental study of surface charge profiles on a model cylindrical polymeric insulator consisting of a glass fiber reinforced epoxy core covered with a layer of silicone rubber. The charging was realized in two different ways reflecting conditions that may appear in service: i.e. by utilizing an external dc corona source and by pre-stressing the insulator with a dc voltage. A set of experiments was carried out with the external corona source to investigate effects of its intensity, duration of application and location with regard to the insulator surface. For all the conditions, surface potential distributions were measured 1 min after completing the charging process. Further, the  $\Phi$ -matrix method was utilized to obtain surface charge density profiles from the measured potential distributions.

## 5.1 Experiments

The insulator sample used was cylindrical in shape and consisted of a glass fiber reinforced epoxy core (108 mm length, 30 mm diameter) covered with 4 mm thick layer of silicone rubber (see Figures 5.1 and 5.3). The relative permittivities of the core and cover materials were 4 and 3.5, respectively, whereas the electrical conductivities of both the materials were  $\sim 10^{-14}$  S/m [99]. The sample was held between two round shaped metallic electrodes, which were solidly mounted on a wooden basement. As 3 mm on each side of the insulator were inserted into grooves on the metal electrodes, the effective length along the surface was 102 mm. All the measurements were performed under ambient laboratory conditions and the temperature, pressure and relative humidity were, respectively, within the ranges of 20–22 °C, 980–1020 hPa and 40–50%.

### 5.1.1 Setup for surface charging

The experimental setup used for charging of the insulator sample by external corona is shown in Figure 5.1. The external corona discharge was initiated from 27 galvanically

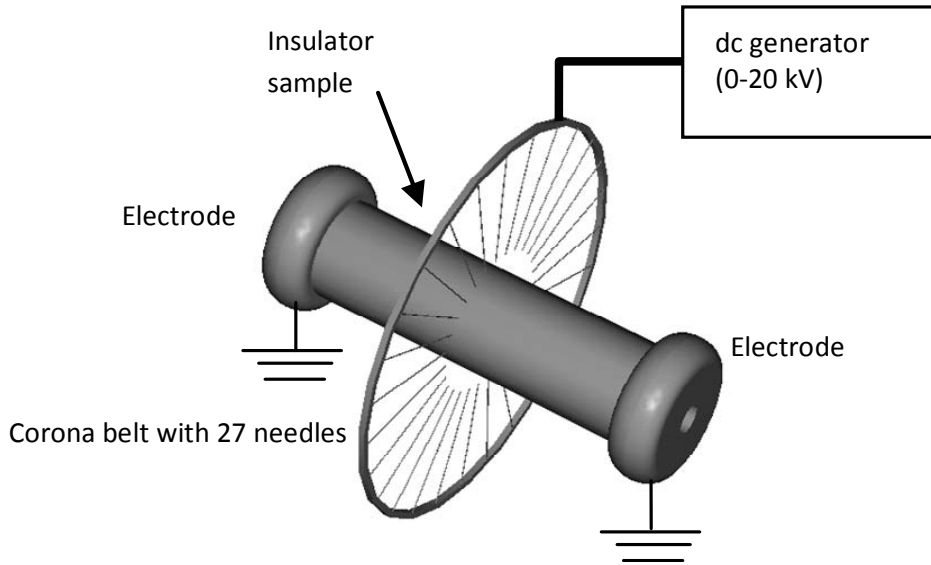


**Figure 5.1.** Setup for charging by external corona source

connected needles, mounted on a solid support (hereafter referred as a corona belt). The space between two adjacent needle tips was 1 cm. The distance between the needle tips and sample surface was maintained at  $\sim 0.7$  cm. These dimensions, the space between the needles and the distance between the needles tips and surface were selected in such a way to get a rotationally symmetric charge deposition. During charging, the belt was arranged symmetrically around the sample surface at a desired position along the axis and both the electrodes were kept grounded while the needles were connected to a dc generator (Spellman SR6), which supplied up to  $\pm 20$  kV. In case of charging by pre-stressing, the corona belt was removed and one of the electrodes was connected to a dc generator which provided up to  $-100$  kV, while the other electrode was kept grounded. Note that one of the electrodes was kept grounded permanently irrespectively of the charging method used.

### 5.1.2 Setup for surface potential measurements

The experimental procedure for measuring surface potential distributions, using the same electrostatic voltmeter as used for the experiments described in Chapter 4, is illustrated in Figure 5.2. The probe-to-surface distance was maintained at 3 mm, while positioning of the probe along the insulator was achieved by means of a computer controlled XY-positioning system (Arrick Robotics). A computer equipped with a data acquisition card was used to collect and record the experimental data, which include surface potential and indication of the probe position. It is worth to mention that both the electrodes were kept grounded during the surface potential measurements.

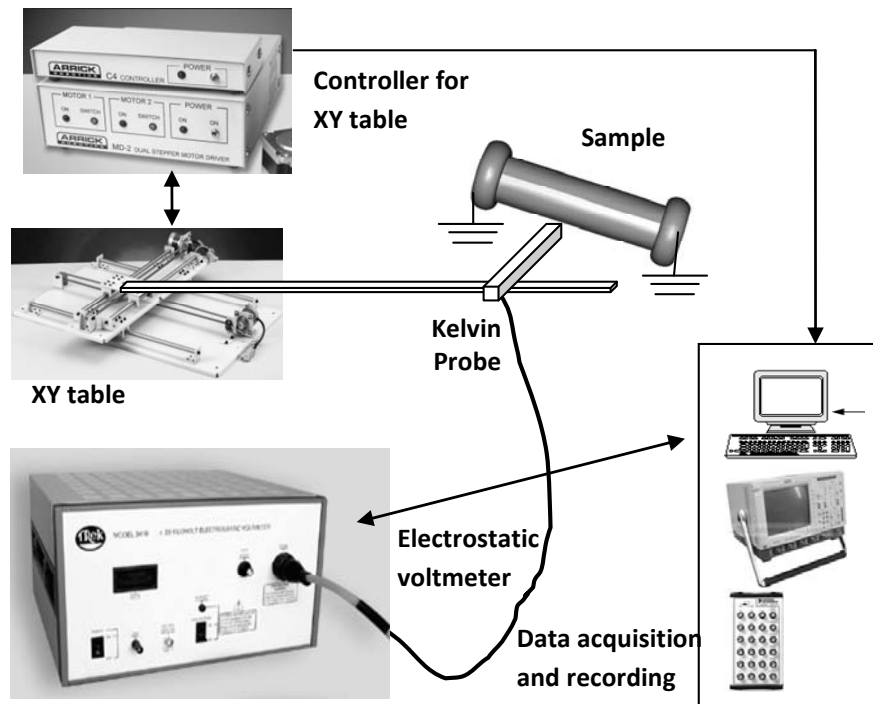


Figure 5.2. Experimental setup used for surface potential measurements.

### 5.1.3 Experimental procedure

Before the charging, the insulator samples were cleaned with isopropanol to remove residual charges deposited during sample handling and thereafter dried. An initial scan of the surface potential was conducted to check that the insulator was properly neutralized. Afterwards, the corona belt was mounted at the required position as accounted along the insulator axis. The considered positions were at the center (zero coordinate), at  $\pm 1$  cm and  $\pm 3$  cm from the center (positive co-ordinates correspond to the direction towards the permanently grounded electrode). Then, the needles were energized with the required dc voltage ( $\pm 7$  kV,  $\pm 10$  kV,  $\pm 15$  kV and  $\pm 20$  kV were used). In most of the experiments, the duration of the corona charging was chosen to be 2 min. The influence of the charging time was also investigated by changing it to 1 min and 3 min (the results are presented below). Upon completing the charging process, the voltage supply was turned off and the corona belt was grounded. After that the belt was carefully removed and the potential probe was brought to one end of the scanning span, which was a straight line along the surface parallel to the axis and ranging from +4.2 cm to -4.2 cm. The whole process of removing the belt and positioning of the probe took about 30 s. The scanning always started at 1 min after the charging from the position +4.2 cm and included 25 measuring points along the span. The distance between two measuring points was 2.5 mm in the region closer to middle of the insulator whereas it was 5 mm closer to the electrodes. The total measuring time was about 25 s. As the charged region formed on the surface was symmetrical around the sample, a single scan along the line parallel to its axis was sufficient for obtaining surface potential pattern for the whole insulator. In case of charging by pre-stressing, one of the electrodes was energized with the desired dc

voltage level for 2 min. After charging was completed, the dc voltage supply was turned off and both the electrodes were grounded. The surface potential measurement started also in this case 1 min after charging in a similar manner as described above for the case of charging with the corona belt.

## 5.2 Calculation of charge densities

Unlike flat material samples kept on a grounded plane, the considered cylindrical insulator model results in complex field distribution consisting of both tangential and normal components. As explained in Chapter 2, simple analytical methods are not suitable for such objects and the  $\Phi$ -matrix method needs to be utilized. This section discusses the  $\Phi$ -matrix method and its application for the above experiments.

### 5.2.1 The $\Phi$ -matrix method

The idea behind this approach is to define contributions of charges present at different locations on the analyzed surface to the potential induced at the position where it is measured by the probe [56]. For this, the surface under consideration needs to be divided into certain number of elements whose size and shape are to be selected according to the test object geometry and surface potential scanning procedure. Further, the probe potential at  $i^{\text{th}}$  element,  $V_i$ , can be expressed as:

$$V_i = \sum_{j=1}^n \phi_{i,j} \sigma_j \quad (5.1)$$

Here,  $\phi_{i,j}$  is the potential at  $i^{\text{th}}$  element due to a unit charge density located at the  $j^{\text{th}}$  element;  $\sigma_j$  and  $n$  represents the charge density at  $j^{\text{th}}$  element and number of elements on the surface, respectively. As there are  $n$  numbers of measured potential values available and each of those is a function of  $n$  charge densities, the whole problem can be represented by  $n$  equations and can be written in the matrix form as:

$$[\mathbf{V}]_{n,1} = [\Phi]_{n,n} [\boldsymbol{\sigma}]_{n,1} \quad (5.2)$$

Obtaining the  $\Phi$ -matrix requires electrostatic field calculations with exact geometric structure including the probe. Usually such calculations need to be done using numerical calculation tools. Knowing the  $\Phi$ -matrix, the measured probe potentials can be used to obtain unknown surface charge distributions by solving the matrix equation:

$$[\boldsymbol{\sigma}] = [\Phi]^{-1} [\mathbf{V}] \quad (5.3)$$

### 5.2.2 Obtaining the $\Phi$ -matrix

Calculations of the coefficients in  $\Phi$ -matrix were carried out using numerical simulation software Comsol Multiphysics. For the computations, the geometry of the measuring setup including the insulator, the electrodes, grounded floor and the probe was represented in a 3D computational domain as shown in Figure 5.3. As the cylindrical surface was charged with the symmetrical corona belt, the resulting charge distributions were assumed to be rotationally symmetric. Therefore, the insulator surface was divided into 27 ring shaped elements, 25 of which were within the scanning span and corresponded to the points where the surface potential was measured (see experimental procedure in Section 5.3). Each of the other two extra rings was located between the ends of the scanning span and the electrodes. Similarly to the distance between two measuring points, the width of the ring element was 2.5 mm in the middle region and 5 mm closer to the electrodes. The potential values for those rings were obtained by interpolating the corresponding potential at the end point of the scanning span and the electrode potential, which was zero for both the electrodes during the measurements. In order to calculate an element in the  $\Phi$ -matrix, a certain charge density was assigned for a ring element while it was set to zero for all other elements. The probe was consequently placed at different elements on the surface for which the induced potential from the specified charge density had to be obtained. Unlike for the capacitive probes, the field nullifying effect inherent for Kelvin type probes, needed to be taken into account. To achieve this, the potential of the probe was initially set to a certain value, which was changed within a specified range using parametric sweep option available in the software. For each of these probe potential values, the electrostatic field and the potential on the insulator surface were calculated. The value of the matrix element was obtained when the probe potential was

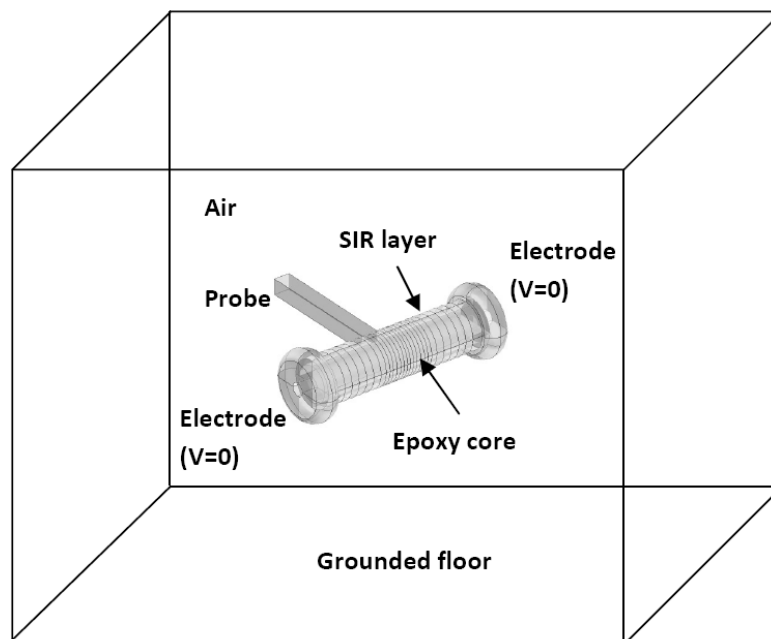


**Figure 5.3.** Schematic diagram of the computational domain.

equal to the measured potential of the ring element at which the probe was located. In general, this procedure needs to be repeated  $27 \times 27$  times to obtain all the elements in the  $\Phi$ -matrix. However due to the geometrical as well as electrical symmetry of the system, the calculations were performed for  $14 \times 27$  elements.

The obtained responses of the probe, i.e., surface potentials induced by  $+1 \mu\text{C}/\text{m}^2$  charge density assigned to different surface elements, are shown in Figure 5.4. The legend shows the position of the charge corresponding to each curve. The smooth shapes of the probe response curves confirm the adequate spatial resolution for the surface charge calculations. When a charge is located at the centre element, the induced potential on the element 2.2 cm away is as high as 23% of the potential on the same element, where the charge is located. On the other hand when the charge is placed on an edge element, the potential  $\sim 15\%$  of the one on that element is induced on the centre of the insulator.

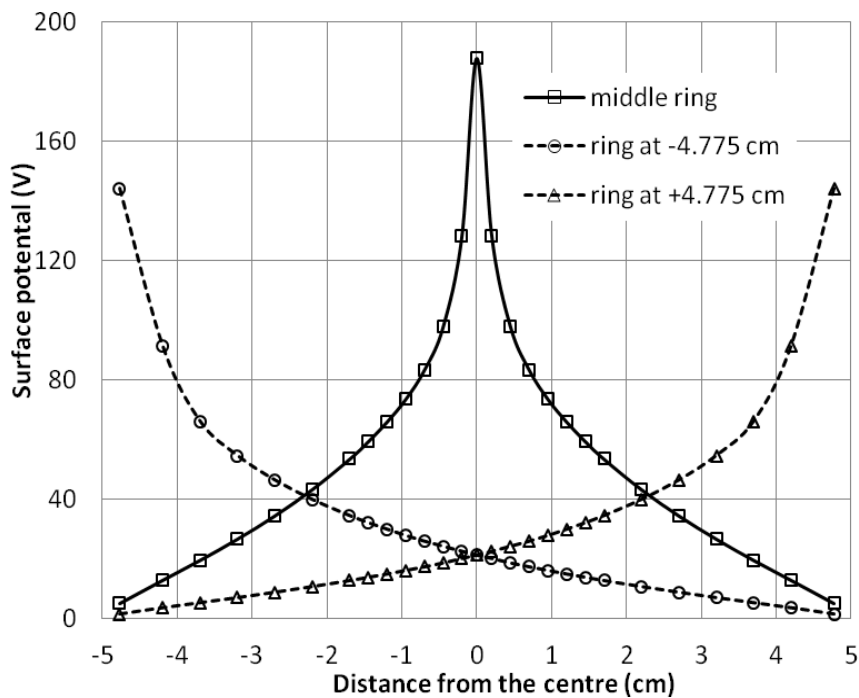


**Figure 5.4.** Calculated surface potential due to  $+1 \mu\text{C}/\text{m}^2$  assigned to a ring on the surface. The location of the charged ring is indicated in the legend.

## 5.3 Charging with corona belt

This section presents measured potential distributions and corresponding calculated charge density distributions when the insulator is charged by means of the corona belt. Each measurement was repeated at least three times and good repeatability was observed. Therefore, only the averaged distributions calculated out of those trials are presented here.

### 5.3.1 Effect of charging voltage

The surface potential distributions obtained with different charging dc voltage magnitudes (7 kV, 10 kV, 15 kV, 20 kV) for both positive and negative polarities are shown in Figure 5.5. For all the tests, the corona belt was located at the centre of the sample and the duration of voltage application was 2 min. It can be observed that at low charging voltages, 7 kV and 10 kV, the surface potential distributions had a bell shape for both polarities whereas for the higher voltage levels, 15 kV and 20 kV, the profiles changed to a saddle shape. Similar behavior has been observed in several other studies for flat samples [14, 42]. Charging by negative corona resulted in slightly higher surface potential values than that corresponding to positive charging. This could be due to the lower inception voltage of negative corona than of positive one. On the other hand, in case of positive charging, the increase of the charging voltage beyond 10 kV did not affect significantly the potential at the centre of the sample whereas for the negative polarity the potential on the entire surface was affected.

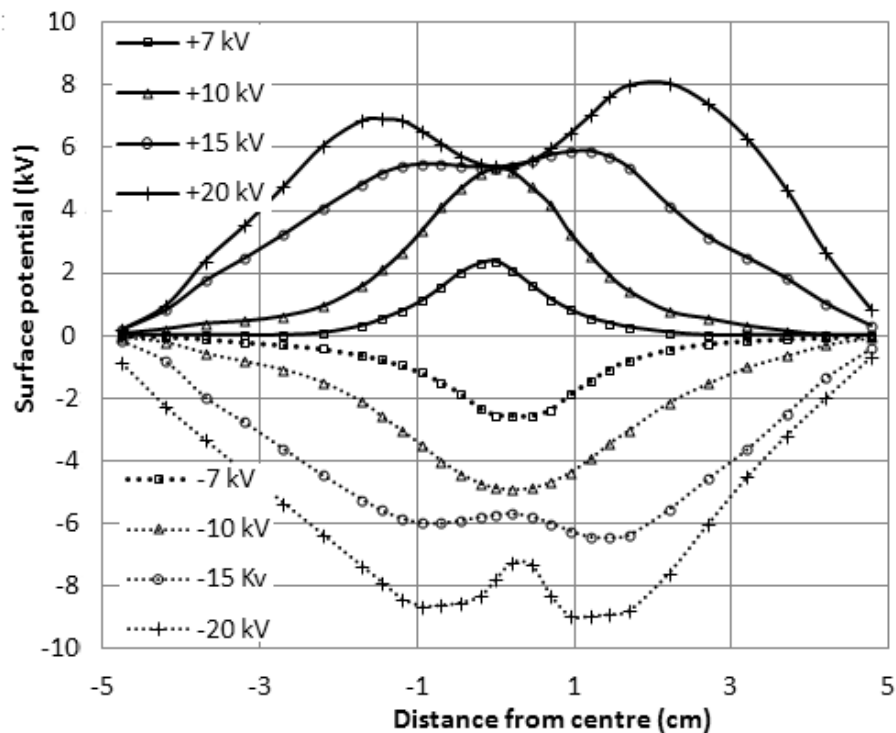


**Figure 5.5.** Measured surface potential distributions resulted from charging by the corona belt; the legend shows the charging voltages.

The reconstructed charge density distributions are shown in Figure 5.6 for  $\pm 10$  kV,  $\pm 15$  kV and  $\pm 20$  kV charging voltages. As it is seen, the charge density profiles in the middle of the insulator also have a saddle or bell shapes. In case of 20 kV charging, the saddle shape becomes more pronounced and charges having opposite polarity compared to that of the charging voltage (hetero-charges) accumulated at the central region. Appearance of bell or saddle shape with regards to the field strength is discussed separately at the end of this section. In the case of 10 kV, the charge spot having the same polarity as the charging voltage extends only for  $\sim 1$  cm from the centre whereas for the 15 kV and 20 kV, its expansion is much more pronounced (beyond 4 cm from the centre). In the regions close to the electrodes, an accumulation

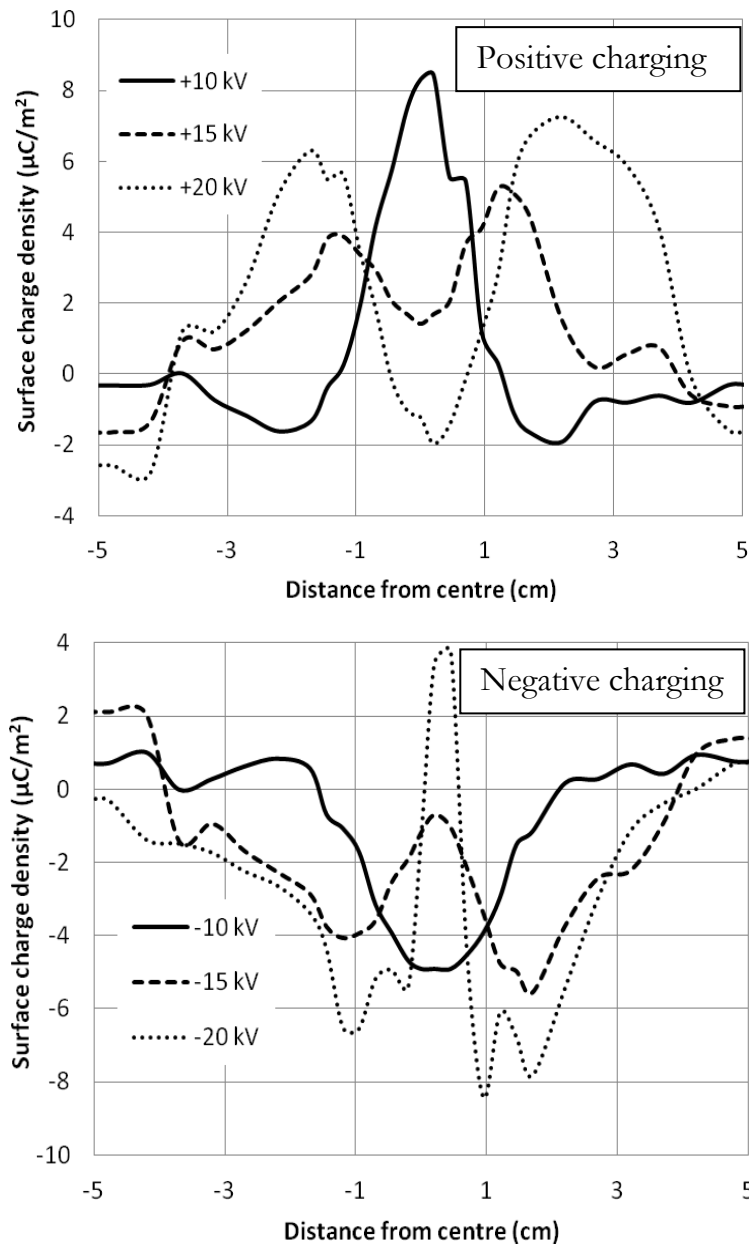


**Figure 5.6.** Calculated surface charge density distributions along the sample surface; legend shows the charging voltage applied to the corona belt.

of hetero-charges can be noticed. Similar observations were reported in other studies, e.g., [56, 100]. Reasons for appearance of these hetero-charges are not clear. However, among the responsible mechanisms one can consider; induction of image charges on the electrodes to compensate for those present in the middle of the insulator in order to keep the potential equal to zero, discharge activity at the triple junctions due to the field created by deposited charges and injection from the metallic electrodes when the field strength at the electrode is high enough.

The amount of charge deposited on the surface for each charging voltage calculated as a surface integral of the obtained charge densities is presented in Figure 5.7. Both the net charge (calculated by accounting for the polarity) and the homo-charge (charges having the same polarity as charging voltage) are shown. As one can observe, the former one increase linearly with the rising corona voltage for both the polarities and negative corona deposits a slightly higher amount of charges. At the same time, the amount of the homo-charge is independent on the polarity of the corona voltage, except for the case of 15 kV. The differences between the homo- and net charge magnitudes are attributed to the amount of hetero-charges, which may appears at the centre and/or closer to the electrodes.

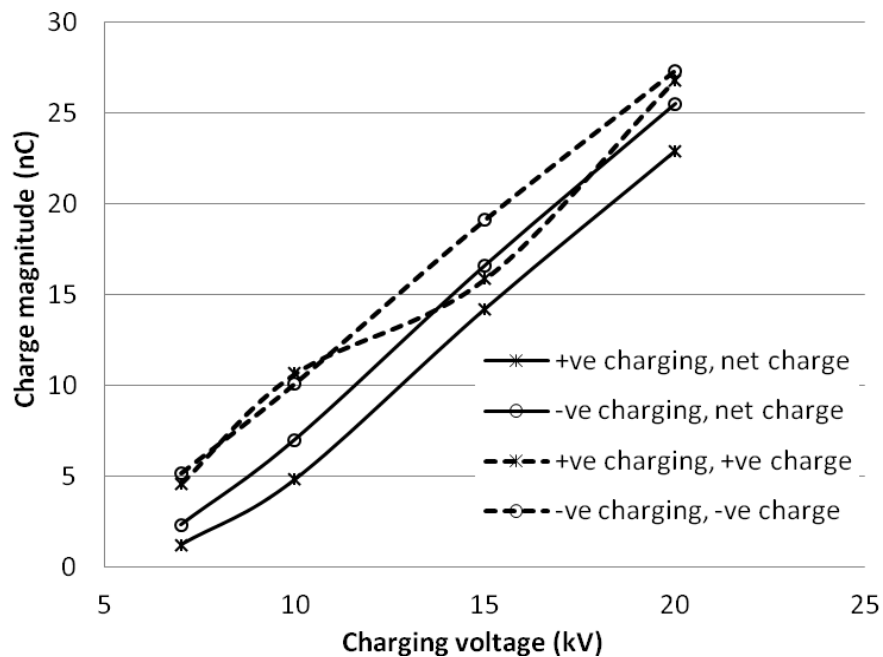
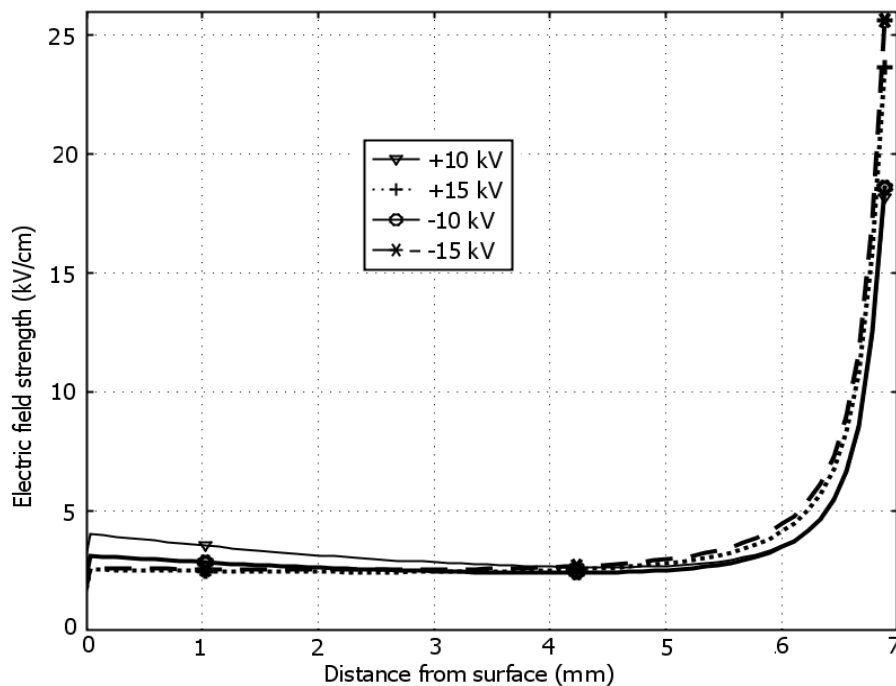


Figure 5.7. Calculated amount of charges on the surface.

## Back discharge

The saddle shaped profiles in both surface potentials and charge density patterns (Figures 5.5 and 5.6) may be related to back discharges between the charged surface and the needles after switching off the voltage supply. A primary requirement for such back discharges is a strong enough field at the needle tips. The field strength between the needles and the surface was evaluated by performing electrostatic calculations with the same model as described above for  $\Phi$ -matrix calculations. For this, the probe was replaced with grounded corona belt and the obtained surface charge density distributions were specified as boundary conditions. Figure 5.8 shows the field profiles created by charges deposited when  $\pm 10$  and  $\pm 15$  kV voltages were applied to the corona belt (corresponding charge distributions shown in Figure 5.6 were used). As one can observe, charges deposited by corona at  $\pm 10$  kV result in maximum field strength  $\sim 18$  kV/cm, which is below the ionization threshold of air ( $\sim 30$  kV/cm). Thus, back discharges cannot be initiated and surface potential and charge distributions appear to be bell-shaped (Figures 5.5 and 5.6). In the case of  $\pm 15$  kV charging voltage, the maximum field strength exceeds 25 kV/cm even with the reduced amount of charges in the central part of the insulator (Figure 5.6). The reasons for that are the much wider spread of charges (they are in general more evenly distributed over the whole surface) and field enhancements produced by the two peaks in charge density profiles. Taken into account that the field strength 25 kV/cm at  $\pm 15$  kV corresponds to already distorted distributions of surface charges, one can expect its higher magnitudes during deposition process which can trigger back discharges from the needles. These discharges partially neutralize the charges on the surface causing a



**Figure 5.8.** Magnitudes of the electric field strength between the surface (at zero coordinate) and the needle tip in presence of surface charges; the legend shows the charging voltages.

reduction of their density in the central part, i.e., forming the saddle-shaped profile. Due to this, the corresponding field drops to a level at which further discharge activities cannot be sustained.

### 5.3.2 Effect of charging time

The potential distributions obtained with different charging times are shown in Figure 5.9. In these tests, the corona belt was located at the centre of the insulator and the charging voltage was set to  $\pm 7$  kV. It can be clearly seen that the increase of the charging time from 1 min to 3 min does not significantly affect the resulting surface potential distributions for both negative and positive polarities. This may be due to the saturation of available surface states, which can contribute to the charge trapping, or termination of the corona discharges because of field reduction caused by the accumulated charges. Due to this observation all studies were carried out only with the charging time of 2 min.

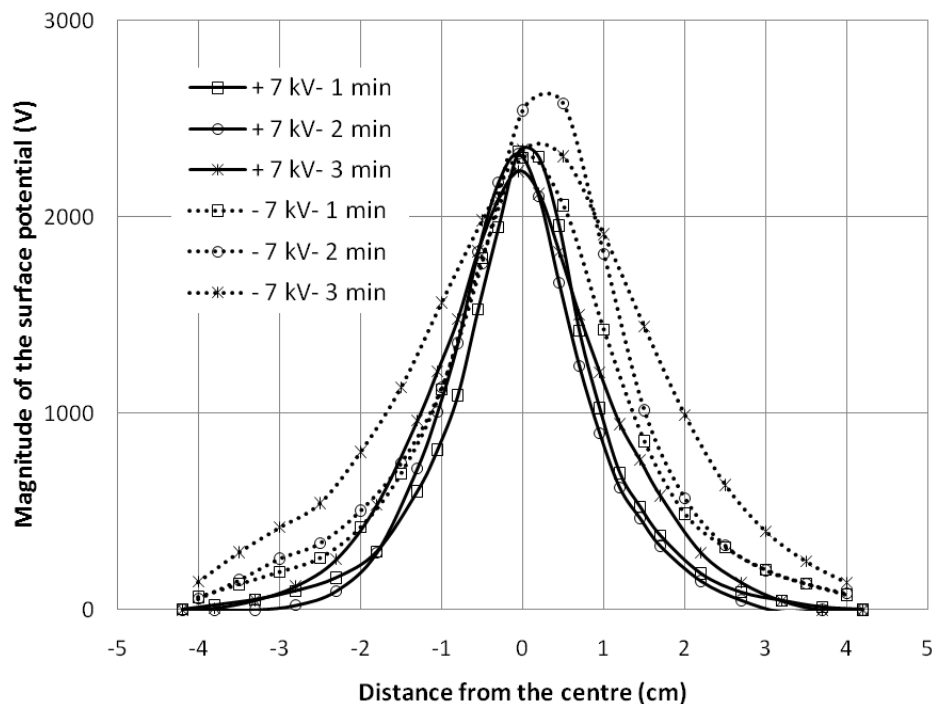


**Figure 5.9.** Measured surface potential distributions resulted from corona charging of different durations. The legend shows charging times.

### 5.3.3 Effect of position of the corona belt

The measured surface potential and charge density distributions for different positions of the corona belt are shown in Figures 5.10 and 5.11 respectively. Five locations with coordinates of -3 cm, -1 cm, 0 cm, 1 cm and 3 cm were considered. The charging voltage and duration were set to +7 kV and 2 min. It can be observed that the peak potential and, hence, the center of the charge spot is aligned with the belt location for all the cases. Even though the positioning of the probe at positive coordinates (i.e.,

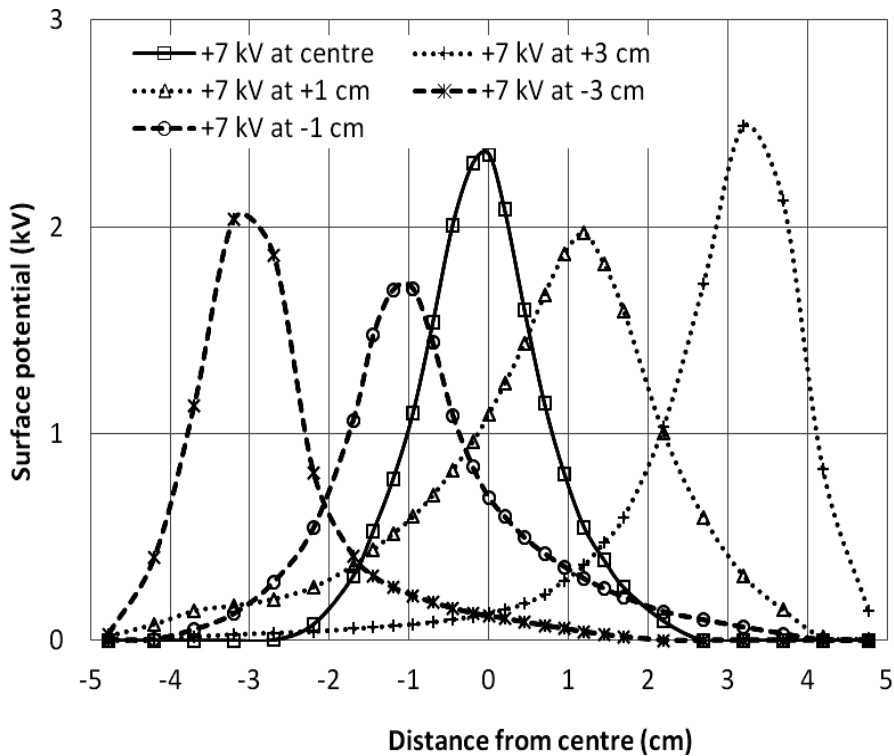


**Figure 5.10.** Measured surface potential distribution resulted from charging by the corona belt located at different positions; the legend shows the position coordinate; the charging voltage is +7 kV and charging time is 2 min.

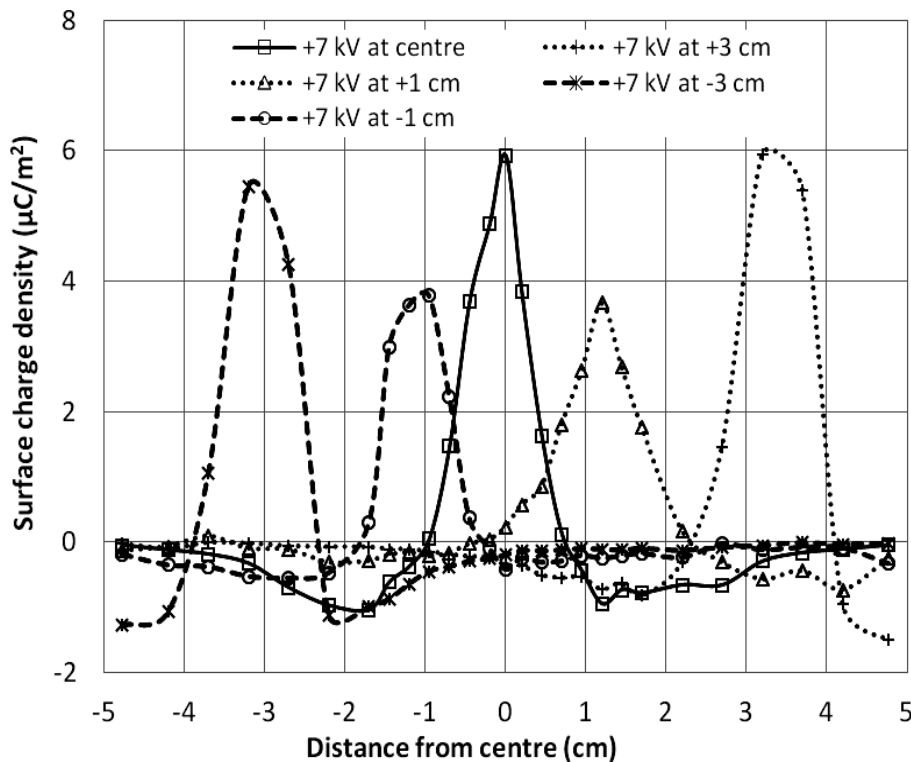


**Figure 5.11.** Calculated surface charge density distributions resulted from charging by the corona belt located at different positions.

closer to the permanently grounded electrode) results in slightly higher potentials than that at corresponding distances at the negative coordinates, the peak charge densities are very similar. Weak asymmetries among the curves corresponding to positive and negative belt positions may possibly be attributed to a presence of grounded objects nearby, which slightly distort the electrical symmetry of the electrode system, and also to the charge decay process during the time needed for scanning. Further, it can be observed that corona belt locations  $\pm 1$  cm result in lower surface potentials and, hence, lower densities of positive charges on the surface as compared to that at belt locations  $\pm 3$  cm. On the other hand, when the latter position was chosen, a slightly higher amount of positive charges was obtained as compared to the situation when the belt was located at the center. The net charge on the surface shows similar variations as for positive charges, however, its value remains at a fairly low level ( $< 3.5$  nC) for all the locations. For higher charging voltages, the behavior of the deposited charges is similar while the net charge densities are higher.

## 5.4 Charging by dc pre-stressing

Surface charging with pre-stressing was studied by applying a negative dc voltage to the high voltage electrode for 2 min. The voltage was increased to the desired dc level at a rate of  $\sim 0.8$  kV/s. Three different voltage magnitudes, -48 kV, -60 kV and -72 kV, corresponding to 60%, 75% and 90% of the flashover voltage were considered. The measured surface potential distributions and calculated charge density profiles are shown in Figures 5.12 and 5.13, respectively. Note that the negative potential was applied to the electrode at coordinate -5.1 cm and the electrode at +5.1 cm was kept grounded during charging while both the electrodes were grounded during the surface potential measurements. It can be observed that all the pre-stressing conditions result in an increase of the potential close to the electrodes. At the lowest voltage level, -48 kV, the magnitudes of the surface potentials at each end are almost equal and they vary linearly along the surface with polarity reversal taking place at the center. Corresponding charge density distributions show that the middle region remains practically uncharged whereas homo-charges (i.e. charges having the polarity of adjacent electrode) accumulate closer to the electrodes with slightly higher maximum density on the cathode side. The net charge accumulated on the surface is only +1 nC. The increase of the pre-stressing voltage up to -60 kV does not make significant changes in the surface potential or charge density profiles in the vicinity of the negative electrode whereas they increase slightly in the vicinity of the positive electrode. The net charge accumulated on the surface rises up to +7 nC in this case. Further increase of the voltage up to -72 kV leads to a significant increment of the surface potential on the anode side and the polarity reversal point is shifted towards the negative electrode. The peak of the negative surface potential is reduced as compared to that at lower pre-stressing levels. A significant portion of the insulator surface becomes positively charged and the magnitude of the resulting net charge is much higher (+28 nC) than that at the low stressing voltages. The reasons for the observed effect are not clear.

One may suggest that it can be caused by corona activities triggered from the edges of the metallic electrodes at -72 kV stressing voltage or can be conditioned by charges induced on the grounded electrode to compensate for the potential created by the surface charges. These hypotheses, however, require further investigations

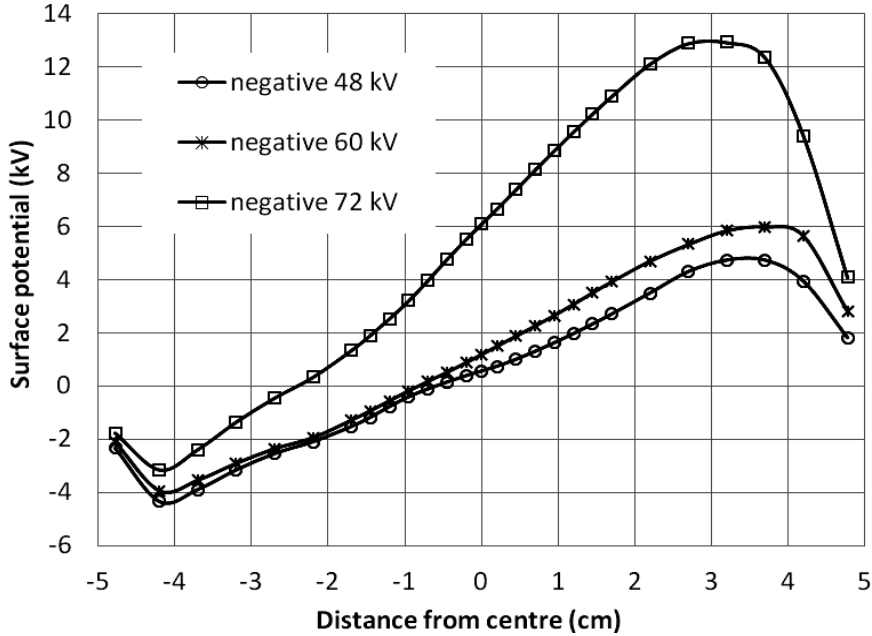


Figure 5.12. Measured surface potential distribution resulted from 2 min pre-stressing; the legend shows the magnitude of the applied voltage.

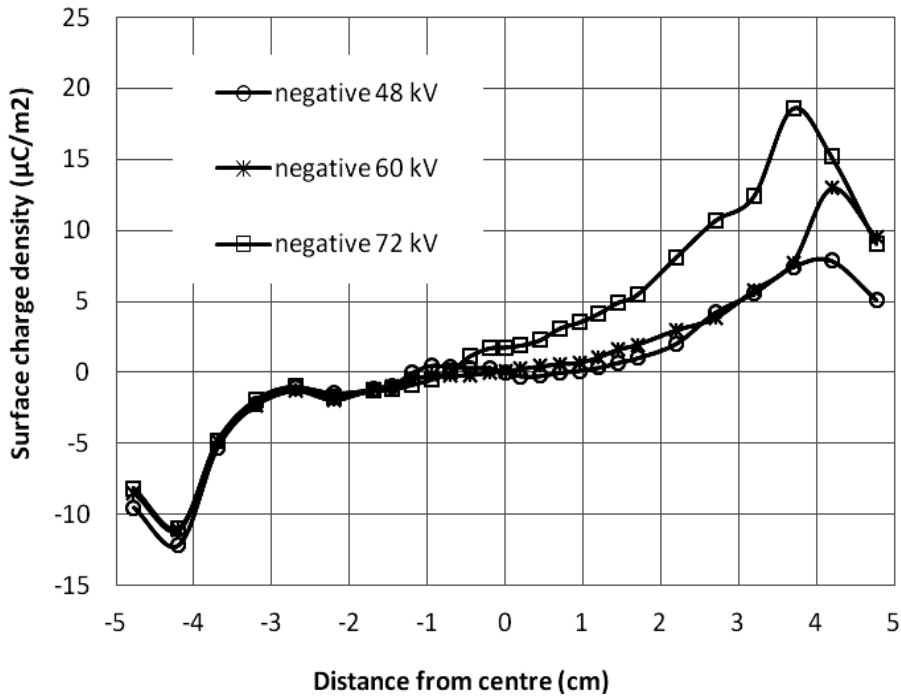


Figure 5.13. Calculated surface charge density distribution resulted from 2 min pre-stressing; the legend shows the magnitude of the applied voltage.

## **6 Impact of surface charging on dc flashover performance of insulators**

This chapter focuses on experimental and simulation studies carried out to investigate the effect of surface charging on flashover performance of a cylindrical composite model insulator. The experimental study aimed at obtaining dc flashover voltages in presence of surface charges while the presented computer simulations focused on developing a theoretical model for predicting flashover voltages. The performance of the model is validated by comparing the computed results with the experimental ones.

### **6.1 Measurements of flashover voltages**

In the experiments, the dc flashover voltages of a model insulator with pre-charged surface were measured. The insulator sample used for this study was identical to the one used for the charging experiments discussed in Chapter 5. Pre-charging of the insulator was also carried out with the same setup and conditions to insure that surface charge densities before flashover tests were similar to those presented in Chapter 5.

#### **6.1.1 Test procedure**

A procedure to conduct the dc flashover tests on polymeric insulators is not well established. General guidelines for dc withstand tests are given in [101] for testing of various components in HVDC systems. Time duration of the voltage application, its level, temporary overloading, etc. are specified and withstand performance is defined in terms of the duration of the voltage application. On the other hand, no mandatory IEC or IEEE ANSI standards are defined at present for dc flashover test procedure on polymeric insulators especially in terms of rates of rise of the applied voltage. However both the standards, IEC 60060-1 [102] and IEEE Std 4-1995 [103], recommend to use a rate of rise  $\sim 2\%$  of a withstand voltage per second during withstand tests. In case of a disruptive discharge test, it is recommended to use the

specific rate of rise defined for the test object under consideration [103]. However, as no specific rate corresponding to the polymeric insulators was found, the rate of test voltage rise for the model insulator used was set to  $\sim 0.8$  kV/s throughout all the experiments, which corresponded to  $\sim 1\%$  of the expected flashover voltage.

The testing procedure always began with cleaning the insulator surface with isopropanol for neutralizing residual charges deposited during sample preparation and handling. Upon allowing sufficient time for drying, a surface potential scan was made for checking that the surface had become charge free. After that the insulator was charged by dc corona for 2 minutes using the corona belt, as discussed in Chapter 5. Upon completion of the charging process, the corona belt was carefully removed and another dc generator capable to supply test voltage up to -100 kV was connected to one of the electrodes of the model insulator while the other electrode was kept grounded. One minute after completion of the charging, the dc generator was switched on and its output voltage was increased at the rate of 0.8 kV/s until a flashover took place. The corresponding flashover voltage was recorded and the procedure was repeated 10 times for each charging condition for getting a set of data for further statistical treatment. To determine the flashover voltage of an uncharged insulator, an extra test was carried out without charging the surface. All the experiments were conducted under indoor laboratory conditions, which were very close to the normal ones and resulted in atmospheric correction factors equal to unity.

### 6.1.2 Results of the measurements

Figure 6.1 shows the measured negative dc flashover voltages corresponding to six different surface charging conditions. The results are represented with the bars indicating maximum, minimum and average flashover voltage values. The amount of charges on the surface ( $x$ -axis) refers to the quantity obtained by integration of the averaged measured distributions shown in Chapter 5, Figure 5.6. In the integration, the hetero charges close to electrodes were neglected since they were assumed to be image charges (as discussed in Chapter 5) and were not produced by corona. At the same time, hetero charge appearing in the middle of the insulator surface (for example at charging voltage of 20 kV), was taken into account as it is directly associated with charging corona activities. Further, it was observed that the deviations in the total charge resulted from different charging events were within  $\pm 6\%$ . It can be seen in the figure that in case of uncharged surface (i.e. no charging was carried out after cleaning the surface with isopropanol), statistical variation of the flashover voltage is higher and lies between 80 kV and 100 kV with average flashover voltage of 87.5 kV. Charging of the surface results in much more narrow statistical variations as compared to that of the uncharged insulator. Even though an exact reason for this behavior is not clear, most probably it could be related to cleaning of the sample with isopropanol molecules which may screen out the existing surface charges. However once the material is subjected to charging after cleaning, this effect disappears. When analyzing the average value as well as the range of the variations of the flashover voltages, it is clear that

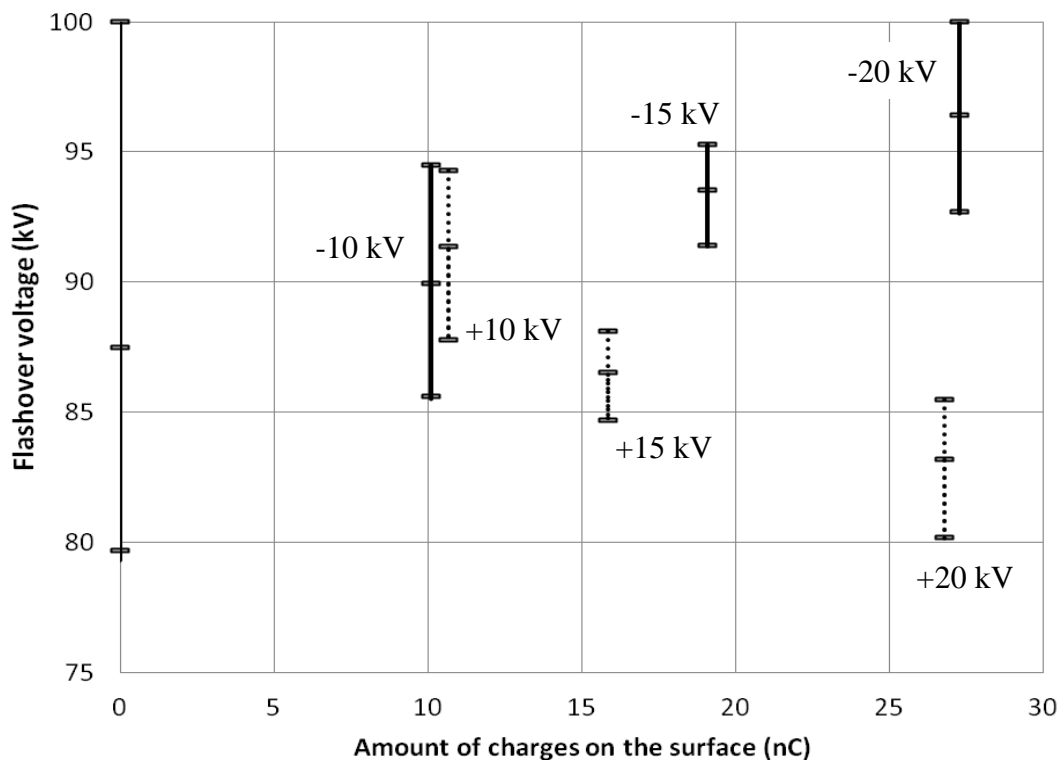


**Figure 6.1.** Measured negative dc flashover voltages; the bars indicate minimum, maximum and average values; the numbers at each bar indicate the charging voltage.

positive charging reduces the flashover voltage whereas negative charging increases it. It can be observed that the flashover voltages vary linearly with the amount of charges on the surface and the dependencies for different polarities are practically symmetric. Thus, charging with the voltage level of 20 kV, which resulted in the total charge of  $\sim 27$  nC on the surface, yields 7% increase of the flashover voltage as compared to the uncharged insulator in case of negative charging and in 6% reduction in case of positive charging. An analysis of these variations utilizing distributions of the electric field is presented in the next section.

## 6.2 Computational model

Determination of flashover voltages in the present study is based on adopting streamer breakdown criteria accounting for streamer inception, propagation and sustenance. Detailed discussion on the flashover criteria can be found in Section 2.3.2. The applied methodology consists of two main steps that include; (i) finding the electric field distribution between electrodes and defining a critical line (along which propagation of a streamer takes place), and (ii) evaluating the criteria for streamer development for the chosen path and field conditions. If either of these conditions is not fulfilled for a given applied voltage, the voltage is increased by a certain value and the whole

procedure is repeated again. The lowest voltage magnitude, at which all the criteria are satisfied, is considered here as a flashover voltage. Each of these steps is discussed in more detail below.

### 6.2.1 Calculations of electric fields

Accurate calculation of the electric field distribution is one of the most critical steps for obtaining precise results from the simulation. In general, a distribution of the electric potential  $V(x,y,z,t)$ , ( $x,y,z$  are spatial coordinates and  $t$  stands for time) in a system containing insulating materials can be found by solving Equation 6.1, which is essentially a current continuity condition.

$$\nabla \cdot (\sigma \nabla V) + \frac{\partial}{\partial t} \nabla \cdot (\epsilon \nabla V) = 0 \quad (6.1)$$

Here, the first term is associated with conductive properties of the material ( $\sigma$  is the conductivity) and the second term is related to the capacitive properties ( $\epsilon$  stands for the permittivity). It can be shown that in cases of rapidly varying voltages and/or highly resistive media, the capacitive term becomes dominating and the potential distribution is governed by Poisson's equation (Equation 6.2), which can be obtained directly from Gauss law.

$$-\nabla \cdot (\epsilon \nabla V) = \rho \quad (6.2)$$

Here,  $\rho$  represents space charge density.

Field calculations were carried out using Comsol Multiphysics software. The calculation process begins with representing the physical system in a computational domain. Then appropriate boundary conditions (including surface charge distributions) and material properties are introduced and a computational mesh is generated. After solving discretized Equation 6.1 or 6.2, electric potential and associated quantities can be obtained in any part of the computational domain.

### 6.2.2 Determination of the effective ionization coefficient

Once the field distribution is obtained, the next step is to determine the effective ionization coefficient along the critical line. Field dependencies of Townsend's ionization coefficient  $\alpha$  and the attachment coefficient  $\eta$  for dry air were adopted from [88] and were used for calculating the effective ionization coefficient  $\alpha' = \alpha - \eta$ . Figure 6.2 shows the variation of the ionization and attachment coefficients with the electric

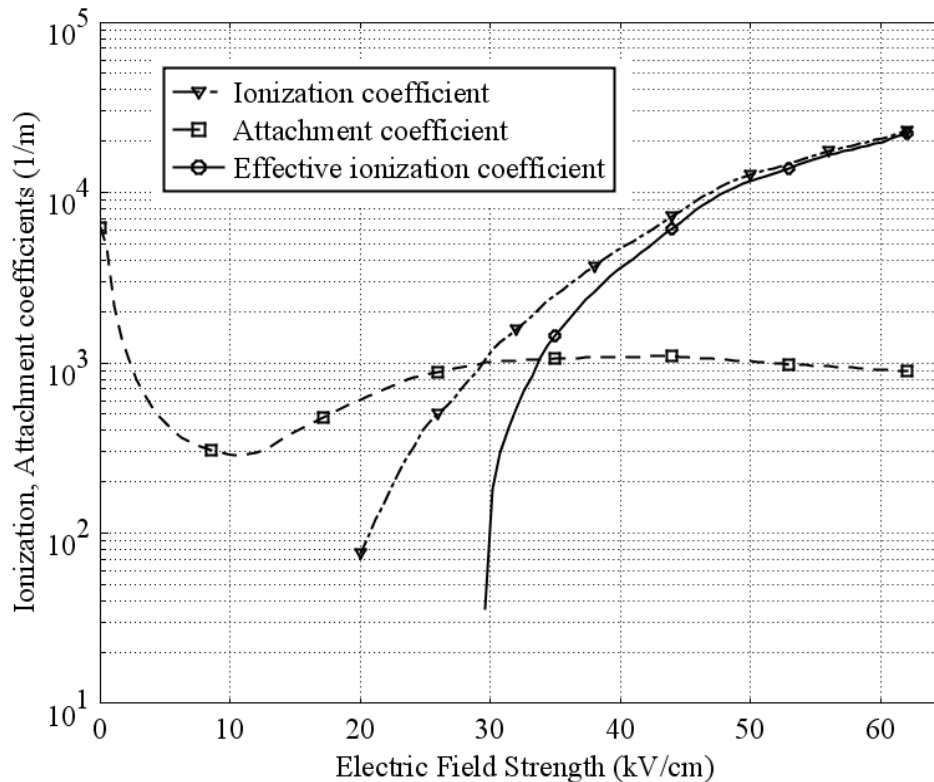


**Figure 6.2.** Variations of the ionization, attachment and effective ionization coefficients with electric field for dry air at atmospheric pressure [88].

field strength for dry air at atmospheric pressure 0.1 MPa and temperature of 25 °C. The integration of the effective ionization coefficient along the critical line in Equation 2.10 was performed utilizing trapezoidal integration rule.

## 6.3 Calculation of flashover voltage

### 6.3.1 Application of the model

Model validation with respect to dc flashover was based on the experimental results presented above in Section 6.1. For the computations, the experimental setup including the insulator and the grounded copper floor was represented in 3D computational domain as shown in Figure 6.3. The materials properties of the insulation system components were previously presented in Chapter 5. The boundary condition on one of the electrodes was set to the experimentally used ramped voltage with the rate  $\sim 0.8$  kV/s whereas the potential on the other electrode was set to zero. Preliminary results show that electric field distributions obtained by two different Equations 6.1 and 6.2 were exactly the same due to relatively low conductivity values of the dielectric media. Thus, the electrostatic application mode was used for further studies. It is worth mentioning that when using the charge density distributions presented in Chapter 5 as boundary conditions on the surface, only homo-charges (i.e. same polarity as the charging voltage) were considered by neglecting the hetero-charges closer to

electrodes. As already discussed in Chapter 5, those hetero-charges were not related to corona charging and appeared, most probably, as image charges.

After obtaining the field distributions, the next step is selecting a proper critical line. The calculated electric field distributions (analyzed below) show that even though the electrode arrangement is geometrically symmetric, it is not electrically symmetric due to presence of the grounded floor. This results in higher field strength closer to the energized electrode, which was the cathode in the experiments, as compared to the field strength at the grounded electrode. Thus, the ionization region is located closer to cathode and flashovers are assumed to be initiated by negative streamers. On the other hand, it was observed in the experiments that flashovers took place in air rather than along the surface. Thus, the line parallel to the top edge of the insulator passing through the point with the highest field strength on the cathode surface was selected as the critical line. One may note that due to different charge densities on the surface, the point having the highest field strength and, hence, the critical line may vary with charging conditions.

Upon selecting the critical line, the three criteria discussed in Section 2.3.2 were evaluated to calculate a flashover voltage. The value of  $K = 11.13$  was used for evaluating the ionization integral in Equation 2.10 (details about this choice are provided in Chapter 7). Note that in all the considered cases, the criteria for streamer propagation and sustenance were fulfilled at much lower voltage levels than that required for fulfillment of the inception criterion. Thus, the latter became the crucial factor deciding the magnitude of the flashover voltage.

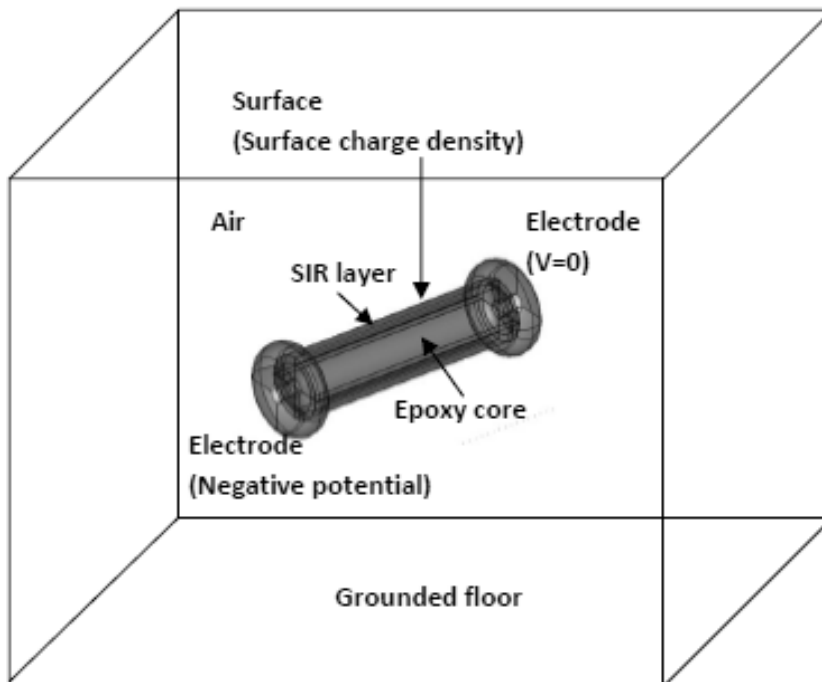
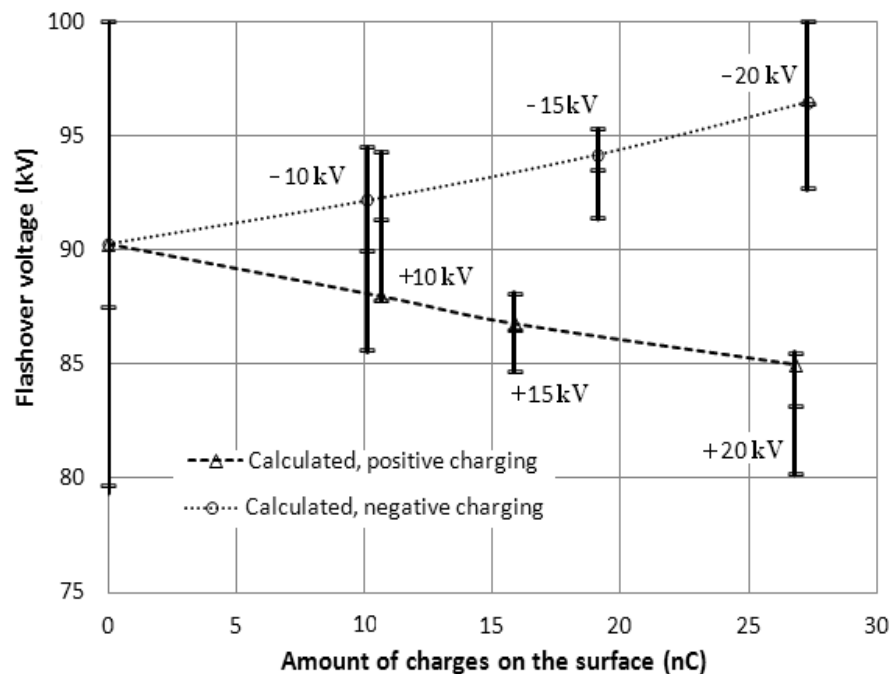


Figure 6.3. Schematic diagram of the computational domain.

### 6.3.2 Results and discussion

Figure 6.4 shows a comparison of the calculated negative dc flashover voltages with the experimental results presented above in Section 6.1. As it is seen, the calculated flashover voltages obtained for each of the charging conditions lie within the corresponding statistical variations of the measured flashover voltages demonstrating an agreement between the theoretical and experimental data. Moreover, one may notice that in case of negative charging, the model provides the results, which are very close to the averaged recorded flashover voltages.

As the mathematical model used for the prediction of flashover voltage was mainly based on calculations of the electric field strength along the critical line, the observed characteristics were further analyzed with the corresponding field distributions. The modifications of the field caused by surface charges can be recognized in Figure 6.5 where the field distributions corresponding to the voltage level of -90.3 kV (calculated flashover voltage of the uncharged insulator) are presented. The profiles are given for the tangential component of the electric field along the critical line for three different conditions of the insulator: uncharged and charged using corona belt with +20 kV and -20 kV. Note that in the figure, the high voltage electrode (the cathode in the experiments) is positioned at the coordinate -5.1 cm whereas the grounded electrode is at +5.1 cm. For all the cases, the critical line was located at 3 mm above the edge of the insulator surface. As already mentioned above, the non-symmetrical nature of the



**Figure 6.4.** Measured and calculated negative dc flashover voltages; bars corresponds to measured voltages whereas lines corresponds to calculated voltages; number adjacent to each bar indicate the charging voltage; legend is for calculated results.

electric field distribution is due to presence of the grounded floor in the vicinity of the electrode arrangement. It can be observed that deposited positive charges make the field in the cathode region stronger whereas its strength decreases in the anode region. The negative charging modifies the field in the opposite way, i.e., it becomes weaker at the cathode and enhances in anode region. Due to this behavior, the effect of the surface charges on the average electric field strength, which defines streamer propagation condition, is rather minimal. As mentioned before, the crucial factor in the calculations was the inception criterion, which is dependent on the field in the cathode region. According to Figure 6.5 (see inset), the modification of the electric field strength seems to be not so significant even at charging voltage of 20 kV. However, due to strong field dependence of the effective ionization coefficient (Figure 6.6), these small variations lead to significant changes in the magnitudes of the effective ionization coefficient and, hence, in the ionization integral (2.10). It can be observed in Figure 6.6 that positive charging results in the increase of the ionization coefficient as well as the size of the ionization region thus demanding lower voltage for the flashover. On the other hand negative charges reduce the ionization coefficient resulting in higher flashover voltages.

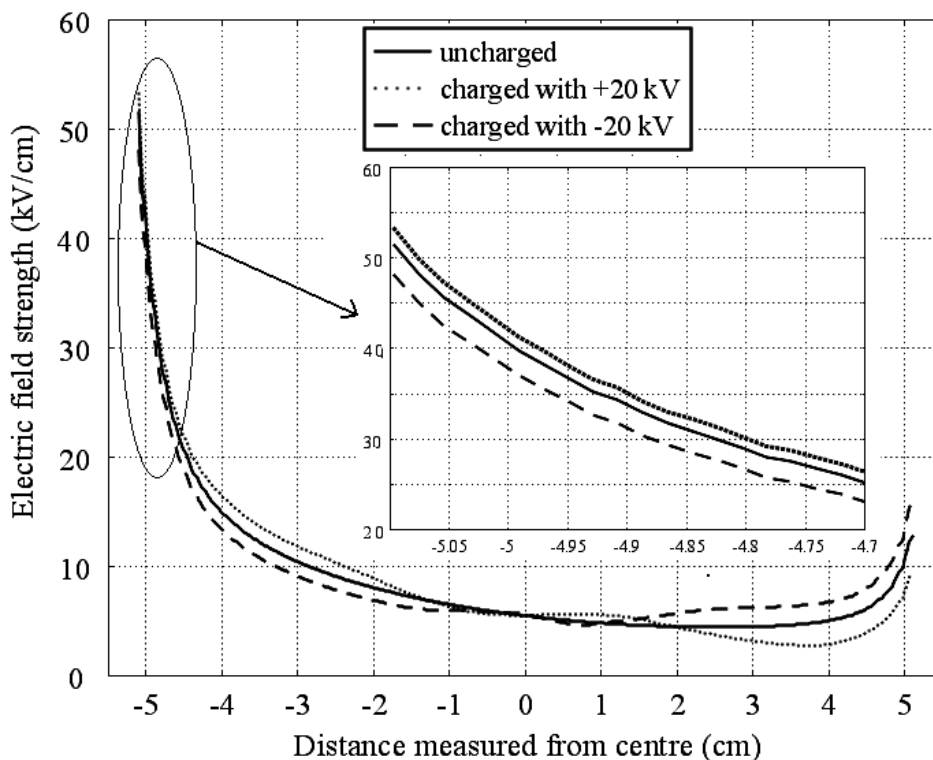


**Figure 6.5.** Calculated electric field strength along the critical line; the applied voltage is -90.3 kV; the distance measured from the centre of the critical line and positive direction is towards the grounded electrode. The inset shows the field in the cathode.

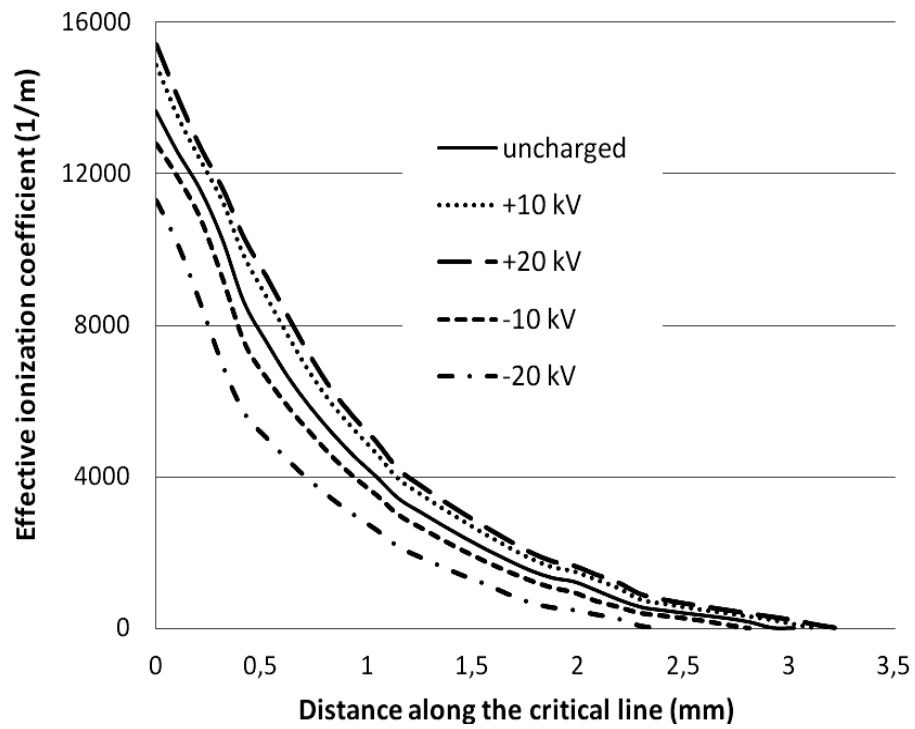


**Figure 6.6.** Variation of the effective ionization coefficient along the critical line; distance measured along the critical line starting from the cathode surface.



# 7 Prediction of impulse flashover performance of insulators in presence of surface charges

In this chapter the model discussed in Chapter 6 is further utilized to investigate possible changes imposed by a presence of surface charges on the impulse flashover voltage of a post insulator. First the model performance is validated by comparing the experimental results found in literature for flat insulation samples. Thereafter, the model is adapted to actual insulator geometry and effects of polarity, magnitude and location of surface charges as well as the influence of the insulator material on impulse flashover voltages are investigated.

## 7.1 Model validation

### 7.1.1 Application of the model

The model was validated by utilizing the experimental results presented in [4], where the experimental setup consisted of a 2 mm thick flat silicon rubber (SIR) sample and two identical brass electrodes placed on it at a distance of 50 mm, as shown in Figure 7.1. The electrodes were half cylindrical, 16 mm in diameter, with quarter spherical terminations. The SIR sample was supported by a plate of polymethylmethacrylate (PMMA) as additional insulation. Impulse voltages of 40/80  $\mu$ s duration of positive or negative polarities were applied to one of the electrodes whereas the other one was grounded. To investigate the influence of surface charges on impulse flashover voltages (IFV), they were pre-deposited on the SIR sample by means of corona from a needle electrode placed at 2 mm above the centre of the sample. The density of the deposited charges was estimated to be in the order of tens of  $\mu$ C/m<sup>2</sup>. The IFVs were measured for each voltage polarity and three different charging conditions: without charge, with positive and with negative deposited charges.

For the simulations, the experimental setup including the insulation sample and the grounded copper floor was represented in a 3D computational domain. Typical

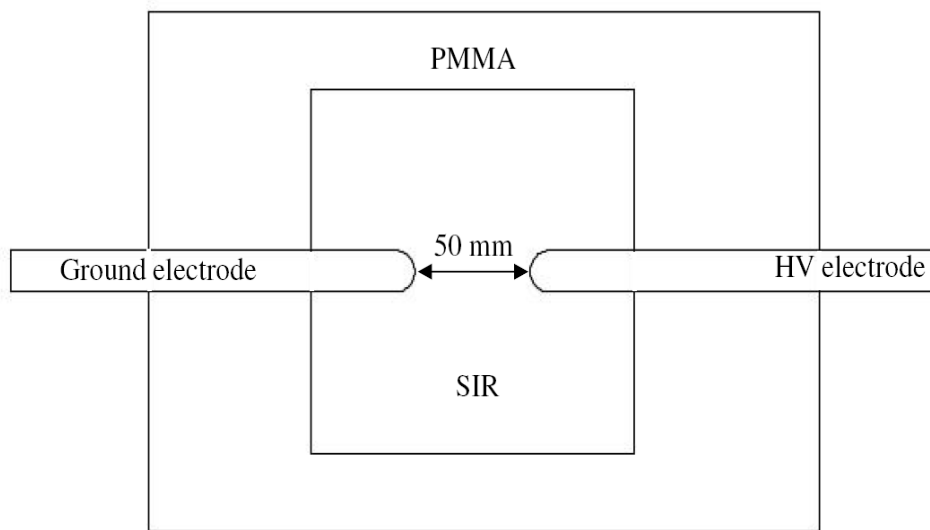


**Figure 7.1.** Top view of the experimental setup [4]; SIR sample placed on PMMA plate; half cylindrical brass electrodes placed on the sample are separated by 50 mm.

material properties (SIR:  $\epsilon_r = 3$ ,  $\sigma = 10^{-14}$  S/m, PMMA:  $\epsilon_r = 4$ ,  $\sigma = 10^{-16}$  S/m) suggested in [25] were used. The potential boundary condition on one of the electrode was set to the experimentally used impulse voltage whereas the potential on the other electrode was set to zero. Open boundaries, which were used to limit the size of the computational domain, were set to “Distributed capacitance” condition with appropriate parameters. First, field calculations for an uncharged insulator were performed by solving Equation 6.1. At the same time, the capacitive field distribution (Equation 6.2) for the same computational domain was calculated by solving the Laplace equation using electrostatic application mode. It was found that the electric field profiles obtained by the two different application modes were exactly the same due to rapidly varying impulse voltage and high resistivities of the materials. Thus, the electrostatic application mode was adopted in further calculations due to provided possibility of direct implementation of “Surface charge” boundary condition.

After analyzing the computed field distributions, the highest field strength were found along the line between the tips of the electrodes on the SIR surface and this line was selected as the critical line for further calculations. An example of the electric field distribution along the critical line is shown in Figure 7.2. Two high field regions near the electrodes could be identified on this line due to symmetrical arrangement of the setup. One may note that the electrode arrangement was placed far away from the grounded surface representing the floor of the lab and the simulations showed that in this case it had negligible effect on the field distribution along the critical line. Depending upon the conditions, one also might expect that the field magnitude in the middle of the gap could become lower than the ionization level providing  $\alpha' < 0$  and, hence, it is necessary to define in which region the ionization integral  $K$  (Equation 2.10) needs to be evaluated. In this respect, an important factor seems to be the polarity of the potential on the electrodes. As it is known from gas discharge theory, a cathode

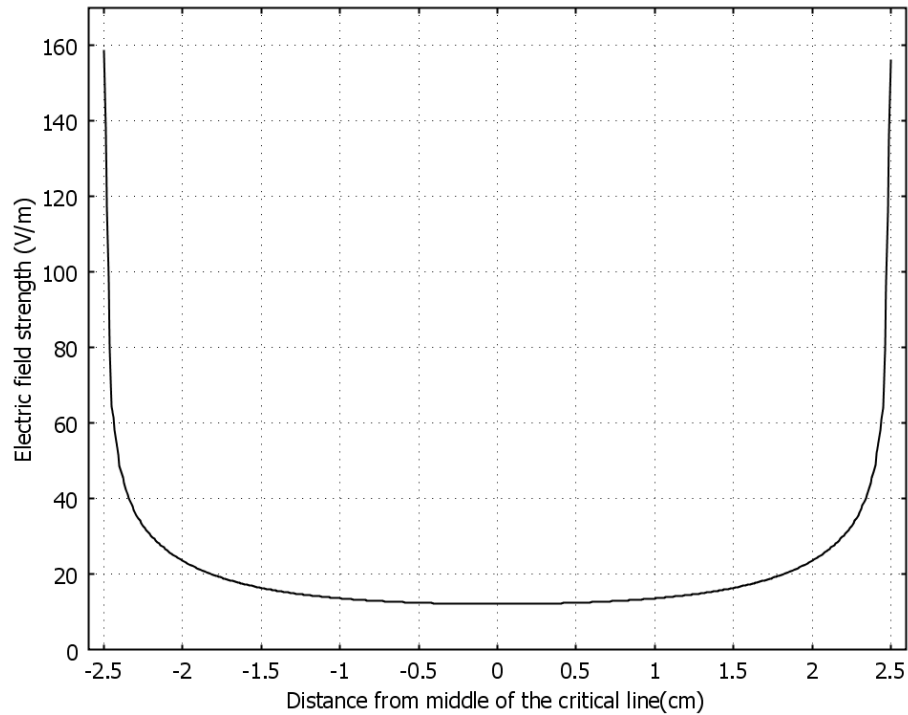


**Figure 7.2.** Electric field distribution along the critical line. Electrode at the coordinate +2.5 cm was supplied with 1 V whereas the other one kept grounded.

plays an important role in initiation and development of an electron avalanche (which is a predecessor of a streamer) by supplying seed electrons due to photo-effect and other secondary processes which sustain discharge development [86]. Hence, one may expect that discharge activity is concentrated mostly in the cathode region rather than at the anode when the applied field becomes high enough. Thus, it was assumed in this study that the discharge process in the considered system is initiated with a primary avalanche formed in the cathode region and it can be eventually transformed into a streamer crossing the gap. This hypothesis was confirmed by comparing the results of the integration for different regions, which showed that its application in the anode region did not yield the experimentally observed increment of IFVs due to the presence of negative charges. Therefore, the flashover criteria were evaluated on the cathode side of the gap for all the experimental conditions discussed below.

### 7.1.2 Comparison of the results

The results of the calculations together with corresponding experimental data are shown in Table 7.1. The experimentally obtained IFVs for cases 1 and 2 were utilized for adjusting model parameters. Thus, the calculations started by implementing case 1 (positive voltage polarity, no deposited charges) and the magnitude of  $K$  was adjusted in such a way that the computed flashover voltage was exactly the same as the measured one, i.e. 58.9 kV. The obtained value of  $K = 11.13$  was found to be within the typical range 9.15-18 [104]. Further, parameters of the deposited surface charges needed to be adjusted. In the present study, a bell-shaped surface charge profile was assumed and represented as Gaussian distribution.

**Table 7.1.** Experimental [4] and calculated values of impulse flashover voltages.

Polarity of the applied voltage	Case	Deposited charge	Flashover voltage (kV)	
			Measured	Calculated
Positive	1	No charge	58.9	58.9*
	2	Positive	56.1	56.1**
	3	Negative	63.8	61.7
Negative	4	No charge	-57.9	-58.9
	5	Positive	-55.9	-56.1
	6	Negative	-60.2	-61.7

\* Used to adjust constant  $K$ , \*\* to find a value for  $Q_{max}$  in Equation 7.1.

$$\rho = Q_{max} \cdot \exp\left(\frac{-(x - x_i)^2 - (y - y_i)^2}{2\sigma_{st}^2}\right) \quad (7.1)$$

Here,  $\rho$  stands for the magnitude of the surface charge density;  $Q_{max}$  is the maximum charge density;  $x$  and  $y$  are coordinates;  $x_i$  and  $y_i$  are the coordinates of the location of the maximum of the charge density distribution. The standard deviation  $\sigma_{st}$  was set to 5 mm. The magnitude of the maximum charge density  $Q_{max}$  in the calculations was adjusted using experimental data for case 2 in Table 7.1 (i.e., positive applied impulse voltage and positive pre-deposited charges) as a reference. The value of the IFV equal to the measured one was calculated with  $Q_{max} = 11.4 \mu\text{C}/\text{m}^2$  that agrees well with the experimental observation [4] where the charge density was evaluated to be in the order of ten of  $\mu\text{C}/\text{m}^2$ . Finally, the flashover voltages for the other cases (3, 5 and 6) were computed with the obtained values for  $K$  and  $Q_{max}$ . As it can be observed, the calculated IFVs are in agreement with the experimental results. The maximum difference between the simulated and experimental values is found for case 3 and the error is about 3.3%. Note that since the geometry of the experimental setup is symmetric, it is obvious that the calculated IFVs values are not dependent on the polarity of the applied impulse voltage. It is important to stress here that the agreement between the calculated and measured magnitudes of the flashover voltages revealed the validity of the approach used, in particular, the way the integration (2.10) was performed. Thus for the considered system, the acceptable level of errors  $\sim 3\%$  was achieved when the integration was done in the vicinity of the cathode. Otherwise, deviations larger than 10% were observed.

## 7.2 Model detail

The developed model was further utilized for analyzing the effect of pre-deposited charges on impulse flashover voltages of a 35 kV post insulator model. To analyze the proximity effect of an external grounded surface in the simulation, two extreme cases for the location of such surface were considered: (a) a ground plane far away from the insulator (infinite distance to ground or “without” ground), and (b) the insulator stands on the grounded plane, providing that one of its flanges is in direct contact with it. In case (a), the electric field distribution becomes symmetric, making it sufficient to consider the applied impulse voltage of one polarity only. Opposite, for the case (b), both polarities of the applied impulse need to be considered due to the unsymmetrical field distributions.

### 7.2.1 Field calculations

Similarly to the procedure used for the model validation, computations started with field calculations. A cylindrical insulator without sheds of diameter 140 mm and height of 440 mm (corresponding to the dimensions of a 35 kV post insulator) was considered. For the computations, rotational symmetry of the insulator was utilized and its geometry was represented in 2D computational domain as shown in Figure 7.3. The selected material properties of the insulation system components are listed in Table 7.2. The field distributions corresponding to 50 kV positive impulse voltage (40/80  $\mu$ s) attained with Equations 6.1 and 6.2 are shown in Figure 7.4. The field profiles are provided for the time instant of 30  $\mu$ s, which is in the front of the applied impulse. One set of the curves is for the field magnitude along the surface of the insulator, whereas the other represents the distribution along line 1 in Figure 7.3, which represents the shortest path connecting the points with maximum field intensity on each electrode and it is located in air 30 mm away from the insulator surface. It can be observed that the effect of conductivity on the field distributions is negligible under rapidly varying impulse voltages and high materials resistivities, which allows for using the electrostatic approach similar to previous studies related to model validations.

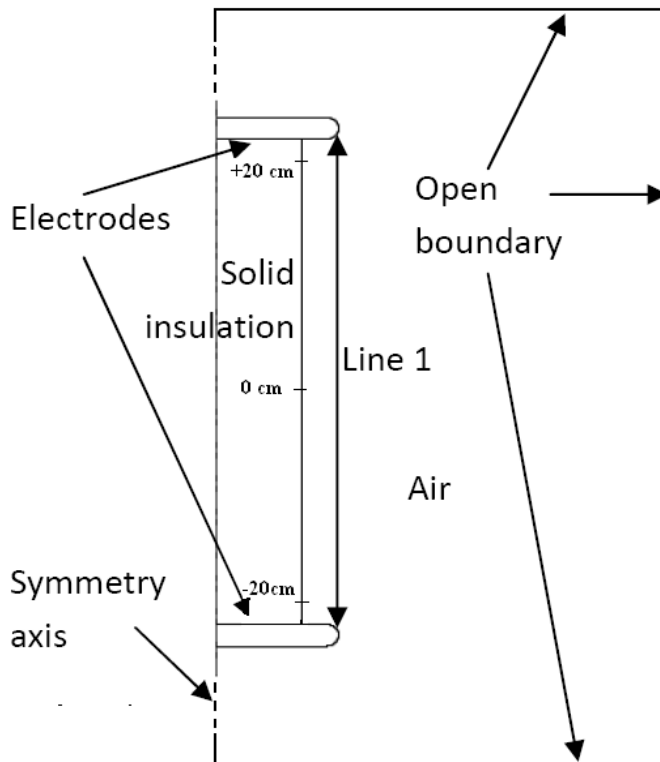


**Figure 7.3.** Model geometry. Solid insulation: cylinder 140 mm diameter, 440 mm height. Electrodes: maximum diameter 200 mm, 20 mm height.

**Table 7.2.** Material properties used in the model [27].

Material	Parameter	Value
Air	Relative permittivity	1
	Conductivity, $(\Omega\text{m})^{-1}$	$10^{-15}$
Solid insulation	Relative permittivity	2.3
	Conductivity, $(\Omega\text{m})^{-1}$	$10^{-14}$

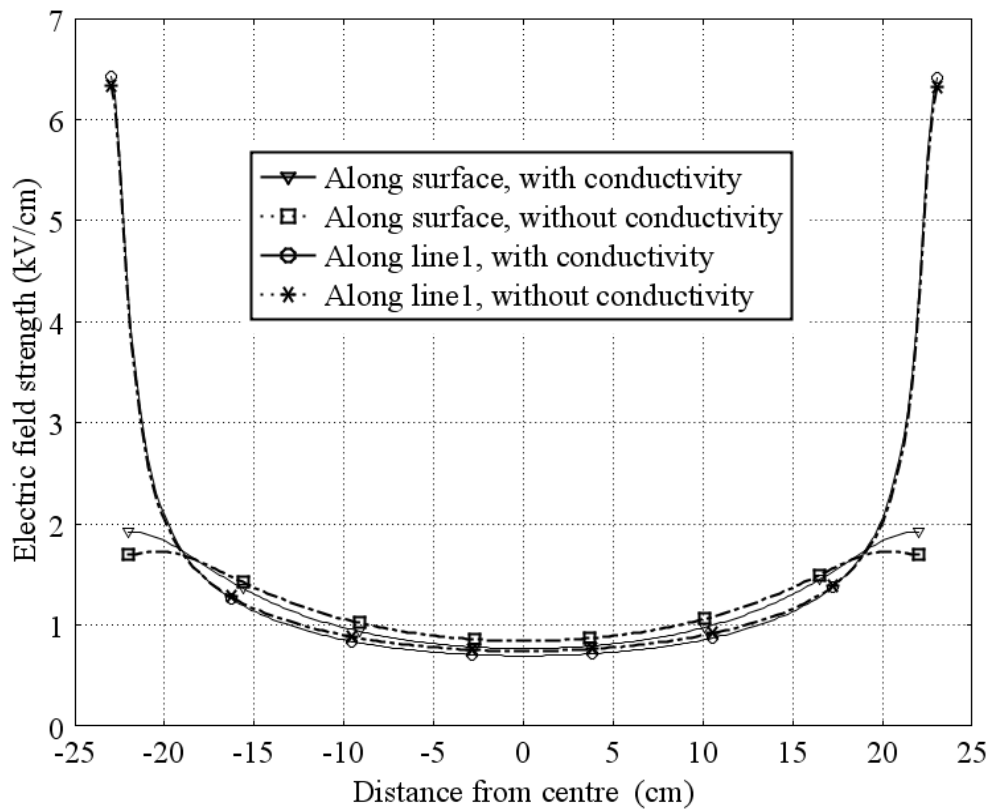


**Figure 7.4.** Magnitude of the electric field strength along insulator surface and along line 1 as shown in Figure 7.3. The profiles were obtained either accounting for the conductivities of the materials (Equation 6.1) or neglecting them (Equation 6.2) as indicated in the legend.

### 7.2.2 Study cases

Three cases were considered. Case 1 was implemented by assigning positive potential to the upper electrode shown in Figure 7.3 while the lower electrode was grounded. Similarly to the procedure used for the model validation with impulse flashovers, it was assumed that discharges were initiated at the cathode and the flashover criteria were evaluated in the cathode region.

In cases 2 and 3, the bottom electrode was placed on the grounded plane and, correspondingly, the impulse voltage, positive and negative respectively, was applied to the upper electrode. Here, despite the field distributions were unsymmetrical, the high field region was always located closer to the upper electrode. Hence, depending upon the polarity of the applied voltage, the flashover criteria were evaluated in the anode region for case 2 and in the cathode region for case 3.

For all the cases 1-3, the line 1 shown in Figure 7.3 was considered as a critical line. Such choice seems to be acceptable as the calculated length of the critical region  $x_c$  in Equation 2.10 are in the range of 7-10 mm, i.e. the ionization zone is limited to the

close vicinity of the electrode providing the strongest field. In the rest of the gap, the average field condition (propagation criterion) plays a major role and the error introduced by averaging the field strength along different probable streamer trajectories is not significant, at least for the length of the insulator (440 mm) used here.

### 7.2.3 Surface charges and parametric study

In order to perform the simulations in the simplified 2D geometry, a belt-like surface charge distribution on the insulator surface is assumed similar to that discussed in Chapter 5. Such a distribution can be generated due to corona from a wire loop around the insulator (corona ring) or from its flanges. In the model, the belt like shape was represented by a Gaussian-type distribution with a standard deviation of 5 mm (similarly to the model validation in Section 7.1). Parametric studies were carried out by varying charge magnitudes as well as its location on the surface. The influence of solid material permittivity was also investigated. It is necessary to mention here that for proper identification of the influence of surface charges on IFVs, the maximum surface charge density was varied in a wide range of  $Q_{max} = 0-75 \mu\text{C}/\text{m}^2$  (absolute). The upper bound was selected so that the field created by the charge does not exceed the field strength of 30 kV/cm for avoiding so-called back discharges. Field calculations performed using the model described above in Section 7.1 showed that this limit was about  $85 \mu\text{C}/\text{m}^2$  for the considered electrode system and charge distributions.

## 7.3 Results

### 7.3.1 Effect of charge magnitude

A set of simulations was carried out with different polarities and magnitudes of the charges located at the centre of the insulator surface for the three study cases. The results of the calculations are shown in Figure 7.5. One can observe that the presence of surface charge can result in an increase or a decrease of flashover voltages depending on the polarity of the deposited charge and field condition similar to that obtained for dc flashover voltages (see Section 6.1.2). In the case without ground effect (case 1, solid lines), the positive surface charge leads to a reduction of IFVs, whereas the presence of negative charge increases them. The variation of IFVs with charge density is linear for the negative deposited charges whereas for positive charges the linear behavior is only seen up to a charge density of  $25 \mu\text{C}/\text{m}^2$ . At higher densities, a non-linear decrement of IFVs is observed (it is further discussed in the following section). For the case with the insulator mounted on a grounded surface and positive applied voltage (case 2, dotted lines), the levels of IFVs are obtained to be much lower and the effect of charge polarity is opposite, i.e. the positive charges leads to increased IFVs, while the negative charges decrease IFVs. Here, the variation of the flashover

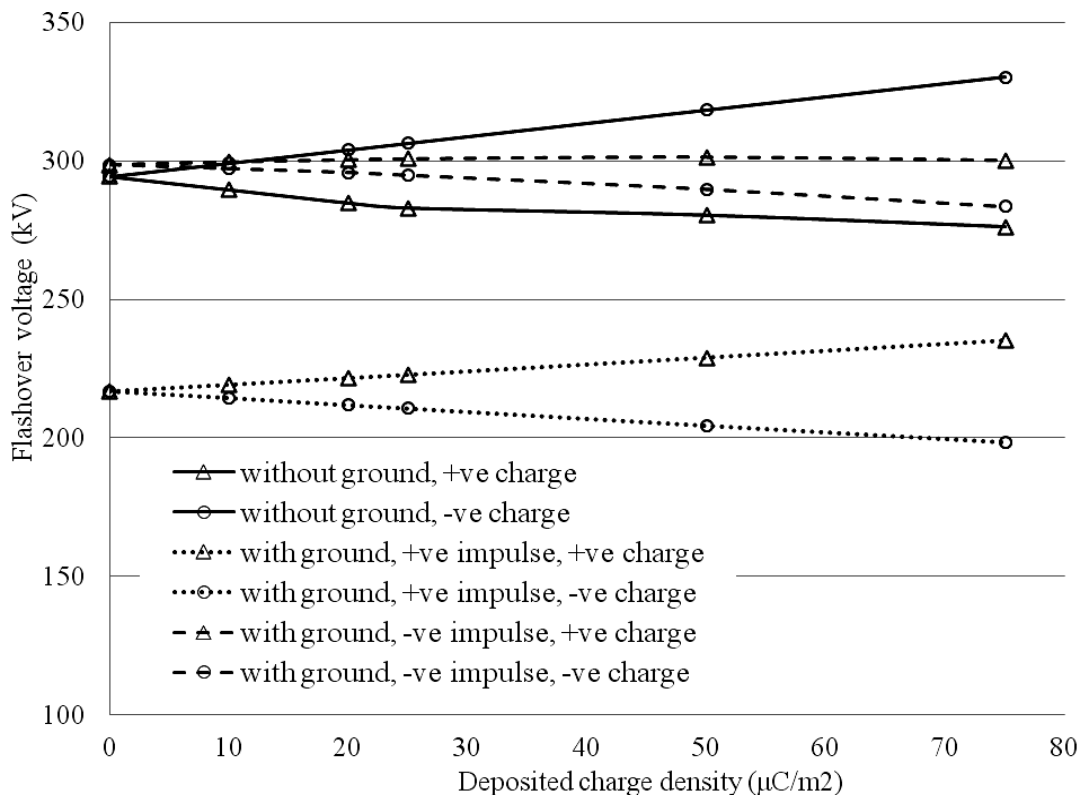


**Figure 7.5.** Variations of the flashover voltages with the magnitude of the pre-deposited charges  $Q_{max}$ ; belt-like surface charges are located at the centre of insulator surface; polarity of the deposited charge is mentioned in the legend.

voltages with the charge magnitude is linear for both positive and negative polarities of the deposited charges. For similar arrangement and negative applied impulse (case 3, dashed lines), the negative deposited charges slightly reduce the flashover voltages whereas the effect of positive charge is negligible. The observed variations of IFVs are non-linear irrespectively of surface charge polarity.

The relative changes in the obtained IFV values due to the presence of a charge belt with  $Q_{max} = 75 \mu\text{C}/\text{m}^2$  (in relation to IFVs without any surface charges) are shown in Table 7.3 for all the three cases. The results of the simulations indicate that cases 1 and 2 show stronger variations of IFVs than case 3. At the same time, the case with proximity to ground and positive applied impulse (case 2) is characterized by lower level of IFVs as compared to case 3 (ground and negative impulse). Even without any surface charges, the IFV for case 2 is 27% lower than for case 3, reflecting the difference in streamer propagation (averaged field) conditions. Thus, case 2 seems to be critical for the considered insulator arrangement (with ground) from the breakdown point of view.

**Table 7.3.** Variations of IFVs due to presence of charge  $75 \mu\text{C}/\text{m}^2$ .

Polarity of the charges	positive			negative		
Case	1	2	3	1	2	3
Change of IFV in % w.r.t. no charge	-6.2	8.5	0.5	12.2	-8.5	-5.0

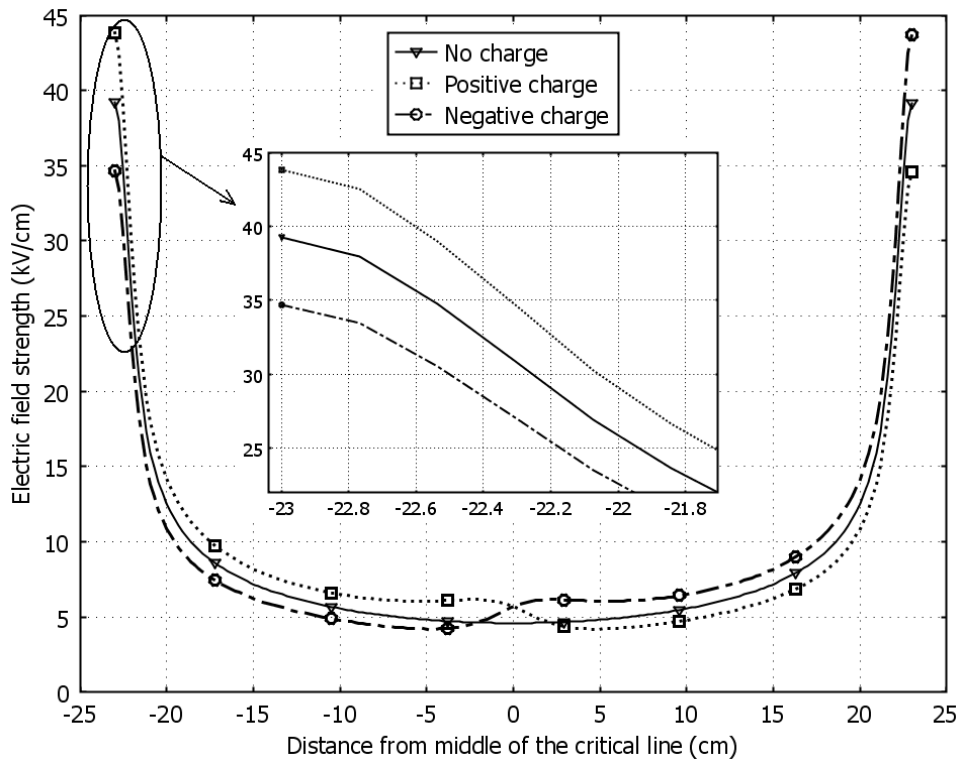


**Figure 7.6.** Magnitude of the electric field strength along the critical line for case 1 at 300 kV. The charge density  $Q_{max} = 75 \mu\text{C}/\text{m}^2$ . The inset shows the fields in the cathode region.

### Discussion on case 1

The behavior of IFVs can be correlated with the variations of the electric field distributions along the critical line. The field profile for case 1 is shown in Figure 7.6. One can observe that the original (without any deposited charges) electric field distribution is symmetric, i.e. the field strengths in both the anode and cathode regions are of the same magnitudes and slightly exceed the ionization level of  $\sim 30 \text{ kV}/\text{cm}$  (this corresponds to the crossing point of the field dependencies of the ionization and attachment coefficients in Figure 6.2). Deposition of positive charges leads to the field enhancement in the cathode region up to  $44 \text{ kV}/\text{cm}$  (see the inset) and its reduction at the anode. This results in a more intensive ionization in a larger volume at the cathode,

where streamer inception criterion is evaluated, thus resulting in lower IFVs. The non-linearity of the flashover characteristics observed in Figure 7.5 for this case with high positive charge densities ( $>25 \mu\text{C}/\text{m}^2$ ) comes from the fact that the streamer inception condition (i.e. ionization integration) is satisfied due to the strong field at the cathode while the average field in the gap is lower than the one needed to support streamer propagation. Hence, an increase of the applied voltage is required to fulfill both criteria and the resulting flashover characteristic deviates from linear behavior.

The situation is opposite for negative deposited charges. The field near the cathode becomes lower in presence of the surface charge, whereas it enhances at the anode. Following the hypotheses of flashover initiation in the cathode region as discussed in Section 7.1, the streamer inception criterion was evaluated at the cathode side, where the field becomes lower due to negative charges resulting in higher IFVs. The required rise of the applied voltage causes the criterion for the average field to be always fulfilled when inception criterion is satisfied and, thus, linear characteristics are observed in Figure 7.5.

### **Discussion on case 2**

The observed variations of IFVs for case 2 can also be explained with help of the field distributions along the critical line shown in Figure 7.7. In contrast to case 1, the field profiles are unsymmetrical to proximity of the grounded surface and only one ionization zone at the anode exists, where the ionization integral is evaluated. One can observe in the figure that the presence of positive charge leads to the enhancement of the field in the cathode region and its reduction at the anode while negative charge affects the distribution in opposite way. This explains the polarity effect observed in Figure 7.5. Note also the linear behavior of the characteristics which is due to the fact that the streamer propagation condition is always fulfilled when the inception criterion is satisfied.

### **Discussion on case 3**

The difference between cases 3 and 2 is only the polarity of the applied impulse to the non-grounded electrode, thus giving the same field distributions along the critical line. However in case 3, the high field region is associated with the cathode and flashover is due to negative streamers, which require higher averaged field along the discharge path as discussed in Chapter 2. For all considered charge magnitudes, the ionization integral is satisfied at a lower voltage than the voltage needed to fulfill the average field (propagation) criterion. Thus the average field requirement becomes a critical condition. The negative charges increase the average field and reduce the IFVs as shown in Figure 7.5 (dashed line). In the case of positive charges there is no significant change in the average field and, hence, in the computed IFVs.

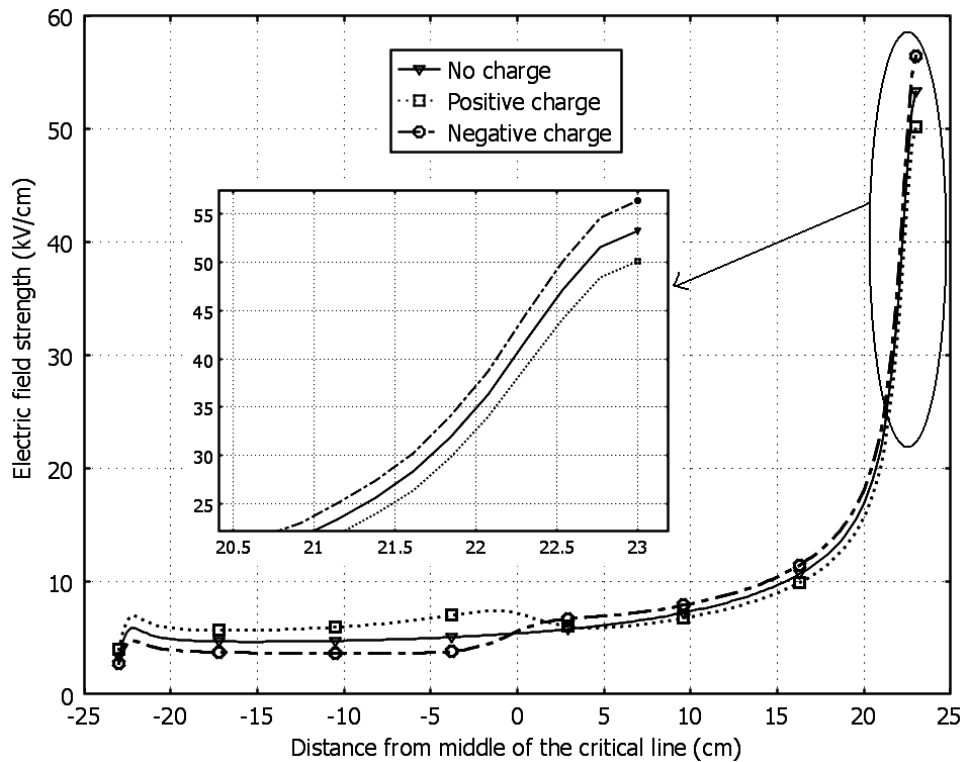


**Figure 7.7.** Magnitude of the electric field strength along the critical line for case 2; the voltage is 300 kV and  $Q_{max} = 75 \mu\text{C}/\text{m}^2$ . The inset shows field distributions in the anode region.

## Experimental evidences

The above presented variations of the impulse flashover voltages agree, in general, with the previously reported behavior [3-7, 66] (discussed in Chapter 2). One should note, however, that the reported data were obtained for electrode configurations different to the one considered here, but still allowing for qualitative comparisons. Thus in [6, 7, 66], where flashovers were triggered from the anode side using protrusion or needle, a presence of positive charges increased the IFVs, whereas negative charges reduced them. These data are in agreement with the results of case 2, where discharge inception is considered in the anode region. In [3], presence of negative surface charges on a 15 kV high density polyethylene insulator resulted in an increase of 50% flashover voltage under negative lightning impulses. This is in agreement with our observations for case 1, where discharge initiation is supposed to take place in the vicinity of the cathode. The results presented in [4] were used above for model validation and, obviously, are in agreement with the obtained variations of IFVs. In [5], it was reported that presence of a bipolar charge layer with the maximum density up to  $-180 \mu\text{C}/\text{m}^2$  on the surface where discharge take place and up to  $+150 \mu\text{C}/\text{m}^2$  on the opposite surface, net charge density of  $-30 \mu\text{C}/\text{m}^2$ , led to a reduction of positive dc flashover voltages in  $\text{SF}_6$  by  $\sim 20\%$  when a discharge developed from the anode side. This is in agreement

with the reduction obtained here in case 2 with negative charges (see Table 7.3). It was also mentioned in [5] that negative charge increased negative dc flashover voltages by  $\sim 15\%$ . In that case, discharge developed from the cathode region, and the results are in agreement with variations observed in case 1 here.

### 7.3.2 Effect of charge location

Flashover voltage levels were also calculated for different positions of the centre of the charged belt on insulator's surface. These locations were as follows (see Figure 7.3): (1) one point at the middle of the surface at coordinate 0 cm; (2) four points at each 5 cm interval starting from the centre towards the high voltage electrode (the upper electrode) at coordinates +5, +10, +15, +20 cm; and (3) four points at each 5 cm interval from the centre towards the grounded electrode at coordinates -5, -10, -15, -20 cm. Approximate positions corresponding to 0 cm, +20 cm and -20 cm are marked in Figure 7.3. Note that the end points mimic locations where charges may be deposited by corona from the triple junction. The maximum value of the charge density was kept constant at  $Q_{max} = 50 \mu\text{C}/\text{m}^2$  for all the cases. This magnitude of  $Q_{max}$  was found to be high enough to affect IFVs and, at the same time, it is below the theoretical limit (see Section 7.3.1) meaning that back discharges from the surface are not likely to appear. Moreover, this choice allowed avoiding very high field regions in the vicinity of the charge belts when located close to the electrodes. In such cases, charge belts with higher density could act as virtual electrodes and therefore trigger discharges, but this aspect is not analyzed here. The flashover voltages for each position were calculated using the same procedure as in the previous sections. The results in Figure 7.8 demonstrate that the IFVs are affected by the position of the surface charge and their variations are dependent on charge polarity. However case 3 (with ground, negative impulse) was excluded from the discussion due to insignificant variations observed in the present study.

#### Case 1 with negative charge

Recall that in this case the grounded surface is assumed to be far away from the insulator. The calculations show that the IFV increases when moving the centre of the negatively charged belt away from the high voltage electrode (anode, coordinate +22 cm) until they reach a maximum at about -14 cm. Further displacement towards the cathode (e.g., coordinate -22 cm) leads to a reduction of the flashover voltage. In this case, the criterion for streamer propagation and sustenance (average field condition) is fulfilled at a lower voltage than the voltage required for satisfying the streamer inception criterion. Thus, the critical parameter, which determines the flashover voltages, is the magnitude of the electric field in the cathode ionization region which depends on the position of the deposited surface charge.

Figure 7.9 shows field distributions in the vicinity of the insulator surface calculated for four cases corresponding to zero surface charge and charges of the same magnitude situated at different locations on the surface. In the first case ( $Q_{max} = 0$ ), the field distr-

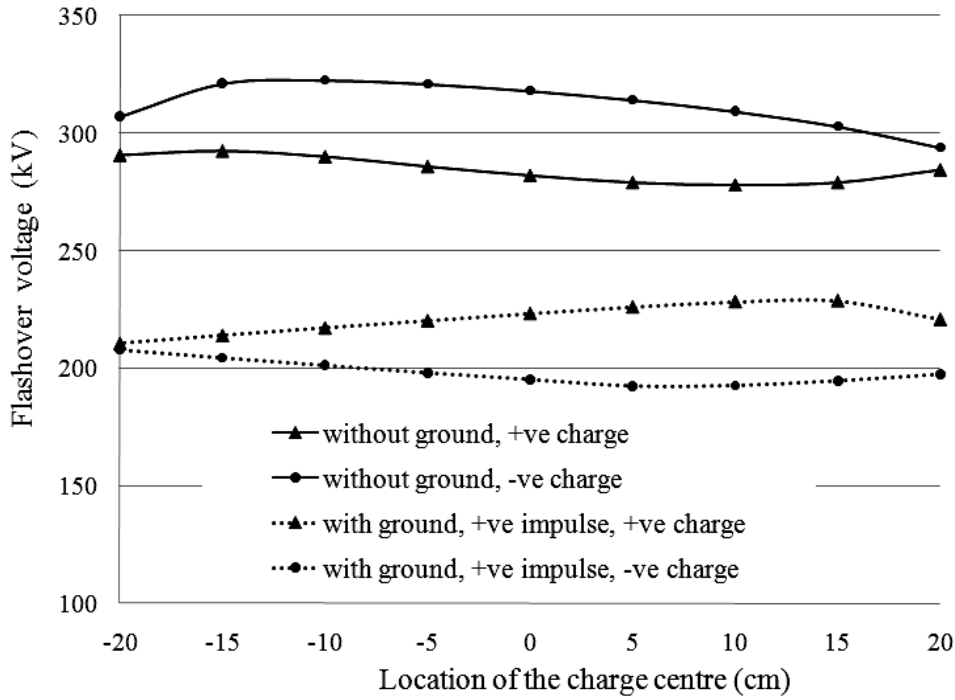


Figure 7.8. Variations of the flashover voltages with the location of the surface charges for cases 1 and 2;  $Q_{max} = 50 \mu\text{C}/\text{m}^2$ .

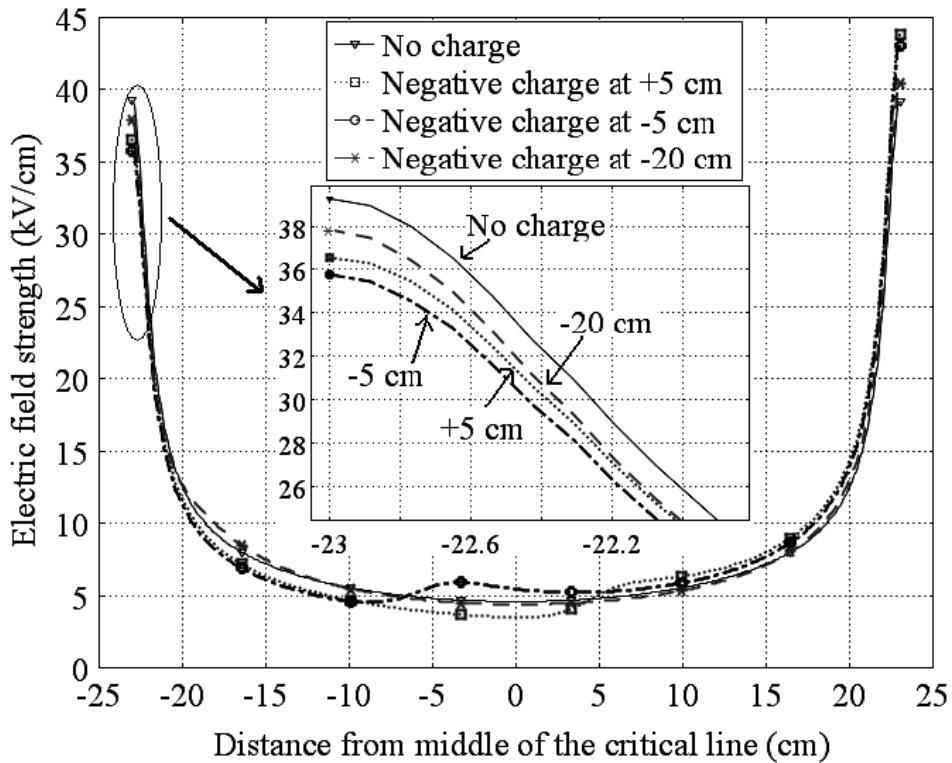
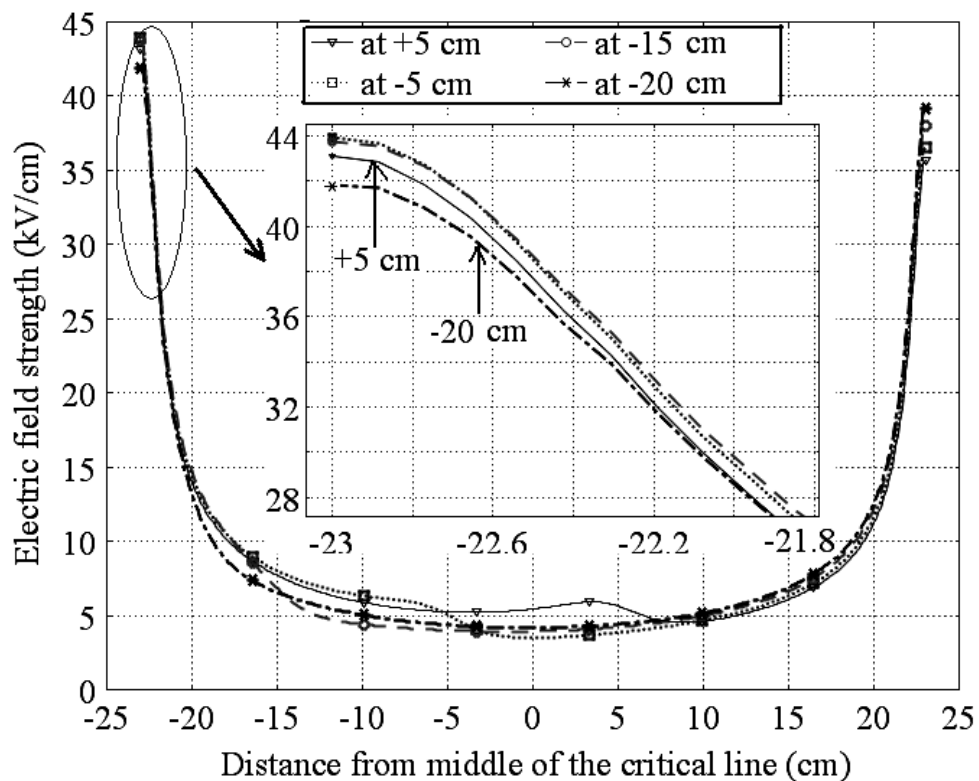


Figure 7.9. Magnitude of the electric field strength along the critical line obtained for the case 1 without deposited charge and with negative charges, applied voltage 300 kV.

tribution is symmetrical and its strength reaches  $\sim 4$  MV/m. Presence of the negatively charged spot leads to a reduction of the field intensity in the cathode region that is more pronounced when the charge centre is getting closer to the cathode surface (observe curves for +5 and -5 cm in the inset). The ionization intensity becomes weaker due to field reduction and the flashover voltages increase as it is seen in Figure 7.8. However, in the case when the negative surface charge is located in the vicinity of the cathode, superposition of the fields produced by both the electrode and the charged spot leads to the enhancement of the field on the critical line, as seen in the inset in Figure 7.9. The charge at this location acts as a protrusion on insulator surface connected to the electrode and the resulting flashover voltage is reduced.

### Case 1 with positive charge

In case 1, when positive charges are deposited on the surface, the field intensity at the cathode is high (see inset in Figure 7.10) and the IFVs are determined by the average field required for streamer propagation as the other two conditions are fulfilled at lower voltages. Therefore, field variations along the critical line in the middle of the gap outside the electrode regions become important. As it is seen in Figure 7.10, the general tendency is that the field strength increases between the charged area and the cathode and decreases in the rest of the gap when moving it away from the high voltage electrode (anode). This leads to a reduction of the average field intensity and



**Figure 7.10.** Magnitude of the electric field strength along the critical line obtained for case 1 with positive surface charges located at different positions; applied voltage 300 kV.

corresponding increment of IFVs observed in Figure 7.8 (for the range of distances from +12 to -15 cm). When the positive surface charge is situated close to the electrodes, the field strength in the middle of the gap is affected differently – the average field becomes higher when the charge is getting closer to the cathode and it becomes lower when the spot is getting closer to the anode. Correspondingly, the calculated IFVs decrease or increase, as can be seen in Figure 7.8, for distances less than -15 cm and greater than +12 cm, respectively.

### **Case 2 with negative charge**

Here, the IFVs decrease when the surface charges are moved away from the grounded electrode until they reach a minimum at coordinate +5 cm (Figure 7.8, dotted line). Further displacement of the charge centre towards the high voltage electrode (coordinate +20 cm) leads to a increment of the IFV. The reason is that the average field condition is not fulfilled when the inception criterion is satisfied and, hence, further increase of the voltage is required to get a sufficiently high average field.

### **Case 2 with positive charge**

As it is seen in Figure 7.8, the IFVs increase when moving the centre of the charged belt away from the grounded electrode, which is located at coordinate -22 cm, until their magnitude reaches a maximum at +15 cm. Similarly to the previous case, the behavior of the flashover characteristics changes when the charge belt comes closer to the energized electrode. In this case, the critical condition, which determines the IFVs, is the streamer inception criterion. Thus one has to analyze the electric field in the anode region to explain the variations in the IFVs. When the positive charge belt moves towards the anode, the electric field strength in the anode region reduces and the IFVs increase. However, as it was mentioned earlier for case 1 with negative charges, when the charge belt comes very close to the anode (+15 - +20 cm), a superposition of the fields produced by the charge itself and by the electrode takes place, thus resulting in a field enhancement and reduction of the IFVs seen in Figure 7.8.

### **7.3.3 Effect of the material**

The effect of the insulator material was studied for cases 1 and 2 by varying the relative permittivity  $\epsilon_r$  within the range of 2.3-12. For each of the cases, calculations were performed for three conditions: without charges, with positive and negative charges deposited on the insulator surface. For the latter, a Gaussian type distribution with the maximum charge density of  $50 \mu\text{C}/\text{m}^2$  located at the centre of the insulator was used. The results of the simulations are summarized in Figure 7.11.

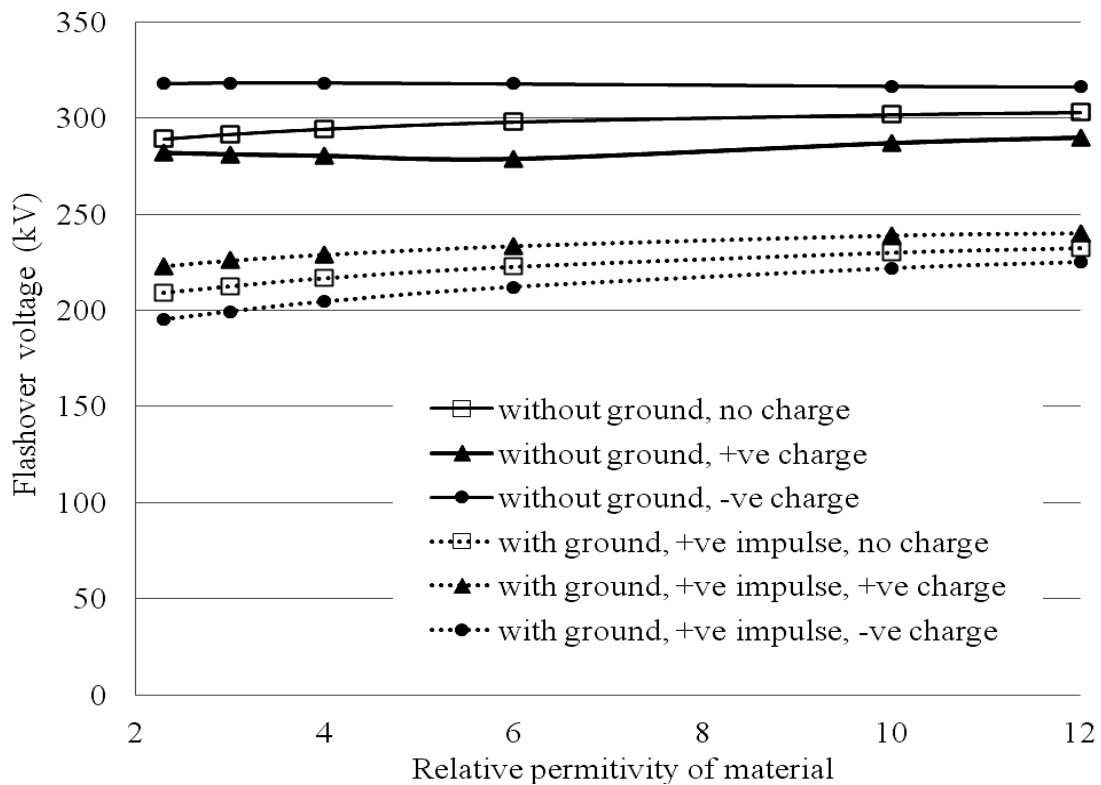


**Figure 7.11.** Variations of the IFVs with the relative permittivity of the insulation material for cases 1 and 2, surface charges with the maximum density of  $50 \mu\text{C}/\text{m}^2$  is located at the center of the insulator surface.

### Case 1

As it can be seen for case 1 with no deposited charges (solid lines), the IFVs slightly increase when using materials with higher permittivity. However, the range of variations is not significant and it is in the order of 5%. The rate of the changes of the flashover voltages (slopes of the curves) is slightly higher for low permittivity material and it gets lower at higher magnitudes of  $\epsilon_r$ . In presence of positive charges on the surface, the IFV slightly decreases with increasing permittivity until  $\epsilon_r$  reaches  $\sim 6$ . Further increase of  $\epsilon_r$  leads to an increase of IFVs with maximum variation of  $\sim 4\%$ . Negative surface charge causes no significant changes to the IFVs.

The analysis of the computed field patterns shows that the increase of the dielectric constant of the material leads to redistribution of the field around the insulator in such a way that the field strength along the surface (gas-solid interface) increases. However, it remains much lower than it is in the surrounding air and, hence, line 1 (Figure 7.3) still represents highly probable path for a flashover and it is considered as a critical line. Based on the field distributions along this line, the calculated flashover voltages for the cases with zero charge and with negative deposited charges are found to be determined by the streamer inception condition as the other criteria are already satisfied at lower voltages. Presence of the negatively charged spot on the surface leads to a reduction of

the field strength at the cathode and, hence, to higher flashover voltages than that for the case without pre-deposited charges. The effect becomes weaker at higher permittivities of the insulator material due to field enhancement in the gas phase.

At positive polarity of the deposited surface charges and permittivity values up to  $\sim 6$ , the dominant criterion defining flashover voltages is the average field condition for streamer propagation, and the flashover voltage depends on the field distribution in the middle of the gap. The computed distributions along the critical line are shown in Figure 7.12 for two values of the permittivity of the insulator material  $\epsilon_r = 3$  and 6. One can observe that the field strength on the cathode side of the gap (left) increases due to presence of the positive surface charges whereas it decreases on the part of the insulator closer to the anode. These variations result in a higher average field for the high permittivity material that defines the slightly lower level of the flashover voltage seen in Figure 7.11. When  $\epsilon_r > 6$ , the field in the ionization region decreases further and streamer inception criteria becomes dominant thus resulting in higher IFV values.

### Case 2

In case 2, the IFVs increase if the relative permittivity of the insulation increases (Figure 7.11, dotted lines). Percentage variations of IFV due to increase of  $\epsilon_r$  from 2.3 to 12 are 11%, 8% and 15% for no charge, positive and negative deposited charges,

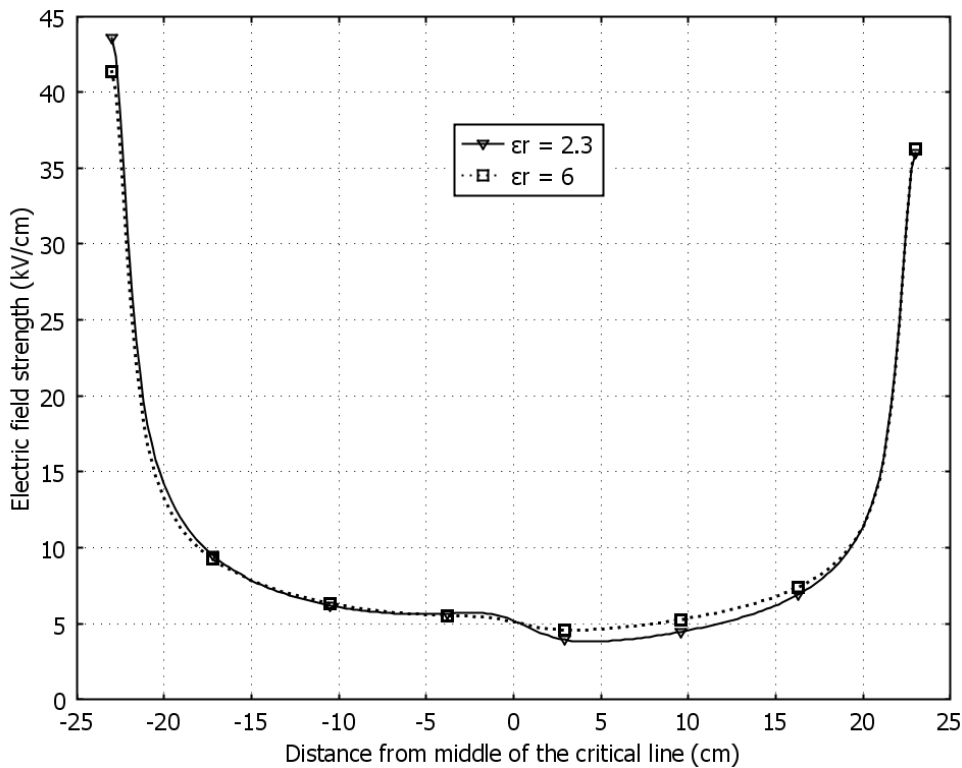


**Figure 7.12.** Magnitude of the electric field strength along the critical line obtained for the case 1 with positive charges of  $Q_{max}=50 \mu\text{C}/\text{m}^2$  located at the centre, applied voltage 300 kV.

respectively. Also one can observe that the surface charge effect is less pronounced at higher values of  $\epsilon_r$ . For all cases, the flashover conditions are dominated by the streamer inception criterion and thus the field strength in the anode region becomes an important parameter. Figure 7.13 shows the electric field distributions along the critical line obtained for two values of the dielectric constant  $\epsilon_r$  with negative surface charges. It can be observed that the increase of  $\epsilon_r$  results in a reduction of the field strength in the anode region that leads to higher IFVs. Similar field reduction due to increase of  $\epsilon_r$  was observed for the cases with no charge and positive charge.

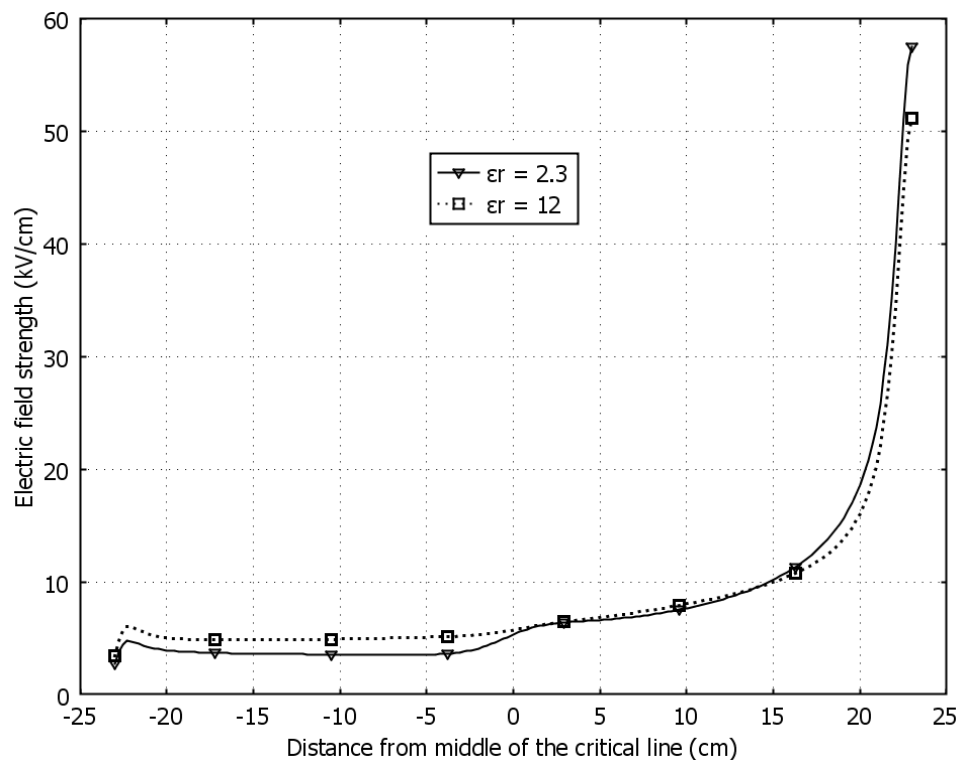


**Figure 7.13.** Magnitude of the electric field strength along the critical line obtained for the case 2 with negative charges of  $Q_{max} = 50 \mu\text{C}/\text{m}^2$  located at the centre, applied voltage 300 kV.



## 8 Conclusions

As the primary objective of the work presented in this thesis was to identify the dynamic of surface charges on insulating polymeric materials and their effect on withstand performance of high voltage polymeric insulators, the research activities concentrated on three main topics. The first one was related to surface charging by corona on flat and cylindrical samples of typical materials used in outdoor applications. Within the second topic surface charge decay on thick flat insulation samples was measured and analyzed. Finally, as the third topic, effects of surface charging on dc and impulse performance of cylindrical insulator models was investigated and modeled. Conclusions drawn from each of these studies are presented below.

### 8.1 Charging of polymeric surfaces

#### Simulation studies

A computer model describing dynamic behavior of space charges and electrical fields in positive impulse corona discharge in air was developed and implemented for a needle-plane electrode configuration. The model was validated by comparing measured and simulated corona current traces, which showed that the developed model was capable to reproduce the measured corona current well. The simulations demonstrated that different types of pre-onset corona modes, namely burst pulses and glow corona, could be identified in air under positive impulse voltages. Appearance of these modes was highly dependent upon the shape of the applied impulse voltage, especially the rate of voltage rise. Glow corona mode was observed under long impulse rise times while burst corona appeared when short impulses were applied. In both the cases positive ions were identified as dominant carriers forming space charge in the gap.

The dynamic behavior of surface charges associated with the corona charging was studied by utilizing the developed model and the simulations were carried out for the two corona regimes. In the case of glow corona, charge deposition was observed as a continuous process during which the radius of the charged spot on the solid surface was gradually increasing. In the case of burst corona, ions were delivered to the gas-

solid interface in portions and each burst contributed to the total amount of deposited charges. The resulting radius of the charged area was found to be smaller than for the case of glow corona.

## Experimental studies

The surface charging of flat HTV silicone rubber samples and a cylindrical polymeric model insulator was studied by measuring the resulting surface potential distributions, which were further used to derive charge density distributions either by field analyses and/or  $\Phi$ -matrix method.

Deposition of negative charges yielded slightly higher surface potential values and, hence, higher amount of charges than those appearing at positive corona polarity. The resulting potential and charge density profiles were either bell-shaped or saddle-shaped, depending on the charging voltage. The later appeared at higher corona voltage levels and were most probably affected by back discharges taking place when the field produced by the deposited surface charges was strong enough for their initiation. In the case of cylindrical insulator model, the amount of the net charge on the surface increased linearly with the charging voltage for both positive and negative polarities. On the other hand, the higher charging voltages resulted in a wider spreading of charges on the insulator surface, whereas increasing the charging time did not affect the magnitude of the surface potential, thus showing a limit up to which the surface could be charged.

Charging of the insulator by pre-stressing with negative dc voltage resulted in accumulation of homo-charge (i.e. charges having same polarity as adjacent electrode) closer to the electrodes with its polarity reversal at the center of the sample. Higher pre-stressing voltages did not influence significantly the surface charge density at the energized electrode while it increased at the grounded side.

## 8.2 Surface charge decay

Surface potential decay on corona charged HTV silicone rubber samples was studied experimentally. Effects of material properties (i.e. bulk neutralization), polarity of deposited charges, intensity of gas neutralization process and surface conduction on surface charge decay were analyzed.

### Decay due to bulk neutralization

The initial (measured 1 min after charging) potential distributions resulting from the corona charging had either saddle-like or bell-like shapes. During the decay, no lateral expansion of the charged spot was registered on non-aged samples, which indicated negligible effect of surface conduction. Faster potential decay was recorded at the regions with higher potentials, implying that the charge decay was field dependent. No

significant effects of the polarity of deposited charges on the decay processes were found. However, it was strongly dependent on material conductivity. For both the materials studied, the decay rates showed an exponential dependence on the potential (field) for the magnitudes higher than 500 V (corresponding average field > 2.5 kV/cm), while they decreased drastically at lower potential levels. Even though the calculated on this basis apparent bulk conductivities followed the exponential dependence on the square root of surface potential, as predicted by Poole-Frenkel model, the theoretical values of the Poole-Frenkel factor did not agree well with those obtained experimentally.

### **Contribution of gas neutralization**

When the natural gas neutralization of the deposited surface charges was allowed, the decay characteristics changed significantly, showing faster reduction of the surface potential for the material characterized by lower bulk conductivity (Elastosil). At the same time, it did not affect the decay on the more conductive material (Powersil). However, when ion densities in air were increased ten times over their natural level, the charge decay for both materials became very fast and the decay characteristics did not show any significant dependency on the material's bulk conductivity.

### **Contribution of surface conduction**

It was observed that surface charge decayed much faster on samples that were earlier aged by ac corona. This appeared to be a result of significantly increased surface conductivity, which could be attributed to the surface oxidation and formation of silica-like layers on the material surface. During the decay, lateral expansion of the charged spot was also registered. As being controlled by surface conductivity, the decay process was found to be sensitive to relative humidity in the surrounding air (especially at longer times), whereas the humidity did not play any role during the potential decay on the non-aged materials. Images of trap energy distributions deduced from the results of the surface potential decay measurements showed that the aging shifted the distributions towards lower energy levels, yielding an increased density of shallow traps as compared to the non-aged material.

## **8.3 Effect of surface charge on flashover performance of insulation**

### **DC flashover performance**

Effect of surface charges on negative dc flashover voltage of a cylindrical polymeric insulator model was studied experimentally and theoretically. Surface of the insulator was charged by corona discharge from a needle belt mounted around it. The obtained results showed that negative dc flashover voltage increased when negative charges were

deposited on the model insulator surface whereas it decreased when positive charges were present. Further, it was observed that the variation of the flashover voltages changed linearly with the amount of deposited charge. Performed analyses of the electric field along the insulator and the corresponding effective ionization coefficients confirmed that the observed variations in flashover voltage appeared due to the field modification in the cathode region (at the energized electrode).

A computer model based on streamer criteria together with electrical field calculations was used to estimate the flashover voltage levels. The comparison of the results showed that the calculated flashover voltages well matched the measured values for all the charging conditions.

### **Impulse flashover performance**

The computer model used for the dc flashover studies was further adopted for simulating impulse flashover voltage level of a post insulator. First, the performance of the model was validated using experimental data available in literature and then the effects of deposited charge magnitude, its polarity and location on the surface were investigated.

It was shown that the dependence of impulse flashover voltage on charge polarity and concentration was similar to that of dc flashover voltage for the cases when the insulator was located far away from the ground (symmetry with regard to voltage polarity). However, the insulator was standing on a grounded plane, the effect of surface charging was dependent on the polarity of the applied impulse voltage. In the case of positive impulse, presence of positive charge increased the flashover voltage, whereas negative charge yielded their reduction. In the case of negative impulse, negative charge caused a decrease of the flashover voltages, whereas positive charge did not make significant changes.

## 9 Future work

A natural way of continuation of the work presented in this thesis and related to charge accumulation on surfaces of polymeric insulators would be through performing additional experimental and theoretical investigations for identifying the possible mechanism of charge exchange at the air-solid interface. This would eventually allow for combining together models representing the charge dynamic in a gas phase during a corona discharge together with models describing charge transport in the solid. Performance of such a combined model could be validated by experimentally quantifying surface and space charge time-resolved measurements in an open electrode system.

As the presented studies of surface charge decay were limited to defining the main reasons for charge neutralization, e.g., bulk neutralization and/or gas neutralization, a continuation should concentrate on identification of the relative importance of various bulk related decay processes, such as intrinsic conduction, polarization, charge injection, etc. Also a study of charge deposition and decay on sandwich-like solid material structures, like elastomeric materials deposited on fiber-glass filled epoxies, would be of great importance for elucidating the behavior of real composite insulators.

The experimental studies related to the effect of surface charge deposition on flashover performance were, so far, carried out on small insulator model and showed a considerable effect on flashover performance in dry conditions. Extension of this work to study the effect on real insulators and at various environmental conditions is necessary, both for confirming the presented experimental findings as well as for confirming the validity of the elaborated simulation model. Development of a proper charging method allowing for controllable charge deposition, characterization of charge dynamics on insulator surfaces and establishment of repeatable flashover test procedures, for both for dc and impulse tests, can be named among the necessary tasks to be fulfilled.

Finally, the continuation of the work would help in elaborating relevant standards for testing insulators for HVDC application.



## References

- [1] G. Asplund, “HVDC towards more power and higher voltage- a challenge for the insulation”, closing lecture, Proc. 21<sup>st</sup> Nordic Insul. Symp. (NORD-IS 09), Gothenburg, Sweden, 2009.
- [2] R. Hackam, “Outdoor HV Composite Polymeric Insulators”, *IEEE Trans. Dielectr. Electr. Insul.*, Vol. 6, No. 5, pp. 557–585, 1999.
- [3] M. S. A. A. Hammam, S. Ochiai and C. Burns, “Effect of 50% flashover voltage due to accumulated charge on the surface of polymeric insulators”, Proc. 3<sup>rd</sup> Int. Conf. Properties and Appl. Dielectr. Materials, pp. 981-984, Tokyo, Japan, 1991.
- [4] S. G. J. Ehnberg and H. J. M. Blennow, “Effects of surface charge accumulation on impulse flashover voltage on silicone rubber surface”, Proc. 13<sup>th</sup> Int. Symp. High Volt. Eng. (ISH 03), p. 242, Delft, Netherlands, 2003.
- [5] A. Winter and J. Kindersberger, “Surface charge accumulation on insulating plates in SF<sub>6</sub> and effect on DC and AC breakdown voltage of electrode arrangements”, IEEE Ann. Rep. Conf. El. Ins. Diel. Phen. (CEIDP 02), pp. 757-761, Mexico, 2002.
- [6] S. Tenbohlen and G. Schröder, “The influence of surface charge on lightning impulse breakdown of spacers in SF<sub>6</sub>”, *IEEE Trans. Dielectr. Electr. Insul.*, Vol. 7, No. 2, pp. 241-246, 2000.
- [7] F. Wang, Y. Qiu, W. Pfeiffer and E. Kuffel, “Insulator surface charge accumulation under impulse voltage”, *IEEE Trans. Dielectr. Electr. Insul.*, Vol. 11, No. 5, pp. 847-854, 2004.
- [8] M. Darveniza, T. K. Saha, M. A. Leijon and S. Wright, “Effects of deposited charge on impulse test techniques for polymeric insulators”, CIGRE Symposium CAIRNS, Paper 200-11, Australia, 2001.
- [9] A. Jose Giacometti and Jr. O. N. Oliveira, “Corona charging of polymers”, *IEEE Trans. Electr. Insul.*, Vol. 27, pp. 924-943, 1992.

## References

- [10] P. Molinie, "Measuring and modeling transient insulator response to charging: the contribution of surface potential studies", *IEEE Trans. Dielectr. Electr. Insul.*, Vol. 12, No. 5, pp. 939-950, 2005.
- [11] T. Mizutani and M. Ieda, "Carrier transport in high-density polyethylene", *J. Phys. D: Appl. Phys.*, Vol. 12, pp. 291-296, 1979.
- [12] M. M. Perlman, T. J. Sonnonstine and J. A. St. Pierre, "Drift mobility determinations using surface-potential decay in insulators", *J. App. Phys.*, Vol. 47, No. 11, pp. 5016-5021, 1976.
- [13] B. Lutz and J. Kindersberger, "Determination of volume resistivity of polymeric insulators by surface charge decay", Proc. 16<sup>th</sup> Int. Symp. High Volt. Eng. (ISH 09), Paper A-4, Innes House, Johannesburg, 2009.
- [14] H. Sjöstedt, S. M. Gubanski, and Y. V. Serdyuk, "Charging characteristics of EPDM and silicone rubbers deduced from surface potential measurements", *IEEE Trans. Dielectr. Electr. Insul.*, Vol. 16, No. 3, pp. 696-703, 2009.
- [15] S. Sahli, A. Bellel, Z. Ziari, A. Kahloure and Y. Segui, "Measure and analysis of potential decay in polyethelene films after negative corona charge deposition", *Journal of Electrostatics*, Vol. 57, pp. 169-181, 2003.
- [16] P. Llovera and P. Molinie, "New methodology for surface potential decay measurements: application to study charge injection dynamic on polyethylene films", *IEEE Trans. Dielectr. Electr. Insul.*, Vol. 11, No. 6, pp. 1049-1056, 2004.
- [17] G. Asplund, "Sustainable energy systems with HVDC transmission", IEEE Power Eng. Soc. general meeting, Vol. 2, pp. 2299-2303, 2004.
- [18] M. A. Abdul- Hussain and M. J. Cornik, "Charge storage on insulation surfaces in air under unidirectional impulse conditions", *IEE Proceedings*, Vol. 134, Pt. A, No. 9, pp. 731-740, 1987.
- [19] J. M. Meek and J. D. Craggs, "Electrical breakdown in gases", John Wiley & Sons Ltd., 1978.
- [20] M. M. Shahin, "Mass-spectrometer Studies of corona discharges in air at atmospheric pressure", *J. Chem. Phys.*, Vol. 43, pp. 2600-2605, 1966.
- [21] M. M. Shahin, "Nature of charge carriers in negative coronas", *Applied Optics*, Vol. 8, Issue S1, pp. 106-110, 1969.
- [22] R. Toomer and T. J. Lewis, "Charge trapping in corona-charged polyethylene films", *J. Phys. D: Appl. Phys.*, Vol. 13, pp. 1343-1356, 1980.

- [23] E. A. Baum, T. J. Lewis and R. Toomer, "Decay of electrical charge on polyethylene films", *J. Phys. D: Appl. Phys.*, Vol. 10, pp. 487-497, 1977.
- [24] G. Teyssedre and C. Laurent, "Charge transport modeling in insulating polymers: from molecular to macroscopic scale", *IEEE Trans. Dielectr. Electr. Insul.*, Vol. 12, No.5, pp. 857-875, 2005.
- [25] G. G. Raju, "Dielectric in electric fields", Marcel Dekker Inc., New York, 2003.
- [26] T. J. Lewis, "Charge transport, charge injection and breakdown in polymeric insulators", *J. Phys. D: Appl. Phys.*, Vol. 23, pp. 1469-1478, 1990.
- [27] F. H. Kreuger, "Industrial high dc voltage", University Press, Delft, 1995.
- [28] Y. X. Zhou, B. L. Zhang, D. Bu, N. H. Wang, Y. N. Wang, X. D. Liang and Z. C. Guan, "Nanosecond pulse corona charging of polymers", *IEEE Trans. Dielectr. Electr. Insul.*, Vol. 14, No. 2, pp. 495-501, 2007.
- [29] J. A. Giacometti, S. Fedosov and M. M. Costa, "Corona charging of polymers: recent advances on constant current charging", *Brazilian J. of Phys.*, Vol. 29, No. 2, pp. 269-279, 1999.
- [30] R. Morrow, "The theory of positive glow corona", *J. Phys. D: Appl. Phys.*, Vol. 30, pp. 3099-3114, 1997.
- [31] R. Morrow and T. R. Blackburn, "Burst pulses and secondary steamers from positive points", *J. Phys. D: Appl. Phys.*, Vol. 35, pp. 3199-3206, 2002.
- [32] M. Ieda, G. Sawa and U. Shinihawa, "A decay process of surface electric charges across polyethylene films", *Japan. J. Appl. Phys.*, Vol. 6, pp. 793-794, 1967.
- [33] H. Von Berlepsch, "Interpretation of surface potential kinetics in HDPE by a trapping model", *J. Phys. D: App. Phys.*, Vol. 18, pp. 1155-1170, 1985.
- [34] H. J. Wintle, "Decay of static electrification by conduction processes in polyethylene", *J. Appl. Phys.*, Vol. 41, pp. 4004-4007, 1970.
- [35] R. M. Hill, "Relaxation of surface charge", *J. Phys. C: Solid State Phys.*, Vol. 8, pp. 2488-2501, 1975.
- [36] I. P. Barta, K. K. Kanazawa, B. H. Schechtman and H. Seki, "Charge carrier dynamic following pulsed photo-injection", *J. Appl. Phys.*, Vol. 42, No. 3, pp. 1124-1130, 1971.
- [37] H. Seki and I. P. Barta, "Photocurrents due to pulse illumination in the presence of trapping. II", *J. Appl. Phys.*, Vol. 42, No. 6, pp. 2407-2420, 1971.

## References

- [38] P. Molinie, "Charge injection in corona-charged polymeric films: potential decay and current measurements", *Journal of Electrostatics*, Vol. 45, pp. 265-273, 1999.
- [39] J. Kindersberger and C. Lederle, "Surface charge decay on insulators in air and sulfurhexafluorid - part II: measurements", *IEEE Trans. Dielectr. Electr. Insul.*, Vol. 15, No. 4, pp. 949-956, 2008.
- [40] P. Molinie, M. Goldman and J. Gatellet, "Surface potential decay on corona charged epoxy samples due to polarization processes", *J. Phys. D: App. Phys.*, Vol. 28, pp. 1601-1610, 1995.
- [41] H. Sjöstedt, "Electric charges on insulator surfaces and their influence on insulator performance", Licentiate thesis, Chalmers University of Technology, Sweden, 2008.
- [42] A. Neves and H. J. A. Martins, "Surface charging and charge decay in solid dielectrics", *IEEE Int. Sym. on Electrical Insulations*, pp. 782-786, Montreal, Quebec, Canada, 1996.
- [43] L. Zhang, Z. Xu, and G. Chen, "Decay of electric charges on corona charged polyethylene", *J. Phys.: Conference Series 142*, Paper ID: 012060, 2008.
- [44] J. Kindersberger and C. Lederle, "Surface charge decay on insulators in air and sulfurhexafluorid - part I: simulations", *IEEE Trans. Dielectr. Electr. Insul.*, Vol. 15, No. 4, pp. 941-948, 2008.
- [45] J. A. Voorthuyzen, W. Olthusis and P. Bergverd, "Research and development of miniature electrets", *IEEE Trans. Dielectr. Electr. Insul.*, Vol. 24, No. 2, pp. 255-266, 1989.
- [46] S. Le Roy, G. Teyssedre, and C. Laurent, "Charge transport and dissipative process in insulating polymers: experiments and model", *IEEE Trans. Dielectr. Electr. Insul.*, Vol. 12, No. 4, pp. 644-654, 2005.
- [47] Y. V. Serdyuk and S. M. Gubanski, "Computer modeling of interaction of gas discharge plasma with solid dielectric barriers", *IEEE Trans. Dielectr. Electr. Insul.*, Vol. 12, No. 4, pp. 725-735, 2005.
- [48] T. J. Sonnonstine and M. M. Perlman, "Surface potential decay in insulators with field dependent mobility and injection efficiency", *J. Appl. Phys.*, Vol. 46, pp. 3975-3981, 1975.
- [49] D. K. Das-Gupta, "Electrical properties of surface of polymeric insulators", *IEEE Trans. Dielectr. Electr. Insul.*, Vol. 27, No. 5, pp. 909-923, 1992.

- [50] B. Lutz and J. Kindersberger, "Influence of relative humidity on surface charge decay on epoxy resin insulators", Proc. 9<sup>th</sup> Int. Conf. Properties and Appl. Dielectr. Materials, Paper I-3, Harbin, China, 2009.
- [51] T. Takuma, M. Yashima and T. Kawamoto, "Principle of surface charge measurement for thick insulating specimens", *IEEE Trans. Dielectr. Electr. Insul.*, Vol. 5, No. 4, pp. 497-504, 1998.
- [52] P. Llovera, P. Molinie, A. Soria, and A. Quijano, "Measurements of electrostatic potentials and electric fields in some industrial applications: Basic principles", *Journal of Electrostatics*, Vol. 67, pp. 457–461, 2009.
- [53] M. A. Noras, "Non-contact surface charge/voltage measurements: Fieldmeter and voltmeter methods", Trek Application Note No. 3002, Trek Inc. 2002.
- [54] M. A. Noras, "Non-contact surface charge/voltage measurements: Capacitive probe principle of operation", Trek Application Note No. 3001, Trek Inc. 2002.
- [55] M. Noras and A. Pandey, "Evaluation of surface charge density with electrostatic voltmeter – Measurement geometry consideration", IEEE Industrial Applications Society Annual Meeting, Session 22, Alberta, Canada, 2008.
- [56] D. C. Faircloth and N. L. Allen, "High resolution measurement of surface charge densities on insulator surfaces", *IEEE Trans. Dielectr. Electr. Insul.*, Vol. 10, No. 2, pp. 285-290, 2003.
- [57] H. Sjöstedt, R. Montaña, Y. Serdyuk and S. M. Gubanski, "Charge relaxation on surfaces of polymeric insulating materials for outdoor applications", Proc. Int. Con. Adv. in Processing. Testing and Appl. of Diel. Mat (APTADM), pp. 17-20, Wroclaw, Poland, 2007.
- [58] V. Adamec and J. H. Calderwood, "The interpretation of potential decay on the surface of a charged dielectric specimen", *J. Phys. D: Appl. Phys.*, Vol. 20, pp. 803-804, 1987.
- [59] R. Robert and S. M. Berleze, "Integro-differential equation of absorptive capacitors", *IEEE Trans. Dielectr. Electr. Insul.*, Vol. 8, No. 2, pp. 244-247, 2001.
- [60] J. M. Alison and R. M. Hill, "A model for bipolar charge transport, trapping and recombination in cross linked polyethylene", *J. Phys. D: Appl. Phys.*, Vol. 27, pp. 1291-1299, 1994.
- [61] J. C. Simmons and M.C. Tam, "Theory of isothermal currents and the direct determination of trap parameters in semiconductors and insulators containing arbitrary trap distributions", *Physical Review B: Solid State*, Vol. 7, pp. 3706-3713, 1973.

## References

- [62] P. K. Watson, F. W. Schmidlin and R. V. Ladonna, "The trapping of electrons in polystyrene", *IEEE Trans. Electr. Insul.*, Vol. 27, No. 4, pp. 680-686, 1992.
- [63] P. K. Watson, "The energy distribution of localized states in polystyrene, based on isothermal discharge measurements", *J. Phys. D: Appl. Phys.*, Vol. 23, pp. 1479-1484, 1990.
- [64] O. Farish and I. Al-Bawy, "Effect of surface charge on impulse flashover of insulators in SF<sub>6</sub>", *IEEE Trans. Electr. Insul.*, Vol. 26, No. 3, pp. 443-452, 1991.
- [65] Z. Liu, P. Jiang, Y. Qui and Y. Feng, "Pre-charging effects on low probability DC flashover along insulating spacer surface", Proc. 6<sup>th</sup> Int. Conf. Properties and Appl. Dielectr. Materials, pp. 603-606, Xian, China, 2000.
- [66] Xie Jun, I. D. Chalmers, "The influence of surface charge upon flash-over of particle-contaminated insulators in SF<sub>6</sub> under impulse-voltage conditions", *J. Phys. D: Appl. Phys.*, Vol. 30, pp. 1055-1063, 1997.
- [67] J. Blenow and T. Sörqvist, "Effect of surface flashover voltage of polymer materials", Proc. 19<sup>th</sup> Nordic Insul. Symp. (NORD-IS 05), pp. 262-265, Trondheim, Norway, 2005.
- [68] F.H. Kreuger, "Industrial high voltage", University press, Delft, 1993.
- [69] L. Tang and M. R. Raghuvier, "Numerical prediction of HVDC wall bushing flashover caused by uneven wetting", *IEEE Ann. Rep. Conf. El. Ins. Diel. Phen. (CEIDP 96)*, Vol. 2, pp. 455-458, Millbrae, California, USA, 1996.
- [70] L. Tang, and M. R. Raghuvier, "Modeling of HVDC wall bushing flashover due to uneven wetting", *IEEE Transaction on Power Delivery*, Vol. 14, No. 1, pp. 194-199, 1999.
- [71] I. Gallimberti, "A computer model for streamer propagation", *J. Phys. D: Appl. Phys.*, Vol. 5, pp. 2179-2189, 1972.
- [72] Yu. V. Serdyuk, A. Larsson, S. M. Gubanski and M. Akyuz, "The propagation of positive streamers in a weak and uniform background electric field", *J. Phys. D: Appl. Phys.*, Vol. 34, pp. 614-623, 2001.
- [73] Yu. V. Serdyuk and S. M. Gubanski, "Modeling of negative streamer propagation in a weak uniform electric field", Proc. XXVI Int. Conf. on Phen. Ionized Gases, Vol. 3, pp. 81 – 82, Greifswald, Germany, 2003.
- [74] N. L. Allen, M. Boutlendj and H. A. Lightfoot, "Dielectric breakdown in non-uniform field air gaps ranges of applicability to dc voltage measurement", *IEEE Trans. Elec. Insul.*, Vol. 28, No. 2, 1993.

- [75] R. Montano, H. Sjöstedt, Y. V. Serdyuk and S. M. Gubanski, "Effect of surface charges on the flash over characteristics: comparison between theory and practice", *IEEE Ann. Rep. Conf. El. Ins. Diel. Phen. (CEIDP 07)*, pp. 368-371, Canada, 2007.
- [76] N. L. Allen and P.N. Mikropoulos, "Streamer Propagation along insulating surfaces", *IEEE Trans. Dielectr. Electr. Insul.*, Vol. 6, No. 3, pp. 357-362, 1999.
- [77] I. Gallimberti, G. Marchesi and L. Niemeyer, "Streamer corona at an insulator surface", *Proc. 7<sup>th</sup> Int. Symp. High Volt. Eng. (ISH 91)*, Paper 41-10, Dresden, 1991.
- [78] N. L. Allen and P. N. Mikropoulos, "Surface profile effect on streamer propagation and breakdown in air", *IEEE Trans. Dielectr. Electr. Insul.*, Vol. 8, No. 5, pp. 812-817, 2001.
- [79] L. A. Lazaridis and P. N. Mikropoulos, "Flashover along cylindrical insulating surfaces in a non-uniform field under positive switching impulse voltages", *IEEE Trans. Dielectr. Electr. Insul.*, Vol. 15, No. 3, pp. 694-700, 2008.
- [80] L. A. Lazaridis, P. N. Mikropoulos, A. Darras and A. Theocharis, "Flashover along cylindrical insulating surfaces under positive lightning impulse voltages", *17<sup>th</sup> Int. Conf. Gas Discharge and Their Applications*, Cardiff, UK, pp. 233-236, 2008.
- [81] L. A. Lazaridis and P. N. Mikropoulos, "Negative impulse flashover along cylindrical insulating surfaces bridging a short rod-plane gap under variable humidity", *IEEE Trans. Dielectr. Electr. Insul.*, Vol. 17, No. 5, pp. 1585-1591, 2010.
- [82] N. L. Allen and A. A. R. Hanshem, "The role of negative ions in the propagation of discharge across insulating surfaces", *J. Phys. D: Appl. Phys.*, Vol. 35, pp. 2551-2557, 2002.
- [83] M. Akyuz, L. Gao, V. Cooray, T.G. Gustavsson, S.M. Gubanski and A. Larsson, "Positive streamer discharges along insulating surfaces", *IEEE Trans. Dielectr. Electr. Insul.*, Vol. 8, No. 6, pp. 902-910, 2001.
- [84] C. Gomas, L. Gao, V. Cooray and F. Roman, "Breakdown characteristics of long sparks along insulating surfaces", *Proc. 16<sup>th</sup> Nordic Insul. Symp. (NORD-IS 99)*, p. 253, Lyngby, Denmark, 1999.
- [85] Yu. P. Raizer, "Gas Discharge physics", Springer Verlag, 1997.
- [86] E. Kuffel, W. S. Zaengl and J. Kuffel, "High voltage engineering: fundamentals", 2<sup>nd</sup> edit., Newness Publications, UK, 2003.

## References

- [87] Y. Serdyuk, "Computer modelling of electrophysical phenomena in high voltage insulation", Doctoral thesis, Chalmers University of Technology, Gothenburg, Sweden, 2004.
- [88] J. J. Lowke, "Theory of electrical breakdown in air- the role of metastable oxygen molecules", *J. Phys. D: Appl. Phys.*, Vol. 25, pp. 202-210, 1992.
- [89] G. G. Raju, "Gaseous electronics: theory and practice", Taylor & Francis Group, 2006.
- [90] J. W. Gallagher, E. C. Beaty, J. Dutton and L. C. Pitchford, "An annotated comparison and appraisal of electron swarm data in electronegative gases", *J. Phys. Chem. Ref. Data*, Vol. 12, No. 1, pp. 109-152, 1983.
- [91] N. Yu. Babaeva and J. K. Lee, "Dust-grain charging in developing air plasma", *IEEE Trans. Plasma Sci.*, Vol. 32, pp. 823-828, 2004.
- [92] J. Chen and J. H. Davidson, "Model of the negative dc plasma corona: comparison to the positive dc corona plasma", *Plasma Chem. Plasma Proces.*, Vol. 23, No.1, pp. 83-102, 2003.
- [93] Yu. V. Serdyuk, "Numerical simulations of non-thermal electrical discharges in air", in V. Cooray (ed.) "Lightning electromagnetics", IET, London, UK, 2012.
- [94] H. Sjöstedt, Yu. V. Serdyuk, R. Montano and S. M. Gubanski, "Experimental measurement and computer modeling of charge relaxation on surfaces of polymeric insulating materials", *IEEE Ann. Rep. Conf. El. Ins. Diel. Phen. (CEIDP 07)*, pp. 413-416, British Columbia, Canada, 2007.
- [95] R. Morrow and N. Sato, "The Discharge current induced by the motion of charged particles in time dependent electric fields; Sato's Equation extended", *J. Phys. D: Appl. Phys.*, Vol. 32, L20-L22, 1999.
- [96] B. Ma, S. M. Gubanski and H. Hillborg, "AC and DC corona/ozone induced ageing of HTV Silicone Rubber", *IEEE Trans. Dielectr. Electr. Insul.*, Vol. 18, No. 6, pp. 1984-1994, 2011.
- [97] B. Ma, "Effect of corona and ozone exposure on properties of polymeric materials for high voltage outdoor applications", Doctoral thesis, Chalmers University of Technology, Gothenburg, Sweden, 2011.
- [98] R. Enderlein and N. J. Horing, "Fundamentals of semiconductor physics and device", pp. 41-42, World Scientific Publishing Co. Pte. Ltd., 1997.

- [99] T. G. Gustavsson, "Silicone rubber insulators- Impacts of material formulation in coastal environment", Doctoral thesis, Chalmers University of Technology, Gothenburg, Sweden, 2002.
- [100] A. Kumada and S. Okabe, "Measurement of surface charge on opposite sides of a planar insulator using an electrostatic probe", *IEEE Trans. Dielectr. Electr. Insul.*, Vol. 11, No. 6, pp. 919-928, 2004.
- [101] C. Stuckenholtz, P. Lequitte, M. Gamlin and R. Connell, "Overview of test requirements on HVDC apparatus and resulting impacts on UHVDC test systems", Proc. 17<sup>th</sup> Int. Symp. High Volt. Eng. (ISH 11), p. 141, Hannover, Germany, 2011.
- [102] IEC 60060-1 (1989), *High voltage test techniques Part 1: General definitions and test requirements*, 1989.
- [103] IEEE Std 4-1995, *IEEE Standard Techniques for high voltage testing*, 1995.
- [104] K. Petcharaks and W. S. Zaengl, "Numerical calculation of breakdown voltages of standard air gaps (IEC 52) based on streamer breakdown criteria", Proc. 9<sup>th</sup> Int. Symp. High Volt. Eng. (ISH 95), paper 2173, Graz, Austria, 1995.

